Synthesis and Characterization of Solution Processed ZnO Thin Films

By

Ahmad Hossein Adl

A thesis submitted in partial fulfillment of the requirements for the degree of

Doctor of Philosophy
in
Solid State Electronics

Department of Electrical and Computer Engineering
University of Alberta

Abstract

Recently ZnO has drawn a lot of attention in semiconductor industry due to its interesting features. High exciton binding energy, high resistivity against radiation, high breakdown voltage, insensitivity to visible light, and easy wet chemical etching are some of the interesting features of this material. ZnO materials can be deposited using two ways: vacuum deposition and solution processing methods. The ZnO thin films deposited using vacuum deposition offer better crsytallinity and hence electrical performance. The main drawback of vacuum deposition is the requirement of expensive vacuum pumps. Additionally the throughput of this method is less compared to solution-processed methods. Solution processing offers a cheap easy method of ZnO thin film deposition.

Currently two solution processing methods are used: pyrolysis of a coated film of a solution-based ZnO precursor (usually zinc acetate) and the spin-coating of a colloidal dispersion of ZnO nanoparticles, subsequently subjected to sintering. In both these methods, it is difficult to control the electrical parameters of the films such as the doping density and defect concentration from run to run, and p-type ZnO is not yet reproducibly obtainable. Therefore, better methods to control the electrical characteristics of the FETs incorporating ZnO films are much needed. The properties of the semiconductor film have a huge impact on the electrical performance of the ZnO TFTs. Hence by reducing the number of defects high performance ZnO TFTs will be obtained. Another method of improving the TFT performance is by modifying the transistor structure. One method of modifying the transistor structure is through schottky barrier thin film transistor (SB-TFT) or the source gated transistor (SGT). In the first part of the thesis we will study the

effect of Schottky source contact on the enhancement of the electrical properties of thin film transistors.

The sol stabilizer used in the solution processing of ZnO functions variously as a sol homogenizer, chelating agent, wettability improver and capping agent. In spite of its obvious importance to influencing ZnO film properties, the effect of the sol stabilizer has not been systematically studied and is generally unknown. Although there are a few papers examining different stabilizers, these studies have been mainly restricted to alkaline short chain ligand bearing species such as ethanolamine, diethanolamine, triethanolamine, etc. Furthermore, these prior reports did not examine the effect of the stabilizers on the performance of the resulting ZnO thin films in optoelectronic devices. Our study also examines longer chain and acidic stabilizers such as oleic acid, oleylamine and octadecene, which are used extensively in the synthesis of colloidal II-VI quantum dots, but have not been used to form ZnO thin films. We examined the effect of six different sol stabilizers -triethylamine, oleylamine, oleic acid, octadecene, triethanolamine and ethanolamine (along with a sol without any stabilizer), on the grain size, crystallographic texture, and resistivity of solution processed ZnO films on thermal oxide-coated silicon substrates, and found large variations in the structural and electrical properties as a consequence of the choice of sol stabilizer. We synthesized ZnO films using various sol stabilizers and studied the effect of the stabilizing agent on the morphology, orientation, optical, and electrical characteristics of the deposited films. The effect of different sol stabilizers on the crystal texture of the films was investigated by studying the XRD results of the films. Raman studies were preformed on the solutions and the films to understand the nucleation and growth of the ZnO films. Four point probe

measurements were performed to compare the resistivity of the films. The ratio of the photocurrent to dark current was measured in steady state photoconductivity measurements. By measuring the transient photoconductivity, mobility−lifetime product for photogenerated charge carriers was measured for each film. By performing C-V measurements using impedance spectroscopy, the doping value of each of the films deposited with different stabilizers was measured. Thin film transistors were fabricated and the effect of different stabilizers on their parameters like mobility and threshold voltage was studied. Using the doping values extracted from C-V measurements and the field effect mobility of the TFTs the barrier height of the grain boundaries and the trapped charge density at grain boundaries was calculated.

Preface

The design of experiments, data analysis and writing of this thesis was done by the author under the supervision of Dr Karthik Shankar. Excluding the following data collection steps all the other data collection and analysis was performed by the author.

- SEM images were taken by Ms. Samira Farsinezhad PhD student at the department of Electrical and Computer Engineering.

- Raman data was collected by Dr Himani Sharma a postdoctoral fellow at the department of Electrical and Computer Engineering.

- The impedance spectroscopy data was gathered by Dr Piyush Kar a postdoctoral fellow at the department of Electrical and Computer Engineering.

Dedicated to My Parents

Acknowledgements

I would like to thank those who helped me during my PhD studies. I would like to thank my supervisor professor Karthik Shankar for his continuous support and encouragement during my PhD studies. His depth of knowledge, dedication, industriousness, and motivation has been truly inspiring. I would also like to thank my supervisory committee members Dr Ying Tsui, Dr Sandipan Pramanik, Dr Doug Barlage, and Dr Richard McCreery for their help during my PhD studies and providing useful feedback for my thesis. I would also like to thank my colleagues at the excitonic research lab for their help and collaboration during my PhD studies. I also like to thank the nanofab and NINT staff for their technical support. In the end I would like to thank the most sacred part of my life: my parents. Words are incapable of expressing my sincere appreciation to my parents for their kindness, and devotion. They have always been with me in sickness and health and rejoiced sincerely at my happiness. I am grateful to them and love them from the bottom of my heart.

Table of Contents

List of Figures

List of Tables

List of Symbols

Symbol	Definition
V_D	Drain voltage
L	Channel length
V_G	Gate voltage
V_{TH}	Threshold voltage
I_D	Drain current
μ_n	Electron mobility
C_{ox}	Oxide capacitance
W	Channel width
V_{GS}	Gate source voltage
V_{DS}	Drain source voltage
μ	Mobility
I_G	Gate leakage current
T	Temperature
μ_L	Lattice mobility
μ_i	Impurity mobility
μ_{eff}	Effective mobility
μ_{FE}	Field effect mobility
μ_{sat}	Saturation mobility
g_d	Transistor conductance
g_m	Transistor transconductance
t_r	Transit time

f_{max}	Maximum operating frequency
k	Dielectric constant
P	Power
R_T	Tunnel Resistance
K	Boltzmann constant
h	Planck constant
e	Electron charge
E_g	Bandgap energy
I_{ph}	Photocurrent
q	Electron charge
λ	Light wavelength
G	Photoconductive gain
c	Speed of light
R_λ	Responsivity
τ	Carrier lifetime
η	Quantum efficiency
ϕ_B	Source-semiconductor barrier height
V_{sat}	Saturation voltage
Ψ	Voltage at the semiconductor insulator interface
C_G	Gate dielectric capacitance
C_S	Semiconductor layer capacitance
f_T	Unity gain frequency
α	Effective barrier lowering constant (tunneling constant)
J_S	Current density
ε_s	Semiconductor permittivity constant

ε_0	Vacuum permittivity
LF	Lotgering Factor
p preferred orientation to	Ratio of summation of integrated intensities of peaks with summation of all peaks
p_0 preferred orientation to	Ratio of summation of integrated intensities of peaks with summation of all peaks for randomly oriented material
D	Crystallite Size
$\beta_{2\theta}$	Full-width half maximum of (002) Peak.
θ	Bragg Angle
σ_p	Photoconductivity
G	Generation rate
μ_p	Hole mobility
τ_n	Electron lifetime
τ_p	Hole lifetime
J_{on}	Current Density with Illumination
J_{off}	Current Density without Illumination
J_{diff}	Difference in Current Density with and without illumination
I_0	Intensity of light at film surface
υ	Frequency
R	Reflection coefficient
α	Absorption coefficient
C_{eff}	Effective capacitance
R_s	Electrolyte resistance
Q_1	Constant phase element
n_1	Exponent of Q_1
L_{eff}	Effective channel length

L_g	Grain Size
λ	Decay length of potential in grain boundary
N_d	Doping concentration
N_t	Trapped charge density at the grain boundary
V_b	Potential barrier at grain boundary
qV_n	Minimum conduction band activation energy
n	Carrier concentration
E_a	Activation energy
E_c	Conduction band
E_f	Fermi Level
J_{gb}	Current density through grain boundary
υ_n	Thermal velocity of electrons
ΔV_b	Voltage drop across Schottky barrier
A	Richardson constant
n_g	Number of grain boundary

List of Abbreviations

Abbreviation	Description
TFT	Thin Film Transistor
CdS	Cadmium Sulfide
SnO_2	Tin Oxide
Al_2O_3	Aluminum Oxide
ZnO	Zinc Oxide
SiO_x	Silicon Oxide
In_2O_3	Indium Oxide
a-Si:H	Hydrogenated Amorphous Silicon
RF	Radio Frequency
IGZO	Indium Gallium Zinc Oxide
YSZ	Yttria Stabilized Zirconium
PLD	Pulsed Laser Deposition
ZTO	Zinc Tin Oxide
IZO	Indium Zinc Oxide
Si	Silicon
Ge	Germanium
RFID	Radio frequency Identification Tag
AMLCD	Active Matrix Liquid Crystal Display
AMOLED	Active Matrix Organic Light Emitting Diode
LCD	Liquid Crystal Display
OLED	Organic Light Emitting Diode

ROM	Read Only Memory
DC	Direct Current
ALD	Atomic Layer Deposition
LED	Light Emitting Diode
LTPS	Low temperature Ploy Silicon
LPCVD	Low Pressure Chemical Vapor Deposition
SPC	Solid Phase Crystallization
UV	Ultra Violet
SLG	Supper Lateral Growth
ELC	Excimer Laser Crystallization
HIZO	Hafnium Indium Zinc Oxide
ZrO_x	Zirconium Oxide
Mg	Magnesium
Al	Aluminum
Ga	Gallium
Ga_2O_3	Gallium Oxide
ITO	Indium Tin Oxide
ATO	Aluminum Tin Oxide
SiO_2	Silicon Dioxide
SiN_x	Silicon Nitride
HfO_2	Hafnium Oxide
$HfSiO_x$	Hafnium Silicon Oxide
XRD	X-Ray Diffraction
PVP	Poly-4-Vinyl Phenol
PI	Polyimide

Hf	Hafnium
IGO	Indium Gallium Oxide
AC	Alternating Current
SiON	Silicon Oxynitride
PECVD	Plasma Enhanced Chemical vapor Deposition
MISFET	Metal Insulator Field Effect Transistor
Y_2O_3	Yttrium Oxide
OTFT	Organic Thin Film Transistor
GaN	Gallium Nitride
MBE	Molecular Beam Expitaxy
MOCVD	Metal Organic Chemical Vapor Deposition
SEM	Scanning Electron Microscopy
LHZA	Layered Hydroxide Zinc Acetate
NaOH	Sodium Hydroxide
LiOH	Lithium Hydroxide
Zn(OAc)2	Zinc Acetate
ZAD	Zinc Acetate Dihydrate
TTFT	Transparent Thin Film Transistor
MSM	Metal Semiconductor Metal
SCCM	Standard Cubic Centimeter per minute
Ag	Silver
Ru	Ruthenium
RuO_2	Ruthenium Oxide
Au	Gold
FET	Field Effect Transistor

SB-TFT	Schottky Barrier Thin Film Transistor
SGT	Source Gated Transistors
MIS	Metal Insulator Semiconductor
FESEM	Field Emission Scanning Electron Microscopy
MESFET	Metal Semiconductor Field Effect Transistor
AgCl	Silver Chloride
KCl	Potassium Chloride
GIXRD	Glancing Incidence X-Ray Diffraction
LF	Lotgering Factor
FTIR	Fourier Transform Infrared Spectroscopy
PDR	Photo to Dark Current Ratio
CVD	Chemical Vapor Deposition
CPE	Constant Phase Element
EIS	Electrochemical Impedance Spectroscopy

1   Thin Film Transistors: History and Applications

1.1   Definition of Thin Film Transistor

The Thin Film Transistor (TFT) is a three terminal device. The drain, source, and gate are the three terminals of this device. The main idea behind the TFT is similar to the metal oxide semiconductor field effect transistor (MOSFET) in which the current from the source to drain is controlled by the voltage applied to the gate. TFTs have a lot in common with other field effect devices like MOSFETs. However, some important differences can also be observed between the two structures. Unlike MOSFETs that use single crystal silicon wafers as substrates, TFTs use polycrystalline or amorphous films deposited on insulating substrates such as glass.[2] The active layer in TFT has more defects compared to their single crystal counterparts, which degrades the performance of the TFTs. For instance TFTs generally exhibit lower mobility and higher leakage current compared to the single crystal MOSFETs. A general way of improving the performance of the TFTs is by reducing the bulk and interface trap densities.[3] The processing temperatures for the TFTs (600-650 ^{o}C) are also lower compared to the MOSFETs (1000 ^{o}C). Unlike TFTs, MOSFETs have $p-n$ junctions at source drain regions. TFTs modulate the conductance of the semiconductor at the interface with the dielectric by forming an accumulation layer while in the MOSFETs, an inversion layer must be formed.[2] TFTs are useful to design circuits on large area or flexible substrates where the conventional semiconductor technology is too expensive. For instance in display technologies, where an array of transistors is expected to control the lighting elements, device performance requirements are less stringent compared to the MOSFET applications.[3]

1.2   History

Thin film transistors (TFT) were invented in 1925 and patented in 1930 by J. E. Lilienfeld and O. Heil.[4] However, due to the limited knowledge about semiconductor materials and vacuum deposition techniques, the first TFT was fabricated in RCA laboratories in 1962 by Weimer.[5] The active layer in this top gate TFT was poly-crystalline n-type CdS deposited on silicon dioxide insulator with gold source and drain electrodes.[6] In 1964, Klasens and Koelmans fabricated the first transparent TFT using

SnO$_2$ as the active layer, anodized Al$_2$O$_3$ as the gate dielectric and aluminum source and drain electrodes.[7] Boesen and Jacobs reported a lithium doped ZnO TFT with evaporated SiO$_x$ gate dielectric and aluminum drain and source electrodes.[8] However, this TFT suffered from low gate voltage effect and did not show saturation behavior.[2] Similarly, Aoki and Sasakura fabricated a transparent SnO$_2$ TFT with poor electrical performance.[9] In 1996 Prins and Seager fabricated SnO$_2$:Sb and In$_2$O$_3$ ferroelectric TFTs, respectively which were used to demonstrate hysteresis behavior in ferroelectric materials.[10,11] The first high performance transparent TFTs with performances comparable with a-Si:H TFTs were reported in 2003. The drawback of these works was that the processing temperature required was in the range of 450-600 °C.[12] [13] In order to circumvent this problem, RF magnetron sputtering was used which resulted in the same electrical performance by room temperature processing.[14]

In addition to binary oxides, complex semiconductor materials were also utilized in the active layer of the TFTs. Nomura grew an epitaxial layer of InGaO$_3$(ZnO)$_5$ (GIZO) on yttria-stabilized zirconia (YSZ) substrate. This device exhibited an exceptional mobility of 80 cm^{2}V^{-1}s^{-1}, an on-off ratio of 10^6, and a turn on voltage of -0.5V.[15] In spite of using high temperatures for fabrication of this TFT, this work provided proof that oxide semiconductors were capable of high performance.[2] A year later, Nomura used pulsed laser deposition (PLD) at room temperature to fabricate amorphous GIZO. This device exhibited a mobility of 9 cm^{2}V^{-1}s^{-1}, a threshold voltage of 1-2 V, and an on-off ratio of 10^3.[16] This was the beginning of applying multicomponent oxide semiconductors as the active layers of TFTs. ZTO[17,18], IZO[19-20], and GIZO[21-22] are some of the examples of these multicomponent materials. Figure 1.1 shows the major breakthroughs in the development of oxide thin film transistors. Hence it can be concluded that oxide semiconductors are an attractive alternative for the active layer of the TFTs.
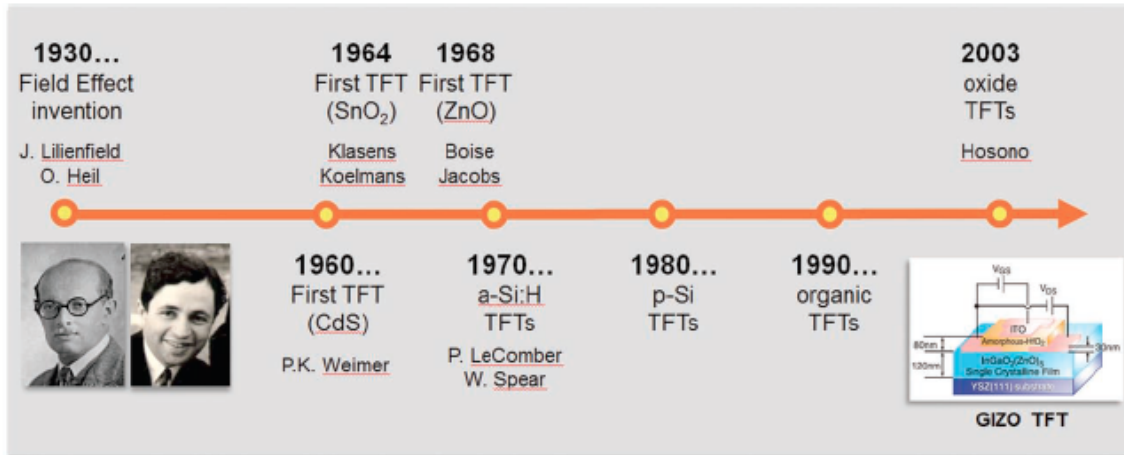
Figure 1-1 The development of thin film transistors in time. (Adapted with permission from Ref[2]; Copyright John Wiley & Sons, Inc.)

1.3 Operation of Thin Film Transistors

Thin Film Transistors (TFTs) are three terminal devices. The basic idea behind these devices is variation of the current between the source and drain electrodes through a potential applied at a third electrode known as the gate.[23] Figure 1-2 shows the different structures of the TFTs:
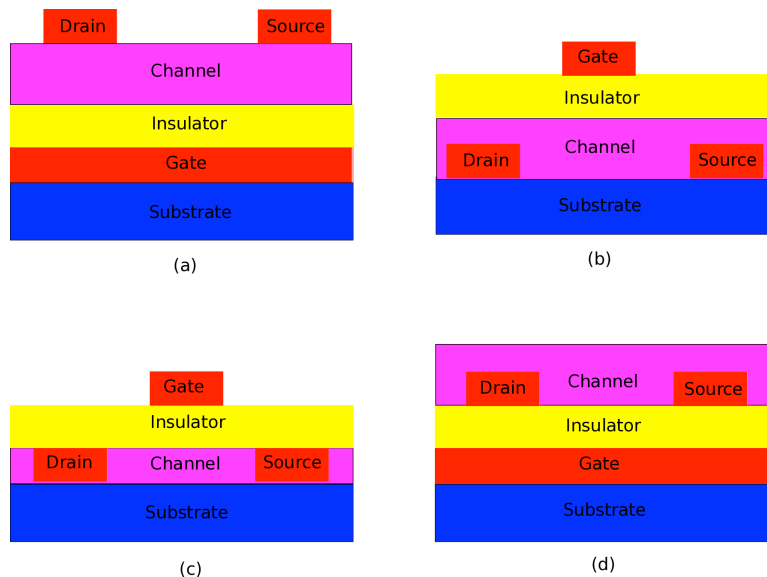
Figure 1-2 Structure of *staggered* a) bottom gate b) top gate, and *coplanar* c) top gate d) bottom gate TFTs.

When a gate voltage higher than a threshold voltage is applied to the gate, a sheet of charges with opposite sign is generated at the insulator-semiconductor interface. Hence

3

the conduction channel is formed. When no voltage is applied to the drain, the charge distribution will be uniform along the channel. Applying a voltage of V_D to the drain causes the potential of point X in the drain to become $V(x)$ which varies continuously from the source electrode ($x=0$, $V(x)=0$) to the drain electrode ($x=L$, $V(x)=V_D$) where L is the channel length. As long as $V_G\text{-}V_{TH} \geq V_D$, the charge will be present throughout the length of the channel. In this regime, which is called the linear region of the operating characteristic, the drain current varies linearly with the drain voltage. When the drain voltage is equal to $V_G\text{-}V_{TH}$ the potential, and as a result the charge at the drain region, will be zero. Hence the channel is pinched off and the drain current is saturated. This regime of operation is called the saturation region.[24] Equation of the drain current in linear region is as follows:

$$I_D = \mu_n C_{ox} \frac{W}{L}\left((V_{GS} - V_{TH})V_{DS} - \frac{1}{2}V_{DS}^2 \right) \qquad (1\text{-}1)$$

As for the saturation region, the drain current equation is as follows:

$$I_D = \frac{1}{2}\mu_n C_{ox} \frac{W}{L}(V_{GS} - V_{TH})^2 \qquad (1\text{-}2)$$

Where W is the channel width, L the channel length, and C_{ox} is the capacitance per unit area.[24]

The structure of different thin film transistors can be seen in figure 1-2. Self-alignment of source and drain contacts with respect to the channel region is the main advantage of the coplanar structure. This will reduce the parasitic capacitance of the TFT. In addition to reduction of parasitic capacitance, the self-alignment enables scaling down the channel dimensions, which improves the pixel to aperture ratio. This is a desirable feature in imaging or display applications. In the staggered structures the source-drain contacts are made on opposite sides of the channel layer with respect to gate, which makes the electric field smaller in the drain region compared to coplanar structure. This results in the

reduction of field dependent leakage current. The performance of top gate and bottom gate TFTs are quite different. The surface of the thin film forms the channel layer in the top gate TFTs. Since in thin films the top layer has larger grain size compared to the bottom layers therefore the top gate TFTs have higher mobility compared to bottom gates. The drawback of the top gate TFTs is surface roughness due to the lateral grain growth, which causes non-uniform device performance for top gate TFT. In the bottom gate TFTs there will be no problem of surface roughness. However, due to the large number of defects at the bottom layer of the thin films the mobility is lower compared to the top gate TFT.[25]

Each of these structures have specific applications. For instance, the staggered bottom gate TFT is useful for fabricating a-Si:H TFTs due to easier processing and enhanced electrical properties. a-Si:H is a light sensitive material. In this configuration, the metal of the gate electrode covers the semiconductor, protecting it from the back light effect. The coplanar top gate structure is used for poly-Si TFTs. Generally, the crystallization of semiconductors requires high temperatures that could degrade other materials that are deposited earlier. In the bottom gate structure, the semiconductor surface is exposed to air, which could cause stability issues for the TFT. However, it is easier to modify the electrical properties of bottom gate TFTs by adsorption of impurities during annealing or plasma treatment.[2]

TFTs are characterized by a set of important electrical parameters that are useful in comparing their performance with other TFTs. These parameters are extracted from the output and transfer characteristics as shown in figure 2-2 (a) and (b). Some of these characteristics are: mobility (μ), on/off ratio and the threshold voltage (V_{TH}).
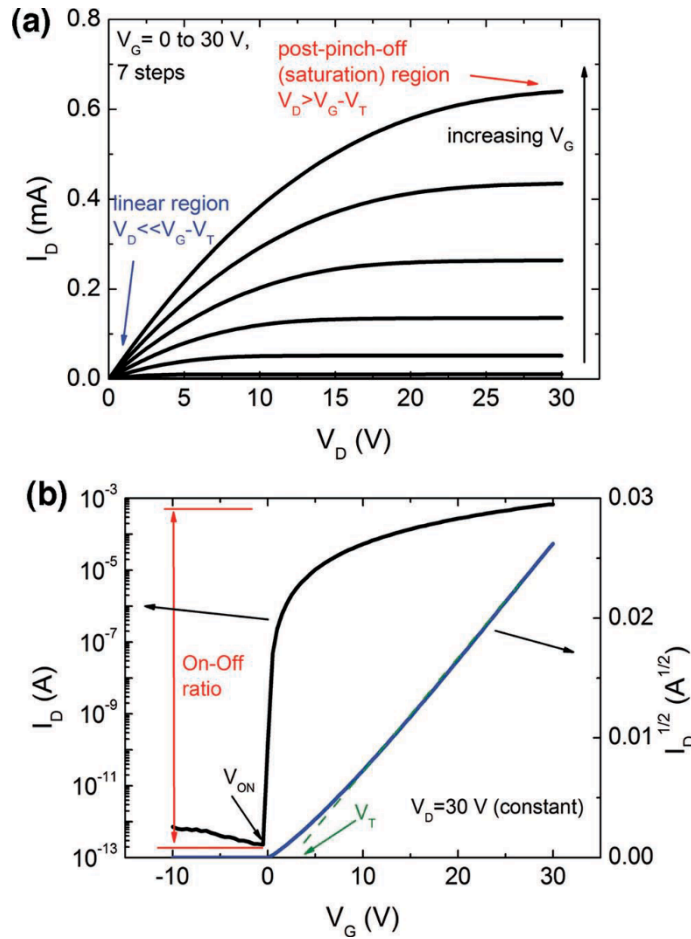
Figure 1-3 a) Output b) transfer charactersitics of *n*-type TFT. (Adapted with permission from ref[2]; Copyright John Wiley&Sons Inc)

The On/off current ratio is the ratio of the maximum to minimum drain current. The noise level of the equipment or the gate leakage current (I_G) determines the minimum drain current. The maximum drain current depends on the semiconductor material and the effectiveness of capacitive injection by the field effect. Typical on/off ratio obtained in TFTs is 10^6.[2]

Mobility (μ) is another parameter, which describes how efficient charge transport is in a material. Mobility is affected by scattering centers in the semiconductor. Impurity scattering is one of the main causes of scattering. Impurity scattering centers can also be charged. For instance, ionized donors and acceptors are examples of charged scattering centers. In the ionized scattering centers, in addition to physical collision, the electrostatic forces also cause scattering in the semiconductor. The amount of this electrostatic

6

scattering depends on the interaction time and number of impurities. Increasing the impurity concentration increases the number of scattering centers, which degrades the mobility of the semiconductor. The interaction time is related to the relative velocity of the carrier and impurity. Hence the thermal velocity of the carrier immensely impacts the interaction time. This explains the dependence of mobility on temperature. By increasing the temperature the thermal velocity of the carriers increases resulting in the reduction of interaction time. Due to the reduction of interaction time, scattering is decreased which enhances the mobility of semiconductor.[26] As a result carriers with higher thermal velocity are less deflected by Coulomb scattering. The mobility from ionized impurities is proportional to $T^{3/2}$.[27]

Scattering can also occur by lattice vibrations (phonons). Phonons are mechanical waves that travel through the semiconductor crystal. Scattering by phonons involves absorption or emission of optical or acoustic phonons. Increases in temperature increase both the phonon density and scattering resulting in lower mobility.[26] In non-polar semiconductors like Si and Ge, the acoustic phonons and ionized impurities are the main source of scattering and reduced the mobility. The mobility due to interaction with acoustic phonon is proportional to $1/T^{3/2}$.[28] Hence ionized impurity scattering and phonon scattering show different dependence on temperature. The combined mobility which is given by Matthiessen rule is:

$$\mu = \left(\frac{1}{\mu_i} + \frac{1}{\mu_L} \right)^{-1} \tag{1-3}$$

where μ_L and μ_i are the phonon mobility and ionized impurity mobility, respectively.[3]

The charge carrier mobility is reduced by several other scattering mechanisms such as bulk and interface traps, and grain boundaries. However, in TFTs, since the charge transport occurs at the dielectric-semiconductor interface, other physical phenomena can cause charge carrier scattering as well. Coulomb forces being exerted on the carriers from the charges trapped in the dielectric or in interface states is another scattering mechanism

7

in TFTs. Surface roughness scattering is another source of scattering that could affect the mobility.[2] Hence it is important to measure the mobility at the interface. There are three methods of calculating the interface mobility: 1- effective mobility (μ_{eff}) 2- field effect mobility (μ_{FE}) 3- saturation mobility (μ_{sat}).

Effective mobility is measured in the linear region of the I_D-V_{DS} curves in the $V_{DS} << V_{GS}$-V_{TH} range, which gives:

$$I_D \approx \frac{W}{L} C_{ox} \mu (V_{GS} - V_{TH}) V_{DS} \tag{1-4}$$

The output conductance for a constant V_{GS} is given by:

$$g_d = \frac{\partial I_D}{\partial V_{DS}} = \frac{W}{L} C_{ox} (V_{GS} - V_{TH}) \left(\mu + \frac{\partial \mu}{\partial V_{DS}} V_{DS} \right) \tag{1-5}$$

By neglecting the term involving the variation of mobility with respect to drain-source voltage, the effective mobility is measured as:

$$\mu_{eff} = \frac{g_d}{\frac{W}{L} C_{ox} (V_{GS} - V_{TH})} \tag{1-6}$$

Neglecting the variation of effective mobility (μ_{eff}) with respect to drain-source voltage for long channel transistors in which velocity saturation is not relevant is an acceptable assumption. Using effective mobility (μ_{eff}) to describe the performance of a TFT has some advantages compared to other mobility measurement methods: 1- the effective mobility (μ_{eff}) is measured in the linear region. In the linear region the charge distribution is uniform along the channel. Hence the concept of mobility being a proportionality constant between the electric field and carrier velocity fits this situation accurately. 2- the term neglected in calculation of effective mobility (μ_{eff}) is indeed negligible for long channel devices. However, effective mobility has some drawbacks. The first drawback is

8

that in order to calculate the effective mobility (μ_{eff}) the threshold voltage value must be known. Inaccuracies in measuring the threshold voltage will lead to errors in calculation of the effective mobility. The second drawback is that the effective mobility (μ_{eff}) value is undefined for the $V_{GS}=V_{TH}$ case. The third drawback is that the effective mobility (μ_{eff}) value is sensitive to the drain-source resistance.[29]

In a manner similar to the calculation of effective mobility, field effect mobility (μ_{FE}) is also evaluated in the linear regime. However, in measuring field mobility (μ_{FE}) instead of output conductance, transconductance is used as shown below (V_{DS} constant):

$$g_m = \frac{\partial I_D}{\partial V_{GS}} = \frac{W}{L} C_{ox} \mu V_{DS} \left(1 + \frac{(V_{GS}-V_{TH})}{\mu_{eff}} \frac{\partial \mu}{\partial V_{GS}} \right) \tag{1-7}$$

By neglecting the variation of mobility with respect to gate voltage we obtain:

$$\mu_{FE} = \frac{g_m}{\frac{W}{L} C_{ox} V_{DS}} \Bigg|_{V_{DS} \to 0} \tag{1-8}$$

The main drawback of the field effect mobility (μ_{FE}) is neglecting the variation of mobility with respect to the gate voltage. This leads to inaccuracies in calculation of (μ_{FE}) which could be enhanced or degraded by applying gate voltage. Another drawback of field effect mobility (μ_{FE}) is that similar to the effective mobility, it is sensitive to the drain-source resistance. Field effect mobility offers some advantages: 1- Similar to the effective mobility it is calculated in the linear regime which means the charge distribution along the channel is uniform. Hence the concept of mobility being a proportionality constant between the velocity of carriers and electric field is appropriate. 2- Calculation of field effect mobility requires no knowledge about the threshold voltage. 3- the field effect mobility is not undefined like effective mobility at $V_{GS}=V_{TH}$. This method is the most popular method for channel mobility estimation.[29]

9

The difference between the saturation mobility and the effective and field effect mobilities is that saturation mobility is calculated in the saturation region. Saturation mobility is calculated by taking square root of the post pinch-off expression for I_D, then differentiating with respect to V_{GS} to obtain:

$$\mu_{sat} = \left. \frac{\left(\dfrac{d\sqrt{I_D}}{dV_{GS}}\right)^2}{\left(\dfrac{W}{2L}\right)C_{ox}} \right|_{V_{DS}>V_{GS}-V_{TH}} \tag{1-9}$$

The condition of $V_{DS}>V_{GS}$-V_{TH} is a condition required for the operation of the transistor in the saturation region. Among all the mobility evaluation methods, saturation mobility is the least used method. The main drawback is that it is calculated in the saturation region where the charge distribution and electric field are highly non-uniform. Hence the concept of mobility being a proportionality constant between the velocity of carriers and electric field is not applicable. In spite of this fact, saturation mobility has some advantages: 1- For evaluation of saturation mobility the threshold voltage is not required. 2- At $V_{GS}=V_{TH}$ the saturation mobility is not undefined 3- It is relatively insensitive to the drain-source resistance.[29]

As mentioned previously, TFTs are suitable for large area, low cost and flexible device applications. Large area flexible displays and low cost low-end electronic devices like RFID tags are some of the applications for TFTs. Both organic and inorganic semiconductors can be used in the active layer of the TFTs with each of them having their own advantages and disadvantages.[30] Organic materials suffer from lower mobility compared to their inorganic counterparts. In addition to that, only a limited number of stable *n*-type organic semiconductors are known.[31] On the other hand, most inorganic materials require high temperature processing steps and are not flexible. In the next section, we will describe some important characteristics required for TFTs in circuit applications.

1.4 Applications

Active matrix liquid crystal displays (AMLCDs), active matrix organic light emitting diodes (AMOLEDs), and radio-frequency identification tags (RFIDs) are some of the applications of thin film transistors.

1.4.1 Active Matrix Liquid Crystal Display (AMLCD):

The active matrix display has a semitransparent grid, which provides the required charge to the liquid crystal. In each pixel a thin film transistor is built in, which by acting as a switch, controls the voltage received by each pixel. Figure 1.4 shows the circuit of these LCDs.
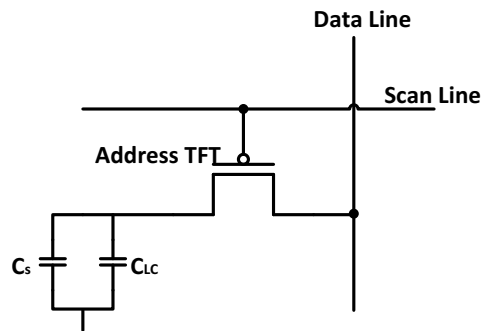
Figure 1-4 Circuit of the active matrix display.

As can be seen from figure 1.4, the conductive grid is connected via a TFT to each pixel. As can be seen from the figure 1.4, the gate and drain electrodes of the TFT are connected to the row and column electrodes, respectively. The source is connected to the liquid crystal. By applying the voltage to the rows line by line, the panel is activated. When the voltage is applied to the gate of TFT, the transistor is turned on. Hence the charge will flow from drain to source. These charges will be stored on the capacitor to preserve the voltage applied to the liquid crystal until the next refreshment cycle.[32]

1.4.2 Active Matrix Organic Light Emitting Diode Display (AMOLED):

Figure 1.5 shows the structure of the AMOLED.
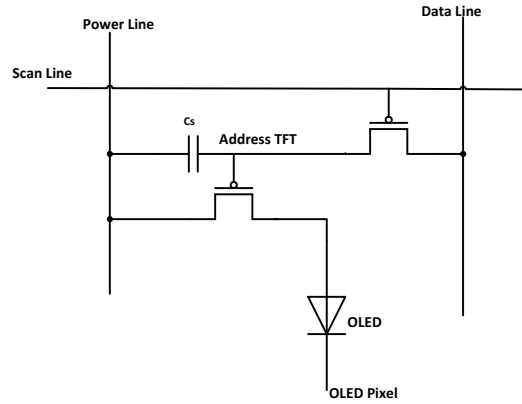
Figure 1-5 Circuit of AMOLED displays.

In this structure, two TFTs control the current directed to each pixel. By turning on one transistor, the capacitor connected to the gate of the other transistor is charged. Hence, the second transistor is turned on. The second transistor acts as the current source for the OLED which illuminates the pixel.[32]

1.4.3 **Radio Frequency Identification Tags (RFIDs):**

Figure 1-6 shows the structure of the RFID chip structure. RFID contains two parts: 1- RF circuits 2- logic circuits. Half-wave rectifier, shunt regulator, load modulator, and reset circuit are the RF circuit parts. Logic circuits consist of a ring oscillator, a read only memory (ROM), memory driver, and encoder.
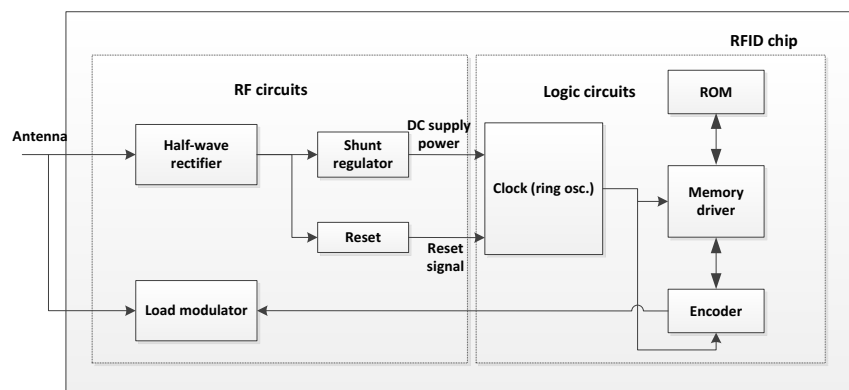
Figure 1-6 RFID chip architecture.

When the input antenna receives the RF input, the half-wave rectifier generates a DC voltage. The shunt regulator prevents excessive DC voltage being applied to the logic

circuit by dumping unnecessary current behind the rectifier. The reset off signal starts the operation of the logic circuits. The ring oscillator consists of a number of cascaded inverters and is responsible for producing clock signals. In response to the clock signal, the encoder generates the tag response.

TFTs can be utilized in low cost RFID applications. RFIDs operate in four main bands: low frequency band up to 135 kHz, a band at 13.56 MHz, a band at 900 MHz, and a band at 2.4 GHz. The low frequency range and the band at 13.56 MHz are the frequency bands that can be covered with certain types of TFTs. TFTs are used to fabricate different parts of the RFID circuits.

Sun fabricated a ring oscillator with 31 ns propagation delay using ZnO thin film transistors deposited using spatial ALD at atmospheric pressure and 200 $^{\circ}$C. The gate dielectric was Al_2O_3, which was deposited using a similar process. The mobility measured for these TFTs was 15 $cm^2V^{-1}s^{-1}$. These TFTs were utilized in fabricating seven stage ring oscillators with signal propagation delay of 31 ns/stage (> 2MHz oscillation frequency) at supply voltage of 25 V. These circuits have propagation delay of 100 ns/stage for supply voltage of 15 V.[33]

In addition to the oscillator, the rectifier can be fabricated using TFTs as well. Kawamura fabricated a full-wave rectifier using amorphous IGZO TFT.[34] The rectifier is composed of four TFTs with two of them in the diode configuration. This avoids the additional fabrication steps. The fabricated rectifier rectifies the wired input up to 25 MHz. A DC output voltage of larger than 5 V was obtained by rectifying a wireless input of 13.56 MHz from a 200 mW commercial reader/writer from a distance up to 65 mm. The authors derived the equations for maximum operating frequency of the bottom-gate top-contact TFTs and estimated a maximum operation frequency of 3 GHz for the non-quasi static operation and 240 MHz for quasi-static operation.[34] Ozaki fabricated an RFID chip for 13.56 MHz using IGZO TFTs on glass substrate. The TFT was used in the half-wave rectifier, load modulator, and ring oscillator. The RFID provided tag response with the minimum power supply of 5 V. The RFID tag was driven by an input power of 40 mW at

13

the distance of 70 mm.[35] Cho developed the oscillator and rectifier circuit using oxide TFTs. The rectifier converted the RF signal to DC voltage with an efficiency that was dependent on the RF input frequency. The maximum output DC voltage was obtained at an input frequency of 2.7 MHz. With the power supply voltage of 15 V, the oscillator operated at 813 kHz. With the DC voltage obtained from the rectifier, the oscillation frequency was 24 kHz.[36]

Organic materials are also used to fabricate RFID tags. Fiore built the first integrated organic 13.56 MHz RFID tag on flexible substrate.[37] In this method a planar near-field antenna was bonded to an RFID tag printed using complementary organic TFTs. Using an active envelope detector, which made the usage of ASK modulation with modulation depth as low as 20% possible, increased the input power of the rectifier. The RFID operated with an internally generated supply voltage of 24 V with the reading range of 2-5 cm and bit-rate of up to 50 bits/s.[37]

1.5 TFT Requirements for Circuit Applications

High mobility, high on/off current ratio, minimum threshold voltage shift, low leakage current, and low subthreshold slope are some of the required characteristics for TFTs in circuit applications. In specific applications, the requirements for some of the mentioned characteristics might become more important. The table below shows the important parameters in each application. (*) sign shows the most important characteristic for each application.

Table 1-1 Requirements for TFTs for different applications. (Adapted with permission from Ref[30]; Copyright John Wiley & Sons, Inc.)

TFT parameter	AMLCD (TFT as switch)	AMOLED (TFT as active driver)	RFID tags
Speed	Not important	Not important	High
Leakage current	Low(*)	Low(*)	Low
Current drive	Not as critical	Large(*)	Large
Threshold voltage	Low	Low	Low
On/off current ratio	Large	Large	Large
stability	High	High	High

In active matrix liquid crystal displays, the TFT behaves as a switch. Hence, emphasis is placed on reducing the leakage current of these TFTs. In the active matrix organic light emitting diodes, the TFT must supply enough drive current to turn on the OLED. Hence the on/off current ratio and current drive are the most important characteristics in an AMOLED. Speed is the most important parameter in the RFID tags due to the high frequencies used in these devices. Low threshold voltage is important in all applications for two reasons: 1- large dynamic range and 2- low voltage operation. High stability is required in all the applications. To obtain these requirements different approaches such as choosing the right material, device structure, and fabrication method might be used.[30] We will discuss each requirement for the TFTs in the next few sections.

1.5.1 **Speed**

In order to provide the required data rates, speed is an important requirement for RFID devices. The maximum operating speed of transistor is determined by the transit time (t_r), which is defined as the time it takes the charge carriers to travel from source to drain.

Transit time can be defined by the maximum switching speed of the transistor as follows[30]:

$$\frac{1}{t_r} = f_{max} \approx \frac{\mu V_{DS}}{L^2}$$

(1-10)

Due to non-idealities the maximum operation frequency is even lower than that predicted above. For a soluble organic semiconductor, with $\mu = 0.1$ cm^{2}V^{-1}s^{-1}, $V_{DS} = 10$ V and $L = 10$ μm, the maximum frequency according to the above equation will be $f_{max} \approx 10$ MHz. Hence, mobility, channel length, and patterning method are some important parameters that determine this maximum operating frequency for this transistor.

Mobility has an immense effect on the speed and current driving capability of the TFT. The mobility of TFTs has shown great improvement during recent years. The use of new gate insulators, thermal annealing, and optimizing the microstructure are some of the common ways used to improve the mobility in TFTs.[38] The effort is still ongoing to improve the mobility of these devices. By using high k dielectrics, the capacitive coupling between the channel and active layer increases.[38] Increased capacitive coupling results in higher charge concentration in the accumulation layer which will be useful in filling the traps and defects. This can enhance the mobility of the TFT.[38]

Inorganic can operate at frequencies much higher than organic materials due to their higher mobility. In flat panel displays, the refresh rate is in the 40-85 Hz range. Hence both organic and inorganic TFTs can be used for this application. The logic circuits for RFID tags operate at 100 kHz. Therefore, both organic and inorganic TFTs can be used. High mobility and small channel length are required to obtain high speed transistors. The mobility is generally affected by the crystal structure and defects in the case of ZnO. In organic materials, higher molecular ordering correlates with higher mobility. In the later sections we will survey some of the papers in both ZnO and organic TFT research that have reported high mobilities.

Reducing the channel length also has an important effect on f_{max}. The minimum channel length achievable is determined by the processing technology. As mentioned previously, the above equation only gives the upper limit of the operating frequency. In practice, the charging and discharging of parasitic capacitances during turn on and turn off reduce the maximum operating frequency. Hence minimization of parasitic capacitances is crucial. Choosing the right sizes for TFTs, improving the patterning techniques, and choosing the appropriate material are some useful techniques to reduce parasitic capacitances. In addition to small parasitic capacitances, low off current to reduce the power consumption and stability for analog circuits are the other important requirements for RFID TFTs.[30]

1.5.2 Leakage

In active matrix displays, low off current, low gate leakage current, sufficient drive current, small parasitic capacitance, and device uniformity are some of the desirable features of TFTs. Among these features, the minimum leakage current is the most important. This is because the charge in the TFT must be sustained during the off-state of the transistor. Improving the quality of the gate dielectric, minimizing the interface states, and reducing the interfacial stress are the main methods of leakage reduction. By isolating the transistors on the same substrate using patterning, parasitic leakage and cross talk can be reduced.[30]

1.5.3 Current Drive

In AMOLEDs, the TFT drives the OLED. So it is important that the amount of current be high enough to provide enough brightness by the OLED. To obtain high drive current, the transconductance of the TFT must be very large. Transconductance can be calculated as follows:

$$g_m = \left(\frac{dI_D}{dV_G} \right)_{V_D=const} = \frac{W}{L} \mu_n C_{ox} V_D \qquad (1\text{-}11)$$

As can be seen from the above equation, increasing the W/L and μ are the two primary ways to increase the transconductance and hence the drive current. In addition to that, choosing a dielectric with higher dielectric constant k and reducing the thickness of the

dielectric results in increase of C_{ox} and hence higher transconductance and drive current.[30]

1.5.4 Stability

Device stability is an important factor in all the applications of TFTs. The stability of the TFT is mainly dependent on the type of the material used in the active layer. Metal oxide and organic materials are some of the examples used as active layers in TFTs.

Most organic materials suffer from sensitivity to environmental parameters such as air, humidity, oxygen, and light. Changing the chemical structure of the material to make it more robust is one way to overcome this problem. Encapsulation is another method to improve the stability of the TFTs. Another issue in TFTs is the variation of the threshold voltage, which is caused by application of the gate bias for a long duration. The shift in threshold voltage is due to the charge trapping in the gate and dielectric. The quality of the dielectric and the dielectric-semiconductor interface are the main factors affecting the amount of trapped charge.[30]

Bias thermal instability is another important issue which needs to be taken into account in ZnO based TFTs. The pixel circuit of AMOLED contains two transistors: switching and driving transistors. The effect of mobility and threshold voltage variation can be alleviated by choosing the appropriate on and off voltage conditions. As for the driving transistor, the drain current determines the brightness of the OLED. Hence the time and temperature variation of mobility and threshold voltage must be limited. For example, if the threshold voltage changes by just 0.1 V, the illumination of the OLED changes by 20%. Hence the bias thermal instability of ZnO based TFTs must be minimized. Thus the bias instability of ZnO based TFTs under positive gate bias must be studied.[38] This issue will be discussed in more detail in the next sections.

Having a large bandgap makes ZnO a suitable candidate for transparent electronics. One of the obstacles hindering the usage of these devices in high-end TFT LCD panels, is light induced instability. Therefore the stability of the TFT devices against back light exposure has to be improved.[38]

1.6 Active Layers in Thin Film Transistors

1.6.1 Amorphous Silicon TFT

Amorphous silicon was the first material used in the active layer of TFTs. Uniformity and adaptability to low temperature processes are some of the advantages of amorphous silicon.[39] By passivation of silicon dangling bonds using hydrogen atoms, the performance of amorphous silicon TFT is improved.[40] Amorphous silicon TFTs exhibit a mobility in the range of 0.5-1 $cm^2V^{-1}s^{-1}$, on/off current ratio of 10^6, and turn on voltage in the range of 5-8 V.[41] These characteristics make these devices a suitable candidate for use in LCD panels. The structure used is a bottom gate structure in which the drain and source are located on the top of the device.[41]

Amorphous silicon mobility is insufficient for newer technologies that have emerged such as 3D TVs. In addition to low mobility, amorphous silicon is incompatible with flexible polymeric substrates.[42] Electrical instability is another drawback of amorphous silicon TFTs. Applying the gate voltage for a long duration shifts the threshold voltage. By designing the TFT to allow a shift in threshold voltage and by minimizing the duration of voltage being applied to the gate, the problem is alleviated for LCD TFTs. However, in OLED displays, the TFT is required to produce a specific current to drive the LED. Variations in threshold voltage will result in variation of current which will in turn affect the brightness of pixel.[41]

1.6.2 Low Temperature Poly-Silicon (LTPS) TFT

The low mobility of a-Si:H TFTs is the main motivation for investigating the low temperature polysilicon (LTPS) technology. The high mobility of polysilicon enables the integration of the polysilicon TFT with the organic light emitting diode.[43] As for AMLCD, polysilicon TFTs can be used both as the switch for pixels and the integrated driving circuitry.[44] Polysilicon active layers are generally deposited using LPCVD. The deposition is done in the pressure of P=100-200 mT and a temperature range of T=580-630 °C. Thicker deposited films have a larger grain size. Hence by increasing the film thickness the performance of the TFT from a mobility point of view is improved.[44] However, increasing the film thickness also increases the off current of the TFTs.[45] For

instance the mobility of films thinner than 1 μm is in the range of 5-10 $cm^2V^{-1}s^{-1}$.[46] This low mobility can be attributed to dangling and distorted bonds.[44] In addition to increasing film thickness, plasma hydrogenation can also be useful in passivation of the dangling bonds hence enhancing the electrical properties.[44]

One way to reduce the grain boundaries is by solid phase crystallization (SPC) of a-Si films deposited by LPCVD. In this method, the a-Si films deposited by LPCVD can be converted into polysilicon by 10-100 hr of annealing at 530-600 °C.[44] The drawback of this method is the long time required for annealing of the films.

Another method of making polysilicon TFTs, is by using excimer lasers which crystallize amorphous silicon. This technique results in polysilicon films with field effect mobilities higher than 100 $cm^2V^{-1}s^{-1}$.[47] Excimer lasers are lasers that emit in the UV region. The duration of these pulses is in the range of 10-30 ns. Si has two important characteristics, which makes excimer lasers suitable: With the bandgap of 1.1 eV, Si has a strong absorption in the UV region. Additionally, the small heat diffusion length (of approximately 100 nm) ensures obtaining high temperatures and melting at the surface without considerable heating of substrate. Hence this method offers two main advantages: since the temperature of the substrate does not increase significantly, this method is compatible with glass[48] and plastic[49] substrates; due to the melting and regrowing, the films also have very good crystallinity.[44] In this method the amorphous Si film is partially melted. The amount of melting depends on the energy of the laser. Hence the film has two layers: An upper layer, which consists of large grains and lower layer with small grains, which undergoes rapid crystallization.[50] By increasing the energy of the laser, the size of the grains increases as well. The boundary level is the case where the whole film excluding some small crystalline clusters is melted. This is called the super lateral growth (SLG).[44] Using the SLG polycrystalline growth in the TFTs results in high field effect mobility of 300-400 $cm^2V^{-1}s^{-1}$.[51] The drawback of this method is the non-uniformity of the grain sizes, which results in non-uniformity in TFT performances.[44]

Combination of the SPC and ELC also introduces an effective method to grow polycrystalline films.[52] Based on this method, the large highly defective grains obtained with SPC are melted by an excimer laser. In this method, the bottom unmelted layers are the seed layers for the melted layers. Hence the grain size will remain unchanged while the in grain defects will be filled.[44]

In spite of the superior performance of LTPS compared to amorphous silicon, one major drawback hinders its wide usage: multiple process steps and lithography masks result in high manufacturing costs. However, there are some applications where the LTPS TFTs could be used. The first application is for the integration of the driver circuits on the glass substrates. Unfortunately, a-Si TFT is not fast enough for the driver circuit applications. Due to the higher mobility of LTPS TFTs, they can be used for the driver circuits. Another potential application of the LTPS TFT is for the OLED display. Generally, in the OLED display systems, obtaining high drive current is crucial. The higher mobility of the LTPS TFTs makes them capable of providing the required current.[41]

To conclude, the low mobility of a-Si:H motivates the usage of LTPS thin films. In spite of obtaining high mobility values for LTPS films using different methods, multiple process steps and lithography masks make this method an expensive method hence limiting the application to specific cases such as driver circuits and OLED displays. Alternative active layers such as metal oxide and organic semiconductors can be used for lower cost applications.

1.6.3 Metal Oxide Semiconductor TFT

Metal oxide semiconductors are another group of semiconductors which can be used in the fabrication of TFTs. Metal oxide semiconductors are inherently highly doped *n*-type materials. This high doping value is attributed to the oxygen vacancies.[41] Metal oxide semiconductors can be fabricated using binary oxides like ZnO[53,14,54,55], SnO_2[7, 9], In_2O_3[56,57] or multiple component oxides such as indium gallium zinc oxide (IGZO)[58,59,21,60], indium zinc oxide (IZO)[61,20], hafnium indium zinc oxide (HIZO)[62,63]. The most common method of deposition for these films is sputtering although other methods of deposition such as solution processing[54, 64,60] also exist. The oxygen stoichiometry can be controlled by either controlling the oxygen pressure in the chamber

during deposition or by annealing the thin films after deposition. The majority of these materials are poly-crystalline, which based on the deposition conditions and annealing temperatures, could exhibit mobility values in the 1-100 $cm^2V^{-1}s^{-1}$ range.[41]

In the case of binary compounds, large differences are observed for the performance of TFTs. SnO_2 is one of the binary oxides used as the active layer of the TFT.[9,7,65,66] The main drawback in using SnO_2 as the active of the TFT is the depletion mode behavior of the device which means a voltage must be applied to the gate to turn the device off. Various ways have been proposed to overcome this issue. One way is by decreasing the film thickness to reduce the current value from the bulk of the films. Presley used this method to obtain enhancement mode operation for SnO_2 TFTs. SnO_2 was deposited using RF magnetron sputtering with varying thickness values of 10-20 nm. Field effect mobilities of 0.8 $cm^2V^{-1}s^{-1}$ and 2 $cm^2V^{-1}s^{-1}$ were measured for enhancement mode and depletion mode devices, respectively.[67]

SnO_2 films have also been deposited using solution processing methods. Huang also fabricated an enhancement mode solution processed SnO_2 TFTs with Al_2O_3 gate dielectric. The solution processed Al_2O_3 gate dielectric creates a coherent interface with SnO_2 resulting in the device performance improvement. Average mobility of 96.4 $cm^2V^{-1}s^{-1}$, current on to off ratio of 2.2×10^6 and threshold voltage of 1.72 V were measured for these TFTs.[68]

Similar to SnO_2, In_2O_3 TFTs also suffer from depletion mode behavior due to high carrier concentration. Wang used the hybrid approach taking advantage of the interesting properties of In_2O_3 like wide bandgap, high mobility, high transparency as the active layer with nanoscopic dielectric materials. Hence, advantages of high mobility inorganic semiconductor is combined with ultrathin high capacitance-low leakage current organic dielectric. The fabricated TFT exhibit mobility values of 120 $cm^2V^{-1}s^{-1}$, on-off current ratio of 10^5, and near zero threshold voltage.[69] Liu also fabricated a fully solution processed enhancement mode In_2O_3 TFT using ultrathin ZrO_x gate dielectric. The ZrO_x gate dielectric showed an amorphous structure with a leakage current density of 10^{-9}

Acm^{-2} at 2 MVcm^{-1} and high breakdown field electric field (7.2 MVcm^{-1}). In$_2$O$_3$ TFTs with annealed ZrO$_x$ layer at 250 ^{o}C showed field effect mobility values of 23.6 cm^{2}V^{-1}s^{-1}, on/off current ratio of 10^7, and threshold voltage of 0.13 V.[70] Zou controlled the electrical properties of In$_2$O$_3$ NW FETs by doping the film with various metals (Mg, Al, and Ga) thus converting depletion mode devices to enhancement mode devices. By changing the metal content the threshold voltage value can be changed. Mg doped In$_2$O$_3$ NW FETs exhibited high saturation current (0.5 mA), on/off current ratio (>10^9), and field effect mobility (110 cm^{2}V^{-1}s^{-1}).[71]

Ga$_2$O$_3$ is another active layer used in the active layer of the TFTs. Matsuzaki fabricated Ga$_2$O$_3$ TFTs using epitaxial deep ultraviolet Ga$_2$O$_3$ active layer deposited on Al$_2$O$_3$ (0001) substrate by pulsed laser deposition. The channel filed effect mobility of this device was only 5×10^{-2} cm^{2}V^{-1}s^{-1}. Thomas fabricated Ga$_2$O$_3$ TFTs using atmospheric ultrasonic spray pyrolysis at low temperatures. The deposited *n*-type Ga$_2$O$_3$ thin films exhibit maximum mobility values of 2 cm^{2}V^{-1}s-^{1}.[72] It can be seen that due to the large number of traps Ga$_2$O$_3$ has a lower mobility compared to other oxides.

Among the oxides ZnO shows the most reasonable behavior which can be deposited using different techniques like pulsed laser deposition (PLD)[73,53,74], atomic layer deposition (ALD)[75,33,76] RF sputtering[14,77,78], and solution processing[1,54,79]. Hoffman fabricated the first transparent ZnO thin film transistor using ITO substrates. The gate dielectric of this TFT was ATO and the ZnO active layer was deposited using ion beam sputtering in 10^{-4} Torr Ar/O$_2$ pressure. Threshold voltage and mobility of the fabricated devices changed in the range of 10-20 V and 0.3-2.5 cm^{2}V^{-1}s^{-1}, respectively with on/off current ratio of 10^7. Visible light has negligible influence on the performance of the TFT. However, exposing the TFT to UV light results in large photoconductive currents.[12] Masuda fabricated ZnO thin film transistors using the PLD method at 450 ^{o}C and oxygen pressure of 3 mTorr. Additionally a double gate layer of SiO$_2$-SiN$_x$ was used to suppress the leakage current hence obtaining on/off current ratio of 10^5.[13] The drawback of Masuda's TFT is the high temperature used for ZnO thin film deposition, which makes it incompatible with plastic substrates. Fortunato fabricated ZnO thin film transistor using

RF magnetron sputtering at room temperature. The fabricated TFT exhibited a mobility of 27 $cm^2V^{-1}s^{-1}$, threshold voltage of 19 V, and on/off current ratio of 3×10^5. In the visible range of the spectrum this film showed 80% optical transmission.[80] Carcia used RF magnetron sputtering to fabricated ZnO TFTs. The highest observed mobility was 2 $cm^2V^{-1}s^{-1}$ with on/off current ratio of 10^6. The measured resistivity value for the deposited films was 10^5 Ωcm and the optical transparency for wavelengths higher than 400 nm was higher than 80%.[14] Carcia investigated the effect of ALD deposited gate dielectric layer on the performance of RF sputtered ZnO TFTs. HfO_2, $HfSiO_x$, and Al_2O_3 were the gate dielectrics tested. Devices with HfO_2 dielectric had a mobility of 12.2 $cm^2V^{-1}s^{-1}$ and threshold voltage of 2.6 V. The Al_2O_3 devices showed a temperature dependent behavior. For instance the Al_2O_3 devices fabricated at 200 ^oC, had a mobility of 17.6 $cm^2V^{-1}s^{-1}$ and threshold voltage of 6 V. In general HfO_2 devices had lower threshold voltage and the Al_2O_3 devices had a lower gate leakage current.[76]

Atomic layer deposition is another method for depositing ZnO thin film transistors. Levy reported ZnO thin film transistors fabricated using the atmospheric atomic layer deposition with alumina gate dielectric. All the deposition steps are done at temperatures below 200 ^oC. The devices show mobility values higher than 10 $cm^2V^{-1}s^{-1}$, near zero turn-on voltage, and on/off current ratios of 10^8.[81] Lim reduced the deposition temperature to 150 ^oC using nitrogen doped ZnO ALD. By varying the nitrogen doping of the ZnO, the electrical properties were controlled. The TFTs were inverted staggered type with Al_2O_3 gate dielectric, which was also deposited using ALD. This device showed saturation mobility value of 6.7 $cm^2V^{-1}s^{-1}$, on/off current ratio of 9.46×10^7.[75]

Lim compared the ZnO TFTs deposited using ALD and RF sputtering. The deposition temperatures of ALD ZnO varied in the range of 100-250 ^oC. XRD results revealed that both ALD and RF sputtered films have (002) orientation. At $T<125$ ^oC, ALD ZnO films have high resistivity (>10 Ω cm) and low mobility (<3 cm^2V^{-1}s-1). The ALD ZnO films deposited at higher temperature have lower resistivty (<0.02 Ω cm) and higher mobility (> 15 $cm^2V^{-1}s^{-1}$). Sputtered ZnO films have higher resistivity compared to ALD at most of the growth conditions.[82]

Pulsed laser deposition is another method of depositing ZnO thin films. Zhao studied the structural, optical, and electrical properties of ZnO thin films deposited using PLD. The deposited ZnO films were grown on single crystal Si (100) and quartz glass substrates using KrF excimer laser with the wavelength of 248 nm. Even at low temperature deposition of 200 $^{\circ}$C the films show the *c*-axis orientation. Increasing the substrate temperature and oxygen pressure, the crystallinity improves. Hall measurement showed that the resistivity of the films increases with temperature and oxygen pressure.[83] Shin fabricated ZnO TFT with PLD method and investigated the effect of deposition condition (oxygen pressure and substrate temperature) on the performance of TFT. The mobility of the TFTs showed a variation in the range of 2.4 to 12.85 $cm^2V^{-1}s^{-1}$ based on the deposition parameters. The on/off current ratio changed in the 10^2-10^6 range. The best performance (μ_{FE}=12.85 $cm^2V^{-1}s^{-1}$) was obtained for oxygen pressure of 26.68 Pa and substrate temperature of around 400 $^{\circ}$C.[73]

Solution processing technique is another method for depositing ZnO thin films. Ohyama studied the effect of heat treatment, withdrawal speed of substrate, and film thickness on the orientation of the crystal growth. The highest (002) orientation was obtained for samples preheated at 300 $^{\circ}$C for 10 minutes and post-heated at 600-800 $^{\circ}$C for an hour. Reducing the withdrawal speed of the substrate increased the density of the films and preferred orientation. Thinner films also had less crystal orientation, which proves that there is a critical thickness for obtaining highly oriented crystals.[84]

Ghosh studied the influence of annealing temperature on the electrical and optical properties of ZnO thin films deposited using dip coating technique. The films were annealed in nitrogen, air, and vacuum in the temperature range of 400-650 $^{\circ}$C. Among all the films, the films annealed in air at 650 $^{\circ}$C is the only film that shows the slight orientation of (002). Two opposite trends are observed for the crystallite size, carrier concentration, and resistivity around a temperature close to the decomposition temperature. The film annealed at 500 $^{\circ}$C in vacuum had the highest carrier concentration of 8×10^{18} cm^{-3} (equivalent resistivity of 2.25×10^{-1} Ω cm). All the films are highly

transparent in visible region and show a sharp absorption edge in the UV region. The optical bandgap shows negligible change for the films annealed at temperatures below 500 °C.[85] Lee studied the effect of drying conditions on electrical and optical properties of ZnO films deposited by spin coating. The films dried at 350 °C and annealed at 600 °C showed the (002) orientation with less resistivity compared to other films. The second heat treatment at 500 °C reduced the resistivity value of the films to 9.9×10^{-2} Ω cm.[86] The solution processed ZnO thin films will be studied in greater detail in the next chapter.

Multicomponent oxides combine the interesting features of each of the oxides hence improving the device performance. Indium zinc oxide (IZO) is one of the complex oxides with interesting features such as a high field effect mobility (20-50 $cm^2V^{-1}s^{-1}$). Yaglioglu fabricated depletion IZO TFT using DC sputtering deposition at room temperature. The source, drain, and channel were all formed from IZO. By controlling the oxygen content in the chamber during deposition, carrier concentration was controlled. Amorphous high concentration IZO with concentration of 3.3×10^{20} cm^{-3} was used for source-drain contacts where as the IZO used in the channel had charge carrier concentration of 2.1×10^{17} cm^{-3}. The fabricated devices exhibited mobility of 20 $cm^2V^{-1}s^{-1}$ and on/off current ratio of 10^8.[87] Paine fabricated the same device with the conditions that were compatible with plastic substrates. The optically transparent devices showed a depletion mode behavior with saturation mobility of 15 $cm^2V^{-1}s^{-1}$, on/off ratio of 10^6, and threshold voltage of -5 V.[88] Choi fabricated solution processed IZO TFTs by annealing at 500 °C. The TFTs exhibit mobility values of 7.3 $cm^2V^{-1}s^{-1}$, threshold voltage of 2.5 V, and current on/off ratio of 10^7. The turn on voltage of this transistor is -20 V, which shows it is a depletion mode device.[19]

IZO thin films can be deposited using the solution processing method. Cheng fabricated IZO TFTs with cross-linked poly-4-vinylphenol (PVP) on polyimide (PI) substrates. These TFTs were fabricated using solution processing and microwave annealing. The depletion mode device had a field effect mobility of 6.9 $cm^2V^{-1}s^{-1}$, a threshold voltage of 2 V, and on/off current ratio of 10^6.[89] Koo optimized the composition and film thickness for high performance solution processed IZO thin films. With the composition of In/Zn

equal to 50/50 and film thickness of 10 nm best operating conditions are obtained. Field effect mobility of 0.54 $cm^2V^{-1}s^{-1}$, on/off ratio of larger than 10^7, and threshold voltage of 1.9 V.[20]

The main drawback of the IZO devices is depletion mode behavior due to high charge carrier concentration. Doping IZO films with dopants like hafnium (Hf) and gallium (Ga) suppresses the carrier concentration hence contributing to enhancement operation. Kim fabricated amorphous HIZO thin films and showed adding Hf element suppresses the growth of columnar structure and reduces Hall mobility and carrier concentration. The fabricated TFTs had a mobility of 10 $cm^2V^{-1}s^{-1}$, subthreshold swing of 0.23 V/decade, and on/off current ratio of 10^8. The Hf ions also result in more stability of the TFTs.[90]

IGO is another amorphous complex oxide used in TFT fabrication. As mentioned before In_2O_3 TFTs suffer from depletion mode behavior due to high number of charge carrier concentrations. By doping the In_2O_3 with Ga^{3+}, which makes strong bonds with oxygen, the oxygen deficiency is controlled. Ebata fabricated enhancement mode polycrystalline IGO TFT by DC sputtering. The TFT showed field effect mobility of 39 $cm^2V^{-1}s^{-1}$, a threshold voltage of 1.4 V, and subthreshold slope of 0.12 V/decade. The high mobility value can be attributed to the large grain size of the deposited films (10 μm).[91] Goncalves studied the effect of oxygen pressure on the IGO films deposited with sputtering. In the absence of oxygen the films were rough and polycrystalline. XRD results show these films have strong (002) orientation. However, when oxygen was introduced to the chamber the films structure was amorphous and films were much more smooth. By changing oxygen pressure by one order of magnitude, the resistivity changes in the 1.8×10^{-3} to 10^4 Ω cm. The work function variation range was from 4.53 to 4.84 eV. The maximum Hall mobility of 25.5 $cm^2V^{-1}s^{-1}$ with oxygen pressure of 2.5×10^{-3} Pa. The films deposited in the presence of oxygen are all transparent and the transparency value is independent of oxygen pressure. The films deposited in the absence of oxygen are opaque. The TFTs fabricated at room temperature showed mobility values of 43 $cm^2V^{-1}s^{-1}$, on/off current ratio of 10^8, threshold voltage of 3 V.[92]

Park fabricated IGO TFTs using solution processing methods and optimized the crystallinity and electrical and optical properties based on the gallium content. XRD results show that by replacement of indium with gallium, the lattice shrinks. The optimum Ga/In ratio was 0.35. TFTs using this ratio showed a mobility value of 3.59 $cm^2V^{-1}s^{-1}$, a threshold voltage of 0.1 V, on/of current ratio 8.2×10^7, and subthreshold slope of 0.9 V/decade.[93] Jeong studied the metal salt precursor effect on the electrical characteristics of low temperature sol gel deposited IGO films. Using indium chloride and gallium nitrate as metal precursors and annealing the deposited films at 300 ^{o}C, TFTs with mobility values of 8×10^{-3} $cm^2V^{-1}s^{-1}$ and subthreshold swing of 16.8 V/decade were fabricated. The IGO films deposited using these precursors and annealed at 250 ^{o}C were inactive. TFTs with IGO thin films deposited with indium nitrate and gallium nitrate and annealed at 300 ^{o}C, showed field effect mobility of 1 $cm^2V^{-1}s^{-1}$ and subthreshold swing of 4.2 V/decade and the IGO films annealed at 250 ^{o}C were still active. The difference in the electrical properties of the two TFTs was attributed to the remaining impurities. Hence it was concluded that the precursors with low decomposition temperatures must be chosen.[94]

AC/DC converters and ring oscillators are two of the sample applications of IGO TFTs. Mcfarlane used IGO TFTs for implementing AC/DC converter. The fabricated rectifiers operate till 20 MHz.[95] Presley implemented highly transparent ring oscillators using IGO TFTs. The utilized TFTs exhibited a mobility of 7 $cm^2V^{-1}s^{-1}$ and turn on voltage of 2 V. The five stage oscillator fabricated with these TFTs oscillates with the frequency of 2.2 kHz with the gate and drain of the load transistor biased at 30 V. The maximum observed oscillation frequency (9.5 kHz) was observed at 80 V bias.[96]

Zinc tin oxide is another amorphous complex oxide used in TFT fabrication. Zinc tin oxide (ZTO) main application is for transparent conductive applications.[97,98,99,100] Chemical stability against etching and oxidation[97], physical robustness[101], and having a smooth surface[101] are some of the interesting features of this material. Chiang fabricated transparent TFTs using ZTO amorphous oxide. The devices annealed at 300 ^{o}C after deposition showed a mobility behavior of 5-15 $cm^2V^{-1}s^{-1}$. Annealing at 600 ^{o}C improved

the crystallinity of the films and field effect mobility values were in the 20-50 $cm^2V^{-1}s^{-1}$ range. The turn on voltage for the devices with films annealed at 300 ^{o}C was 0-15 V whereas devices with films annealed at 600 ^{o}C was -5 to 5 V. In both cases the on/off current ratio was higher than 10^7. This shows that even at relatively low temperatures (300 ^{o}C) the performance shows slight degradation.[17] Jackson fabricated ZTO TFTs using sputtering with silicon oxynitride (SiON) gate dielectric on flexible polyimide substrates. The gate dielectric was deposited using PECVD at 300 ^{o}C. The fabricated TFTs showed mobility of 14 $cm^2V^{-1}s^{-1}$, turn-on voltages of -17 V, and on/off current ratios of 10^6.[102] Hong fabricated ZTO TFTs with reactive sputtering using metal target. The oxygen pressure and the total pressure were changed to obtain optimum performance. The oxygen pressure of 0.8 mTorr and total pressure of 30 mTorr result in the optimum outcome. The devices fabricated at 500 ^{o}C give mobility values of 32 $cm^2V^{-1}s^{-1}$, turn on voltage of -4 V and on/off current ratio of 10^7. DC sputtering and RF magnetron sputtering showed similar results.[103]

ZTO Seo fabricated solution processed ZTO TFTs by spin coating method. The amorphous transparent films were annealed at 400 ^{o}C and 500 ^{o}C. The fabricated TFTs showed enhancement mode behavior. The TFT annealed had saturation mobility of 2.49 $cm^2V^{-1}s^{-1}$ and threshold voltage of 5.93 V where as TFTs annealed at 500 ^{o}C had a saturation mobility of 14.11 cm^2V^{-1}-s^{-1} and threshold voltage of 1.7 V. The on/off current ratio for both devices was higher than 10^8.[18] Similarly Chang used spin coating method for the deposition of ZTO. The deposited films are highly uniform, amorphous (proven by XRD) and transparent (95% in the visible part of the spectrum). Enhancement mode MISFETs were fabricated by this spin coated ZTO layer. The MISFET showed a mobility value of 16 $cm^2V^{-1}s^{-1}$, turn on voltage of 2 V, and on/off current ratio of 10^5.[104] Jeong investigated the thermal behavior of ZTO precursors and effect of annealing temperature on the performance of ZTO TFTs. By annealing of up to 500 ^{o}C, the thermal decomposition of organic residues is complete. The ZTO TFT (with 30 mol% Sn) annealed at 500 ^{o}C shows a field effect mobility of 1.1 $cm^2V^{-1}s^{-1}$, on/off current ratio of 10^6, and threshold voltage of 1.9 V. Reducing the Sn content to 20 mol% and 0 mol%

degraded mobility values to 0.3 and 0.002 $cm^2V^{-1}s^{-1}$, respectively. Hence it was confirmed that 30 mol% Sn content results in the optimum performance.[105]

Jeong studied the stability of the solution processed ZTO under gate bias stress. While applying a positive bias stress shifts the transfer curve in the positive direction without mobility or subthreshold swing changes, negative bias stress has no effect on the transfer curves. However, after 10 min relaxation at room temperature the devices restored their original characteristics. The authors attributed the charge trapping to the charge trapped at the interface and also active layer of ZTO TFT. The oxygen vacancies could be the possible source of traps. The solution processing method also affected the instability behavior of the TFT. For instance ink-jet printed TFT has a larger threshold voltage shift compared to the spin coated TFT, which is due to the nanopores present in the inkjet printed films.[106]

One of the other oxides used for the active layer of the TFTs is IGZO. As mentioned previously, in spite of all the advantages of the IZO devices, the high carrier concentration makes the enhancement mode operation difficult. One method to overcome this issue is by reducing the thickness of the IZO films. For instance active layer of 10 nm thickness can be used instead of 40 nm. By reducing the thickness of the active layer, the depletion region created by the adsorbed oxygen at the surface of the film can extend to the dielectric-semiconductor interface hence contributing to the enhancement mode behavior.[2] Doping the IZO films with appropriate elements is another method of suppressing the carrier concentrations. Doping the IZO films with elements like hafnium[62,90,63](discussed before) and gallium[107,58,59] reduces the charge carrier concentration. These elements form strong bonds with oxygen suppressing the charge carrier concentrations.

Nomura fabricated amorphous IGZO TFTs on polyethylene terephthalate substrates using the pulsed laser deposition method (PLD). The Hall effect mobility measured was around 10 $cm^2V^{-1}s^{-1}$. The optical bandgap estimated with the Tauc plot was 3 eV. The saturation mobility of 6-9 $cm^2V^{-1}s^{-1}$ and on/off current ratio of 10^3. The devices showed the same

behavior after bending.[16] Yabuta fabricated IGZO TFTs by using RF magnetron sputtering which gave better results compared to the previous work. The gate dielectric was Y_2O_3 which was also deposited with RF magnetron sputtering. By changing the mixture of sputtering gases $O_2/(O_2+Ar)$ from 3.1% to 3.7% the conductivity of the films was changed from 10^{-3} to 10^{-6} $\Omega^{-1}cm^{-1}$. The top gate enhancement mode TFT showed mobility of 12.1 $cm^2V^{-1}s^{-1}$, on/off current ratio of 10^8, and subthreshold slope of 0.2 V/decade.[108]

IGZO thin films have been deposited using solution-processing techniques as well.[58,109,110,111,112] Lim reports using sol-gel process for fabricating IGZO active layer for thin film transistors. By varying the content of Ga in the active layer the effect of Ga concentration on the electrical behavior of the thin film was studied. Changing the Ga ratio from 0.1 to 1, changes the electrical behavior of the active layer from conductor to semiconductor. The devices sintered at 300 ^oC showed a mobility value of 0.2 $cm^2V^{-1}s^{-1}$. By increasing the sintering temperature to 400 ^oC the mobility value increases to 1-2 $cm^2V^{-1}s^{-1}$.[109]

By adjusting the composition ratio of different elements with respect to each other the electrical properties of IGZO TFTs can vary. Kim studied the effect of composition ratio on the performance of IGZO TFTs. By increasing the In/(In+Zn+Ga) molar ratio, the carrier concentration increased from 2.2×10^{14} cm^{-3} to 5.43×10^{18} cm^{-3} while the mobility increased from 1.79 to 6.95 $cm^2V^{-1}s^{-1}$. Increasing the Ga content reduced the mobility and charge carrier concentration. It is observed that Indium rich TFTs (>60%) are depletion mode devices due to large carrier concentrations. The Zn content changes the subthreshold characteristics of the TFTs. The subthreshold slope of TFTs improves by increasing the content of Zn to 70% and degrades for content higher than 80%. Improvement in subthreshold slope is due to reduction of shallow traps below conduction band or reduction of interfacial states. Increasing the Zn molar ratio (>80%) results in the polycrystalline film structure and higher surface roughness which increases the shallow traps and interfacial state densities degrading subthrehsold characteristics. By changing the In:Ga:Zn ratio, the mobility of 0.5-2 $cm^2V^{-1}s^{-1}$, threshold voltage of -5 to 5 V, and

subthreshold slope of 1.5-2.5 V/decade is obtained. By using larger indium ratio (60%-70%) higher mobilities >2 cm^{2}V^{-1}s^{-1} were obtained. However, the threshold voltage shifts to the -70 to -90 V which makes the devices impractical.[113]

Hwang studied the effect of annealing on the solution processed IGZO TFTs. Increasing the annealing temperature from 300 ^{o}C to 600 ^{o}C enhanced the saturation mobility from 0.003 cm^{2}V^{-1}s^{-1} to 6.415 cm^{2}V^{-1}s^{-1} and the on/off current ratio from 4.5×10^4 to 3.9×10^7 and the threshold voltage from 13.62 V to -37.72 V. It was observed that devices annealed at 400 ^{o}C showed enhancement behavior and good on/off current ratio with reasonable mobility.[58]

Suresh studied the effect of bias stress on IGZO transistor performance. Applying a gate bias stress of IGZO TFTs results in the parallel shift of threshold voltage without changes in mobility or subthreshold swing. This threshold voltage shift is logarithmically dependent on the duration of bias stress.[114]

To conclude, among the binary oxides SnO$_2$ and In$_2$O$_3$ TFTs, in spite of higher mobility values, suffer from depletion mode behavior due to higher charge carrier concentrations. This increases the power consumption and complicates the circuit design. On the other hand Ga$_2$O$_3$ suffers from low mobility due to the large number of traps. Among all the binary oxides, ZnO shows the most reasonable behavior. ZnO thin films can be deposited using solution processed and vacuum based methods. The solution processing method is a cheap and easy method with a high throughput which can be used for ZnO thin film deposition. Using the complex oxides the interesting features of different oxides can be utilized.

1.6.4 Organic Semiconductors

Organic semiconductors are another group of semiconductors used in TFT fabrication. Unlike the conventional Si technology, organic thin film transistors (OTFTs) use low temperatures for deposition, which makes them compatible with the plastic substrates. In addition, organic materials can be solution processed which has the potential of replacing

more complicated vacuum based processes.[115] The highest mobility of organic semiconductors is in the range of 1-10 $cm^2V^{-1}s^{-1}$.[116,117,118] Due to this important limiting factor, OTFTs are incapable of replacing high speed inorganic TFTs. However, organic materials have a great potential for cases were their unique properties could be useful. Electronic newspaper, smart tags, and large area flexible displays are some of the applications OTFTs can be utilized.[115]

The nature of charge transport in organic materials is different from that well-ordered inorganic materials. Due to the tight binding of atoms via covalent bonds in inorganic materials, the charge carriers move as highly delocalized plane waves. These materials have a very high mobility, which is limited by the lattice vibration. Hence increasing the temperature results in the degradation of mobility.

Band transport is not valid for disordered organic semiconductors. In these semiconductors, charge transport occurs by hopping between localized states. Phonons can contribute to hopping. As a result by increasing the temperature mobility is enhanced.[119] For highly ordered organic semiconductors like pentacene the boundary between band transport and hopping transport can be observed. At temperatures below 250 K band transport is the dominant charge transport mechanism.[119] In the low temperatures very high mobility values are reported. For instance in ultrapurified naphthalene, anthracene, and perylene time of flight drift mobilities of up to 400 $cm^2V^{-1}s^{-1}$ were measured at low temperatures.[120] This high measured mobility can be attributed to the vibrational energy of molecules being lower than the intermolecular bonding energy. Hence phonon scattering is reduced, enhancing the mobility. At temperatures close to the room temperature, the vibrational energy increases resulting in enhanced phonon scattering and mobility reduction. At these temperatures the hopping mechanism becomes the dominant charge transport method replacing the band transport. Increasing the temperature assists with the hopping transport. Thus, it can be concluded that by increasing the temperature, the mobility value rises.[119]

The described methods are not the only methods of charge transport in organic semiconductors. For instance, there are papers in the literature that report thermally activated transport in single crystal pentacene, quaterthiophene, and hexathiophene. This behavior can be explained by the coulomb blockade transport. In this transport model, the coulomb forces between electrons can hinder charge transport. This phenomenon occurs when the tunnel resistance, R_T, is large ($>>h/e^2$) and the charging energy (e^2/C) is larger than kT where h and k are Planck and Boltzmann's constant, respectively and C is the capacitance between the two sites.[121] Schoonveld demonstrated that OTFTs can be considered as array of sites separated by tunnels. Due to the small capacitances of sites, the charging energy becomes dominant at room temperature and hence a thermally activated transport is observed.[121] The advantages of organic materials like flexibility and light weight has encouraged researchers to find new applications for these materials. Organic inverters[122], ring oscillators[123,124] memories[125,126], RFIDs[127], solar cells[128,129], sensors[130,131], and drivers for flexible displays[132] are some these emerged applications.

In spite of these new applications, there are still some challenges that need to be overcome. The characteristics of organic materials change with time. Hence, more research needs to be done to overcome the stability issues of these materials. Additionally, organic semiconductors are sensitive to oxygen and water.[133] Lack of reliable n-type organic semiconductors is another issue hindering the extensive usage of organic materials.[134] Due to their lower mobility compared to inorganic semiconductors, organic semiconductor can not be utilized in high speed applications.[133]

Hence, it can be concluded that using each type of material as the active layer of the TFTs has its own advantages and disadvantages. In spite of their advantages such as flexibility and lightweight, organic materials suffer from low mobility and stability issues. As a result the organic materials are used in low frequency operations where flexibility and lightweight are crucial. Hence it is important to find the suitable material for the specific application. In the rest of the thesis we will focus on ZnO thin films and their applications in TFTs and photodetectors.

1.7 Summary

In this chapter, we first described with the fundamentals of thin film transistor operation. We discussed some of the applications of these devices and requirements for each of these applications. Some of the active layers used for the TFTs were introduced and the advantages and disadvantages of each of these TFTs were discussed.

2 ZnO Thin Films

Inorganic semiconductors such as amorphous silicon and polysilicon are used extensively in thin film transistors. Low mobility of electrons, low current drive levels, and low on/off ratios are some of the drawbacks of these technologies.[53] Organic materials have also been utilized to make flexible transistors. Low mobility, low current density, process-dependent performance variations, and reliability are some of the challenges that need to be overcome for these materials.[135]

Recently there has been a lot of interest in ZnO. ZnO is a direct wide bandgap material ($E_g = 3.3$ eV) attractive for multiple applications in optoelectronics. ZnO and GaN (also a large band-gap semiconductor) have some applications in common. However, ZnO has some advantages over GaN. ZnO has an exciton binding energy of 60 meV, which is 2.4 times the thermal energy at room temperature ($kT = 25$ meV). This makes light emission at room temperature feasible. ZnO is highly resistant to high energy radiation which is a useful property in space applications. Unlike GaN, thin films of ZnO can be made by solution processing. Easy wet chemical etching is another important feature of ZnO, which makes the fabrication of small size devices possible. Zn is also much more abundant in nature compared to Ga and In. ZnO can also be used in fabrication of thin film transistors. Due to the insensitivity of ZnO to visible light, the protective covering for preventing light exposure can be removed. ZnO also has a high saturation velocity and breakdown field and is also a piezoelectric material. These two features make ZnO a suitable candidate for power electronics. Due to the difficulty in obtaining p-type ZnO, one strategy consists of using ZnO to form heterojunction devices with other p-type materials. For instance, due to sensitivity to air and humidity generally n-type organic materials generally have severe stability issues. Hence n-type ZnO can be combined with p-type organic materials to form heterojunction devices.[136]

ZnO is not a newly discovered material. Many important characteristics of ZnO have been studied in the past few decades. With all the interesting features mentioned above in addition to being well known for decades, one might ask the legitimate question as to what has hindered the extensive usage of ZnO? The main obstacle in using ZnO is the

difficulty in controlling the type and degree of electronic conduction. In spite of some initial progress, a reliable and reproducible method for growing *p*-type ZnO has not yet been developed. Likewise, control over the *n*-type conductivity in unintentionally doped ZnO is also inadequate. Due to the difficulty in obtaining *p*-type ZnO, the implementation of heterojunction devices and/or complementary logic with other *p*-type materials is a proposed route forward for ZnO technologies.

Vacuum deposition and solution processing are the two main methods of depositing ZnO thin films. Each method has its own advantages and disadvantages. The films deposited using vacuum deposition methods like RF magnetron sputtering usually have better crystal structure which results in enhanced mobility. However, vacuum deposition methods are expensive and have low throughput. Solution processing on the other hand offers a cheap and easy method of depositing ZnO films with high throughput.[137] In the next part, we will review some of the basics of the sol-gel method along with some of the available works in the literature.

2.1   Sol-gel deposition of ZnO thin films

As mentioned before, ZnO thin films can be deposited using different methods like Molecular Beam Epitaxy (MBE)[138], pulsed laser deposition (PLD)[73], metal-organic chemical vapor deposition (MOCVD)[139], sputtering[14], spray pyrolysis[54], and electrodeposition.[140] Among these methods sol-gel method offers a cheap and easy method with a high throughput.[137] In this method (which is also called soft chemistry), a solid material is also formed from a solution by using a sol or a gel as an intermediate step. This process can be done at temperatures much lower compared to the other methods.[141] The formation of solid oxides from molecular solutions often requires hydrolysis and condensation reactions.[142]

The synthesis of metal oxides by dissolving metal alkoxides in organic solvents is one group of sol-gel methods. This method is based on the polycondensation of metal alkoxides M(OR)z. R is usually an alkyl group and z is the oxidation level of the metal.

The synthesis involves two steps: The first step is hydrolysis in which reactive M-OH groups are formed by the following reaction:

$$M\text{—}OR + H_2O \Rightarrow M\text{—}OH + ROH \tag{2-1}$$

The second step is the condensation, which forms bridging oxygen:

$$M\text{—}OH + RO\text{—}M \Rightarrow M\text{—}O\text{—}M + ROH \tag{2-2}$$

Or

$$M\text{—}OH + HO\text{—}M \Rightarrow M\text{—}O\text{—}M + H_2O \tag{2-3}$$
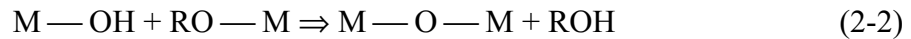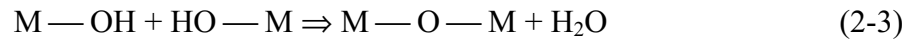
Transition metal alkoxides offer the advantage of good glass wetting. Additionally mixing several alkoxide in one solvent can result in a multicomponent film. However, metal alkoxides are costly and highly reactive. Thus aqueous solutions are more appropriate for industry.[142]

Inorganic precursors in aqueous solutions are another sol-gel deposition method for metal oxides. Once dissolved in an aqueous solution metal cations form compounds with water molecules (M-OH$_2^)$. The formation of M-OH$_2$ bonds draws electrons away from bonding σ molecular orbital of the water molecule. As a result of the electron transfer the O-H bonds gets weaker and the coordinated water molecules act as stronger acids than solvent molecule waters. Olation is one mechanism of condensation, which results in the departure of one molecule of water.

$$\text{—}M\text{—}OH + H_2O\text{—}M\text{—} \Rightarrow \text{—}M\text{—}OH\text{—}M + H_2O \tag{2-4}$$
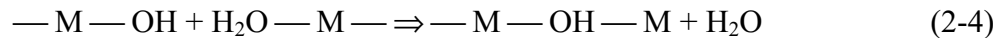
Oxolation is another condensation method in which two OH groups form one water molecule, which is then removed.

$$\text{—}M\text{—}OH + HO\text{—}M\text{—} \Rightarrow \text{—}M\text{—}O\text{—}M\text{—} + H_2O \tag{2-5}$$

38
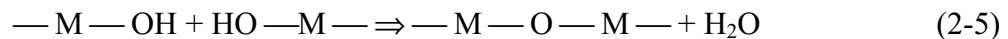
Hence condensation forms oxides or hydroxides.[142]

The sol gel method is a chemical method in which the molecular precursor undergoes the following steps for the formation of oxide films: a) hydrolysis of the precursor b) polymerization by addition of ions forming oxo, hydroxyl, or aqua bridges c) condensation of dehydration d) nucleation e) growth.[143] The deposition of ZnO thin films by sol-gel method involves three steps: 1- preparing the solution 2- depositing the prepared solution on the substrate with different techniques like spin coating 3- heat treatment for drying and pyrolysis of the deposited films. This process can be affected by numerous parameters including precursor and its concentration, the solvent used and its acidity, the stabilizer and its concentration, the method of coating and the speed of it, the type of substrate, the age of the mixture, and the heat treatment of materials are some of the important parameters affecting the formation of ZnO films.[141]

To conclude, in this section we reviewed some of the reactions, which form the metal oxide compounds. Two reactions were discussed: 1- metal alkoxides in organic solvents 2- metal salts in the aqueous solutions. In spite of metal alkoxides advantages such as glass wettability and formation of multicomponent oxides by mixing, expensiveness and high reactivity are two drawbacks of this sol-gel method. Another sol-gel method is mixing of metal salts (organic-inorganic) in the aqueous solution. In the next section we will discuss the details of this approach. The effect of different deposition parameters mentioned above will also be discussed.

2.1.1 **Precursors**

Nitrate, chloride, perchlorate, alkoxide, and acetate dihydrate are some of the common precursors used in ZnO deposition. There are various reports studying the effect of precursors in the deposition of ZnO thin films.[144,145,146,147] Zinc nitrate is the most widely used inorganic salt used for the deposition of zinc oxide. By dissolving zinc nitrate in water, zinc nitrate is ionized as below:

$$Zn(NO_3)_2 + H_2O \Rightarrow Zn^{2+} + 2\ NO_3^- + H_2O \qquad (2\text{-}6)$$

The evaporation of water gives back zinc nitrate. By heating at 450 $^{\circ}$C small crystallites of zinc nitrate are formed.

$$2\ Zn(NO_3)_2 \Rightarrow 2\ ZnO + 4\ NO_2 + O_2 \qquad (2\text{-}7)$$
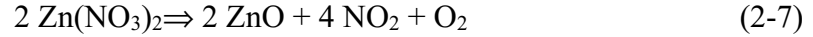
In this reaction small crystallites are formed in random directions very fast, which gives the film dendrite morphology. The crystallite size of films deposited using zinc nitrate was 15 nm in the c-axis and 12 nm in the a-axis direction.

Zinc acetate is the most used organic salt for the ZnO thin film deposition. The process of formation of ZnO from zinc acetate is done in two steps of hydrolysis and condensation. The hydrolysis occurs as follows:

$$Zn(OH)(CH_3COO)_2 + OH^- \Rightarrow Zn(OH)_2 + CH3COO^- \qquad (2\text{-}8)$$
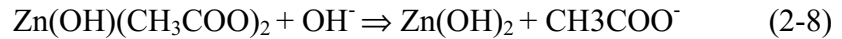
Condensation of two $Zn(OH)_2$ molecules gives:

$$HO\!-\!Zn\!-\!OH + HO\!-\!Zn\!-\!OH \Rightarrow HO\!-\!Zn\!-\!O\!-\!Zn\!-\!OH + H_2O \quad (2\text{-}9)$$

By evaporation of water, the final product has empirical formula of HO-$(Zn\text{-}O\text{-}Zn)_n$–OH where n is the number of molecules involved in the condensation (poly-condensation). Poly-condensation occurs uniformly in all directions in the plane of the substrate. This results in a flat and uniform ZnO film. The crystallite size in the a-axis direction is 25 nm and in the c-axis 15-20 nm.

Comparing the films deposited using zinc nitrate and acetate, it can be concluded that in the zinc nitrate case first crystallization occurs in forms of small crystals of zinc nitrate. Next by heating at 450 $^{\circ}$C, decomposition occurs forming ZnO. For the zinc acetate case hydrolysis, condensation, poly-condensation are the steps prior to the formation of ZnO films at 450 $^{\circ}$C. Hence ZnO films deposited using zinc acetate are uniform.[144] Another drawback of using these inorganic salts is difficulty in removing the anionic species in

the final product.[148] The precursor used also affects the crystal orientation of the deposited films. Figure 2-1 shows the effect of the precursor on the crystal orientation of the deposited films using spray pyrolysis technique.
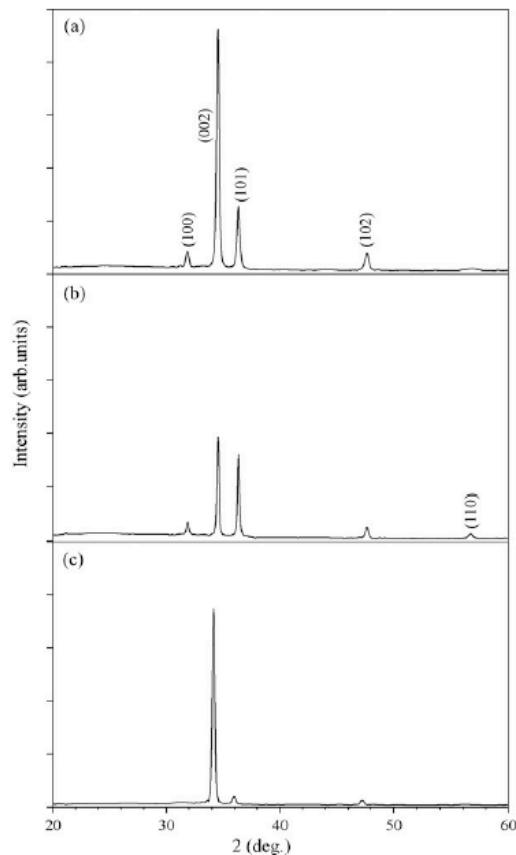
Figure 2-1 XRD patterns of films deposited for a) zinc nitrate b) zinc acetate c) zinc chloride precursors.[147]
(Adapted with permission from Ref[147]; Copyright Elsevier.)

The XRD results reveal that in all cases the (002) orientation is the dominant orientation. The (002) peak is much more dominant in the case of zinc chloride case. As can be seen from figure 2-1(b), the relative intensity of the (002) peak reduces compared to other cases. The relative intensity of the (002) peak in the case of zinc nitrate increases.[147] The different crystallinity for different precursors could be attributed to different growth rates for various precursors.[149] Figure 2-2 shows the SEM images of films deposited with various precursors.

41
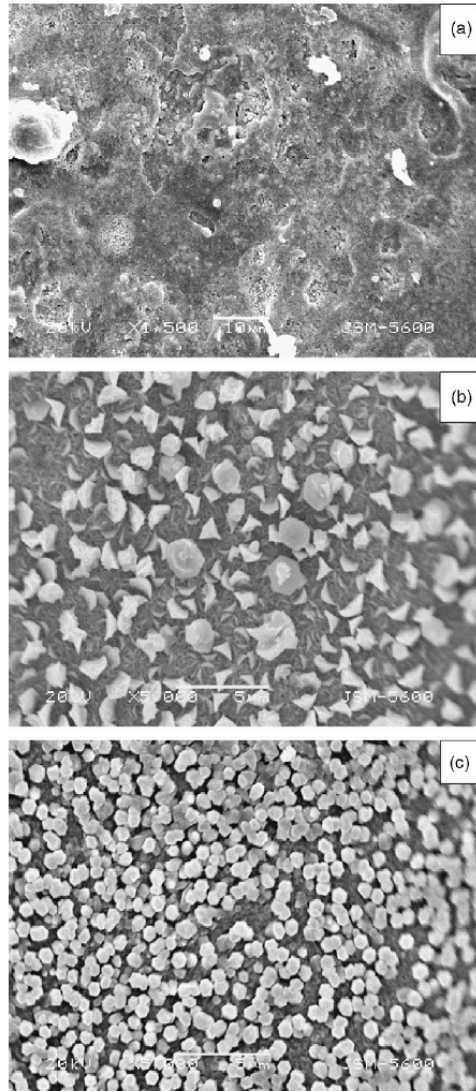
Figure 2-2 SEM images deposited using a) zinc nitrate b) zinc acetate c) zinc chloride. (Adapted with permission from Ref[147]; Copyright Elsevier.)

Figure 2-2(a) shows the films deposited using zinc nitrate. As explained above the film is nonuniform. In the case of zinc acetate hexagonal crystal islands form a flat film similar to the spin coating case. The SEM image of the films grown with zinc chloride shows hexagonal columnar rods along (002) direction. The differences in morphology could be attributed to the availability of enough energy for thermal decomposition at the substrate surface. The initial condition of the substrate also affects the growth process. Stronger interaction between particle-particle results in continuous films whereas in the cases in which there is strong interaction between particle and substrate the films are discontinuous. Using the van der Pauw technique 5.7×10^3, 7.1×10^3, and 1.3×10^4 Ω cm

were measured for zinc nitrate, zinc acetate, and zinc chloride, respectively. The doping concentration was 1.1×10^{14}, 1×10^{14}, and 9.3×10^{13} cm^{-3} for the precursors, respectively.[147] To summarize, in this part we investigated the formation of ZnO thin films using metal salts in aqueous solutions. In the case of inorganic metal salts such as zinc nitrate crystallization occurs by formation of zinc nitrate crystals and decomposition of these crystals by heating where as for organic metal salts hydrolysis, condensation, and poly condensation are steps prior to the formation of ZnO films. The precursor used also affects the morphology of the deposited films, which is related to the energy required for thermal decomposition at the surface of the substrate. Initial condition of the substrate also affects the film structure. In the case of strong particle-particle interactions the films are continuous where as for the case of strong substrate-particle interaction the film becomes dissentious.

2.1.2 Solvents

It is generally well known that solvents with higher dielectric constant facilitate the dissolution of inorganic salts.[143,150,151] It is well known that the dielectric constant is dependent on chain length.[152] Among the various solvents, alcohols with low number of carbon atoms (maximum four) are the most widely used solvents.[141] Methanol[54], ethanol[153], 1-propanol[154], 2-propanol[155], 1-butanol[156], and 2-methoxyethanol[1] are some of the solvents used more compared to the others.

As for the inorganic salts, a lower dielectric constant of the solvent is equivalent to the lower solubility of the salt in the solvent, which results in a shorter induction period for nucleation and higher solid particle growth kinetics. Hu studied the formation of monodispersed hydrous zirconia microspheres with zirconyl chloride dissolved in alcohol-water mixtures.[143] Different solvent like methanol, ethanol, isopropyl alcohol, n-propanol, and acetone were chosen to study the homogenous nucleation and growth. The effect of solvents is related to their dielectric constants. The general trend observed is that solvents with lower dielectric constant caused faster precipitation kinetics. In the case of acetone and n-propanol which have almost similar dielectric constant, reactive interaction of n-propanol with zirconium species results in faster growth kinetics.[143]

As for organic salts, Hosono studied the formation of ZnO nanocrystals from alcoholic solutions of zinc acetate dehydrate at low temperature of 60 $^{\circ}$C.[150] Methanol (dielectric constant of 32.6), ethanol (dielectric constant of 24.3), and 2-methoxyethanol (dielectric constant 16.9) were the solvents used. The important difference in these solvents is their dielectric constant. Zinc acetate shows higher solubility in methanol (higher dielectric constant). Water was added to the solvents to increase the dielectric constant and hence contribute to the dissolving of zinc acetate. In dissolving zinc acetate in methanol solution, each zinc ion is surrounded by six methanol molecules. However, in the case of ethanol and 2-methoxyethanol water molecules also participate in surrounding zinc ions. In all cases the (+2) zinc ions forms ion pair with (-1) acetate ions. Hence a complex is formed containing hydroxyl and acetate groups. The complexes go through hydrolysis, polymerization, and crystallization in to layered hydroxide zinc acetate (LHZA). The formation of acetate rich LHZA in lower dielectric constant solutions is attributed to the stronger coulomb forces. Hydrolysis of LHZA is slowed down by low dielectric constant increasing the formation time of ZnO in ethanol and 2-methoxyethanol.[150] Some other works in the literature also confirm the formation of LHZA complex in the formation of ZnO.[157,158,159] However, Tokumoto reports the formation of zinc-oxy-acetate from dissolving zinc acetate in ethanol.[160]

In spite of the different reported by-products in the intermediate step, both of these reactions undergo hydrolysis and inorganic polymerization leading to the formation of ZnO sols.[141] The influence of solvent can be seen in the nucleation process of zinc acetate with basic solutions like sodium hydroxide. For longer chain alcohols the nucleation is faster compared to the shorter length chain alcohols which is expected for lower dielectric constant solvents.[152]

The solvents also affect the texture of the deposited films. Wang showed that by increasing the ethanol content in aqueous- ethanolic solution the crystal orientation is changed from perpendicular to almost parallel relative to the surface of substrate.[161] Figure 2-3 shows the SEM images of the ZnO films deposited with solvents using different ethanol contents. Oriented nanorods with diameter of 150 nm are seen for the

aqueous solution in figure 2-3(a). Increasing the ethanol content results in a slight increase in diameter of nanorods and tilt of crystals. Increasing the ethanol content increases the amount of tilting causing the films to be more dense. As can be seen from figure 2-3(d) at ethanol content of 40% the cracked hexagonal are still visible. Increasing the ethanol content results in crystal corners (figure 2-3(e)) and smoothed corners (figure 2-3(f)). Increasing the ethanol content generates crystals with irregular shapes (figure 2-3 (g),(h)). This behavior is confirmed by XRD results shown in figure 2-4. As can be seen from the XRD results by increasing the ethanol content the strongest peak is changed from (002) to (101) and ultimately to (001).[161]
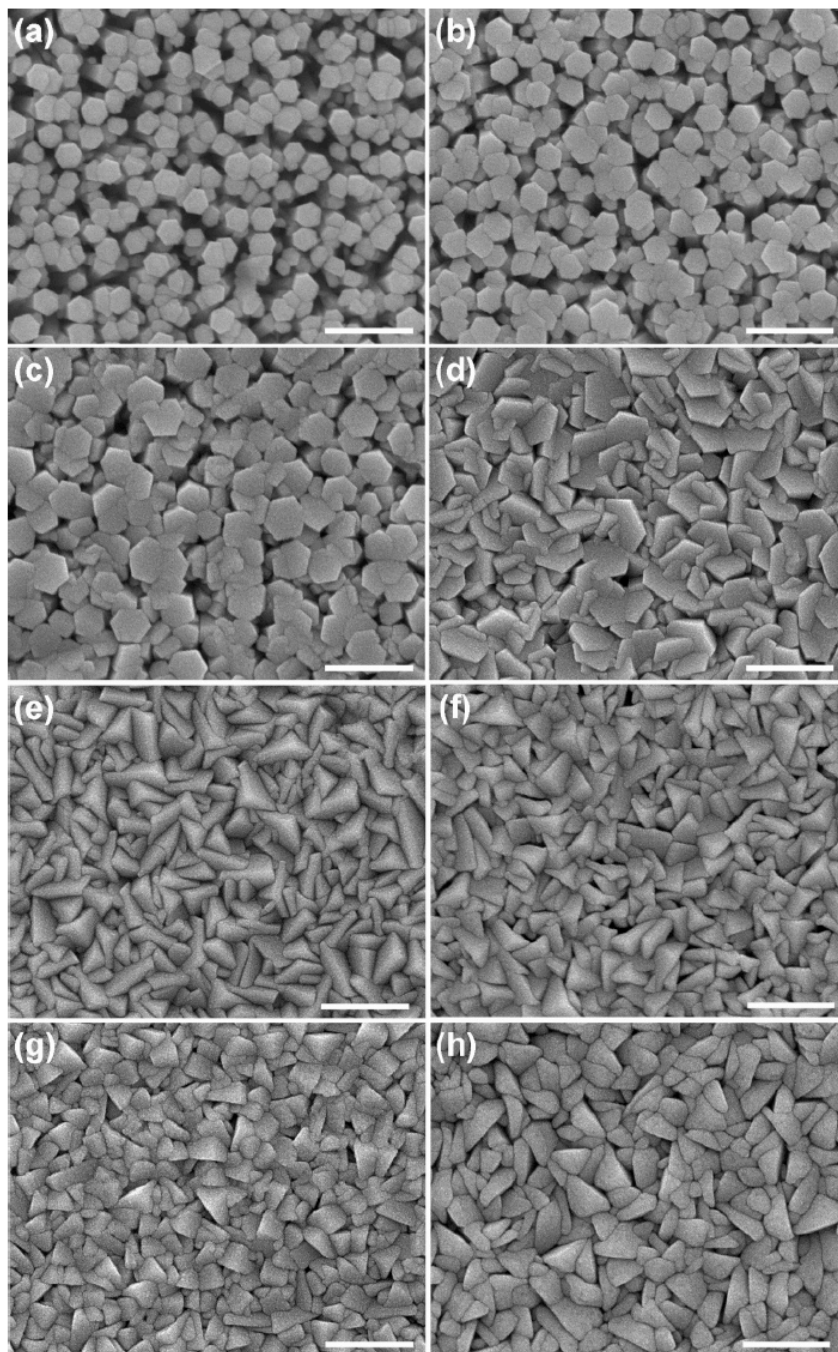
Figure 2-3 SEM images of ZnO films deposited with different ethanol content a) 0% b) 20% c) 30% d) 40% e) 50% f) 60% g) 70% h) 80%. (Adapted with permission from Ref[161]; Copyright American Chemical Society.)
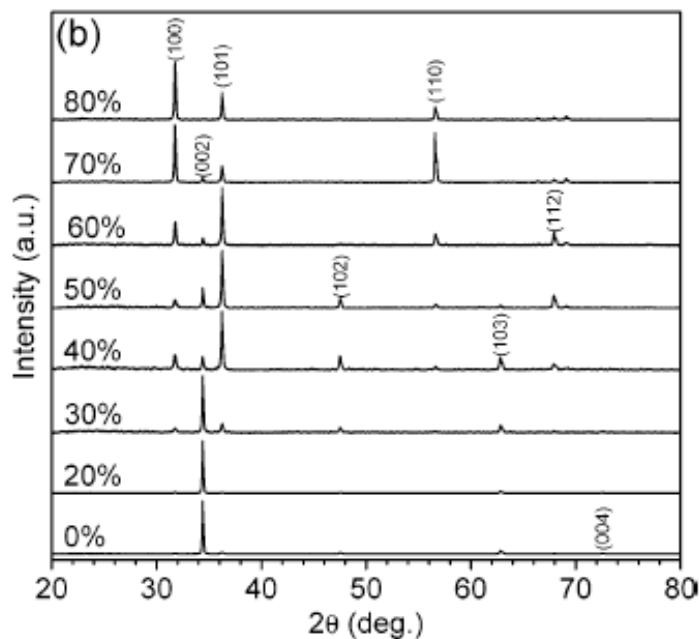
Figure 2-4 XRD results of ZnO films deposited with different content of ethanol in solution. (Adapted with permission from Ref[161]; Copyright American Chemical Society.)

In addition to the dielectric constant of the solvent, the boiling point of the solvent also has a huge impact on the crystallinity of the films. Higher boiling point slows down the evaporation of the solvent resulting in a larger grain-sized films.

To summarize in this part we studied the reactions that led to the formation of ZnO thin films with emphasis on the effect of solvent. In these reactions a layered zinc acetate hydroxide (LHZA) was formed. In the case of low dielectric constant solvents a more acetate rich LHZA was formed. The solvents also affect the crystal texture of the deposited films.

2.1.3 Stabilizers

Stabilizers are chemical species containing at least one functional group. Alkali metal hydroxide, carboxylic acid, alkanolamines, alkylamines, acetylacetone, and polyalcohols are some of the stabilizers used for depositing ZnO nanostructures.[141] There are several reasons for their usage: in some cases they contribute to the dissolving of zinc salt in the alcoholic solvents. It is well known that zinc acetate dehydrate does not dissolve completely in alcohols like ethanol or 2-propanol. By addition of stabilizers like

monoethanolamine or triethanolamine this issue is resolved.[155] Another role of stabilizers is stabilizing ligands, preventing the rapid precipitation of zinc hydroxide and hence contributing to the formation of stable sols.[141] For instance by adding alkanolamine to zinc acetate solution, a clear solution is obtained.[162]

Amines like monoethanolamine and diethanolamine are one of the common stabilizers used in ZnO sol-gel deposition. In the sol-gel method hydrolysis starts the reactions leading to the formation of sols. Hence basic or aqueous solutions are required. Aqueous solutions are used for quantum dot production and are not suitable for depositing thin films. Basic solutions are made by adding inorganic bases like NaOH and LiOH to the solution. These inorganic bases cause precipitation, prevent film formation and contamination.

Amines can be used as a stabilizer for ZnO thin film deposition. Basic nature, showing stabilizing behavior, and contributing to the dissolving of precursors and film formation are some of the features that make amines suitable candidates for stabilizers in ZnO film depositions. These stabilizers reduce the contamination of ZnO films and have less health risks and enviormental hazards.[163] Vajargah studied the effect of amine stabilizers on the ZnO thin films deposited on glass substrates.[163] Monoethanolamine, diethanolamine, triethanolamine, triethylamine, and ethylenediamine are the studied stabilizers. Amines were added to 1-propanol solvent under stirring. In the next step zinc acetate was added to the solution to obtain a 0.2 mol L^{-1} solution. The ratio of Zn(+2)/stabilizer was selected as 0.5, 1, and 2. The films were deposited using dip coating with the withdrawal speed of 120 mm min^{-1} with 10 min drying period at 120 ^{o}C or 300 ^{o}C between each coating. Finally the films were annealed at 500 ^{o}C. Figure 2-5 shows the XRD results of the deposited films.
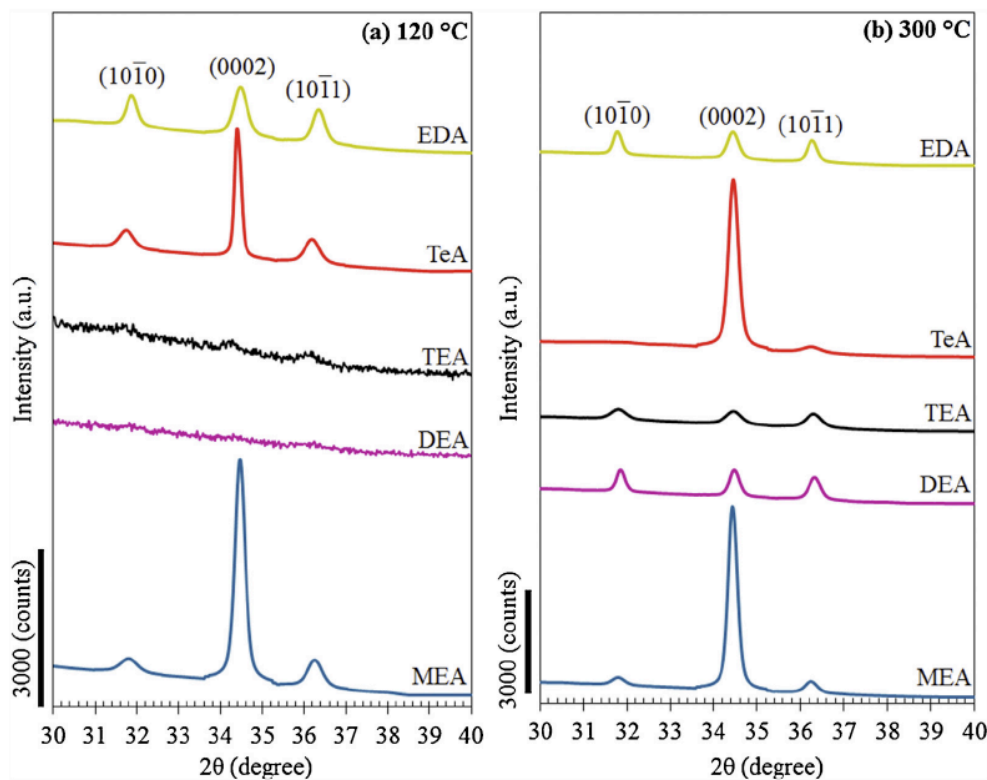
Figure 2-5 XRD patterns of different thin films deposited using drying temperature of a) 120 °C b) 300 °C for 10 min. (Adapted with permission from Ref[163]; Copyright Elsevier.)

As can be seen from figure 2-5, monoethanolamine stabilizer produces ZnO thin films with (0002) orientation, which is perpendicular to the substrate. A non-crystal structure is observed for diethanolamine and triethanolamine. The films deposited using triethylamine also show (0002) orientation. The films deposited using ethylenediamine show random orientation.[163]

Explanation of the behavior results for different stabilizers is related to both sol and heat treatment parameters. Generally reducing the overlap of a) evaporation b) decomposing of organic material c) crystallization during annealing enhances the crystallinity of the thin films. The non-crystallinity of diethanolamine (boiling point of 280 °C) and triethanolamine (boiling point of 335 °C) is due to the large difference between the drying temperature (120 °C) and boiling point of the sols. As can be seen by increasing the drying temperature to 300 °C both films obtain crystallinity. Thus the high boiling point

and slow condensation prevents the formation of crystals in the diethanolamine and triethanolamine. Low boiling point of (89 $^{\circ}$C) and formation of large amounts of zinc-oxy-acetate are some of the reasons contributing to the preferred crystallinity of triethylamine. Ethylenediamine is a polar base with relatively low boiling point. The random orientation of ethylenediamine could be due to the chelating agent of the stabilizer preventing the formation of complexes with tetrahedral shape.[163]

Ohyama studied the effect of temperature and stabilizer on the crystallinity of the ZnO films.[162] The films were deposited using dip coating on glass substrates. Zinc acetate was dissolved in 2-methoxyethanol using monoethanolamine and diethanolamine. The solution was kept at 60 $^{\circ}$C under stirring for 30 min before deposition. The molar ratio of zinc acetate to alkanolamine was 1. The withdrawal speed of 3.5 cm min^{-1} was used in the dip coating process followed by heat treatment at temperatures in the range of 200 $^{\circ}$C to 800 $^{\circ}$C. This process was repeated twice followed by the heat treatment at the same temperature for one hour. XRD results are shown in figure 2-6. As can be seen from figure 2-6(a) by increasing the temperature for diethanolamine films, no preferred orientation is obtained and all the three peaks of (002), (101), and (100) are observed. In the monoethanolamine case, the crystallization of ZnO starts at around 200 $^{\circ}$C. The (002) peak, which is the only observed peak, intensifies at 500 $^{\circ}$C. Increasing the temperature from 500 $^{\circ}$C weakens the (002) peak and other peaks appear as well. The high boiling point of monoethanolamine and 2-methoxyethanol and lack of overlap between the evaporation and decomposing of organic material (unlike the diethanolamine case) is the reason for high crystallinity of the films deposited using monoethanolamine and 2-methoxyethanol.[162]

Image removed due to lack of copyright permission.

Figure 2-6 XRD results for ZnO fims deposited at different temperatures using a) diethanolamine b) ethanolamine stabilizers.[162]

To conclude, stabilizers are chemical species containing at least one functional group, which are used for their contribution to the dissolving of salts and forming of stable sols. The stabilizers affect the crystallinity by varying the overlap between evaporation,

decomposition of organic material, and crystallization (during annealing) based on their boiling temperature.

As mentioned before the deposited ZnO films are affected by different parameters like the precursor, the solvent, the stabilizer, the age of the solution, the speed and method of coating, substrate type and the heat treatment method. In the next part we will discuss the effect of each of these parameters on the deposited ZnO films.

2.2 Film Deposition:

Spin coating and dip coating are the two main methods for depositing ZnO films. The sols can be fresh or aged at room temperature or around 60 $^{\circ}$C. As for the heat treatment, a two-step procedure is preferred. In the first step (pre-heat treatment) the solvent and organic compound are removed at temperatures in the range of 40-500 $^{\circ}$C. The main purpose of the post-heat treatment is obtaining better crystallinity for the films along with the decomposition of organic by-products. The post heat treatment temperature can vary between 250 to 900 $^{\circ}$C based on the substrates used.[141]

2.3 Chemical System:

As previously mentioned, deposition of ZnO thin films using solution processing method depends on parameters like the precursor type and concentration, stabilizer, solvent, age of solution, speed and method of coating, substrate type and heat treatment method. The influence of precursor, stabilizer, and the solvent used was discussed in the last section.

The precursor concentration is also another parameter affecting the crystallinity of the ZnO. However, the results related to the effect of precursor concentration are contradictory. The differences in crystallinity could be due to differences in experimental conditions. Kim studied the effect of precursor concentration on the crystallinity of ZnO films.[164] In this experiment zinc acetate was dissolved in mixture of isopropanol-monoethanolamine with the ratio of zinc acetate to monoethanolamine kept at 1. The concentration of zinc acetate varied from 0.3 to 1.3 mol L^{-1}. The solution was stirred at 50 $^{\circ}$C for one hour. The solution was spin coated on glass substrate at 3000 rpm for 20 s. Preheating and postheating temperatures of 250 $^{\circ}$C and 650 $^{\circ}$C were used, respectively. Figure 2-7 shows the XRD results for different precursor concentrations.
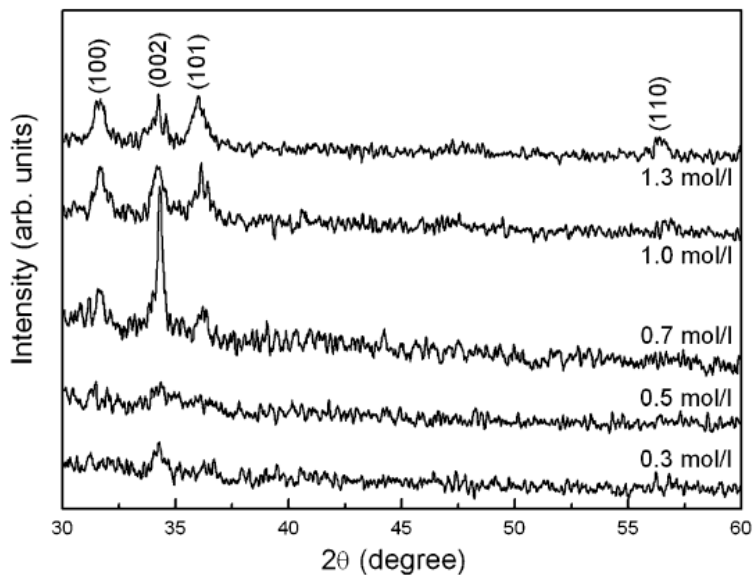
Figure 2-7 XRD results for different precursor concentrations dried at 250 °C and annealed at 650 °C. (Adapted with permission from Ref[164]; Copyright Elsevier.)

As can be seen from figure 2-7, the 0.7 mol L^{-1} concentration results in highly (002) peak orientation with small (100) and (101) peaks. Increasing the solution concentration reduces the (002) peak and increases (100) and (101) peaks.[164] O Brien got different results as shown in figure 2-8.[165]
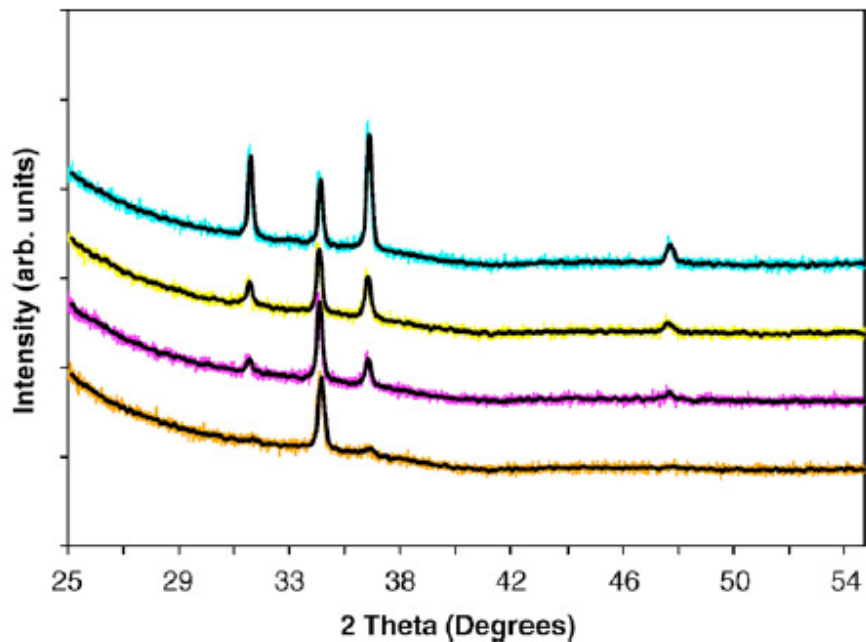
Figure 2-8 XRD results for different precursor concentration of ZnO films spin coated at 2000 rpm, dried at 60 °C and annealed at 650 °C. (Adapted with permission from Ref[165]; Copyright Elsevier.)

As can be seen from figure 2-8, the film with precursor concentration of 0.3 M resulted in the highest (002) orientation. By increasing the concentration to 0.7 M, the (002) concentration lost dominance. Increasing the precursor concentration to 1.3 M resulted in the (101) peak to become dominant.[165]

The differences in the result could be due to differences in experimental conditions: in Kim's experiment a drying temperature of 250 °C and spin coating of 300 °C were used where as in O Brien's experiment the drying temperature was 60 °C and spin coating speed of 2000 rpm was used.[141] In the preheating temperature of 60 °C the drying step and decomposition of organics do not overlap where as in the 250 °C drying step the organic materials are decomposed in the drying step as well. In addition to the solution concentration, the order of using different concentrations also affects the crystallinity of the films.

Li studied the effect of solution concentration and the order of deposition on the ZnO films.[135] In order to do so, ZnO TFTs were fabricated with 0.05 M, 0.1 M, 0.25 M, and

0.5 M solution concentrations at annealing temperature of 500 ^{o}C. By using the low concentration solutions and performing the deposition multiple times, high mobility is obtained. However, in the first deposition cycles the mobility is low due to the discontinuous nature of the film. For instance, for the solution of concentration of 0.05 M, by repeating the deposition ten times, the highest amount of mobility of 6.78 cm^2 V^{-1}s^{-1} is obtained. For the precursor solution of 0.1 M, by repeating the deposition five times, the highest mobility of 2.86 cm^2 V^{-1}s^{-1} is achieved. As for the 0.25 M solution, one deposition cycle resulted in the mobility of 2.18 cm^{2}V^{-1}s^{-1}. Increasing the number of deposition cycles did not enhance the mobility. For the solution concentration of 0.5 M, with one deposition cycle, saturation mobility of 0.64 cm^2 V^{-1}s^{-1} is obtained. Increasing the deposition steps reduces the mobility. In order to make the deposition of high quality films cost efficient, it is required that the lowest number of deposition cycles result in the highest mobility. Hence, three solution concentrations of 0.05 M, 0.1 M, and 0.25 M were chosen to reduce the number of deposition cycles. Figure 2-9 compares the obtained mobility by changing the order of the concentration of each deposition cycle.
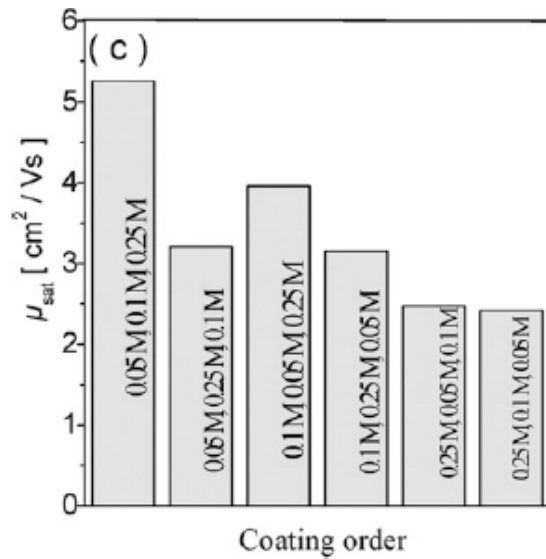
Figure 2-9 Saturation mobility of ZnO TFT devices using three deposition cycles with different orders. (Adapted with permission from Ref[135]; Copyright Royal Society of Chemistry.)

As can be seen from figure 2-9, the 0.05 M, 0.1 M, and 0.25 M precursor concentration order results in the highest mobility of 5.26 cm^{2}V^{-1}s^{-1}. As mentioned before, at low concentration of precursors, the films were not continuous, resulting in low mobility for

the films. By increasing the number of deposition cycles the film became dense, covering the whole substrate hence improving the mobility. However, this method needed many deposition cycles, which increased the costs. ZnO films prepared using high concentration solutions fully cover the substrate. However, the films were very dense creating micropores. The processes of vaporization, decomposition, and crystallization introduce even more micropores to the films. Increasing the number of deposition cycles introduced even more pores further degrading the mobility. Hence, it can be concluded that to obtain the maximum mobility, the deposition should be done in a multistep way starting from lower concentration ending with the highest concentration. Due to the low concentration of the first deposition step, the film will be discontinuous. By performing the subsequent deposition steps, the gaps will be filled resulting in continuous films. By eliminating one of the steps in the deposition, the devices show an unstable behavior in long runs. Eliminating each of the deposition steps reduces the density of the prepared crystal films resulting in a higher resistance, which in turn causes the devices to heat up. This heat increases the rate of erosion of electrodes.[135]

In addition to the precursor concentration, the aging time of the sol can also affect the competition of the two (100) and (002) orientations. Li studied the effect of aging sol on the orientation of the ZnO deposited films.[166] Zinc acetate, monoethanolamine, and ethanol were used as the precursor, stabilizer, and solvent, respectively. The solution with concentration of 0.25 mol L^{-1} was stirred at 70 ^{o}C for 1 hr. These sols were aged 0 (sample A), 8 hr (sample B), 24 hr (sample C), and 36 hr (sample D). Drying, pre-annealing, and post-annealing temperatures of 100 ^{o}C, 320 ^{o}C, and 500 ^{o}C were used, respectively. The XRD results are shown in figure 2-10. As can be seen from the figure, all the films show c-axis orientation and the (002) peak intensifies with aging.[166] This result agrees with some reports in the literature.[167] The intensification of (002) peak is attributed to the condensation of the active groups and aggregation of zinc species in the solution resulting in the (002) peak intensification.[167]

To conclude, the effect of different parameters like precursor concentration, order of deposition for different concentrations, and aging of the sol was studied on the

crystallinity of the film. As for the precursor concentration contradictory results are available in the literature due to different deposition parameters. As for the order of deposition of different concentration solutions, the optimum results are obtained by using the lower concentrations for the first deposition cycles to obtain the seed layers followed by higher concentration depositions to make the film continuous. Older solutions also result in more intensified (002) peaks which is attributed to the condensation of the active groups and aggregation of zinc species.
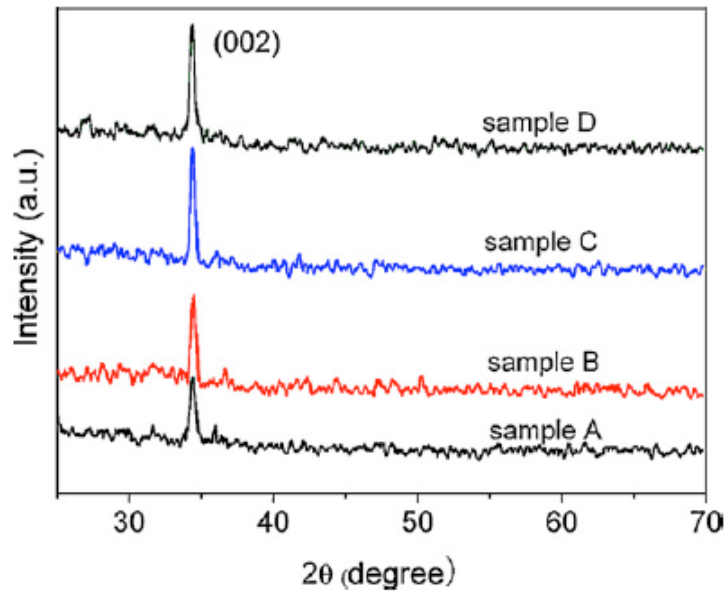
Figure 2-10 XRD results for aged solutions of a) 0 hr (sample A) b) 8 hr (sample B) c) 24 hr (sample C) d) 36 hr (sample D). (Adapted with permission from Ref[166]; Copyright Elsevier.)

2.3.1 **Coating method, speed, thickness, substrate:**

(a)   (b)
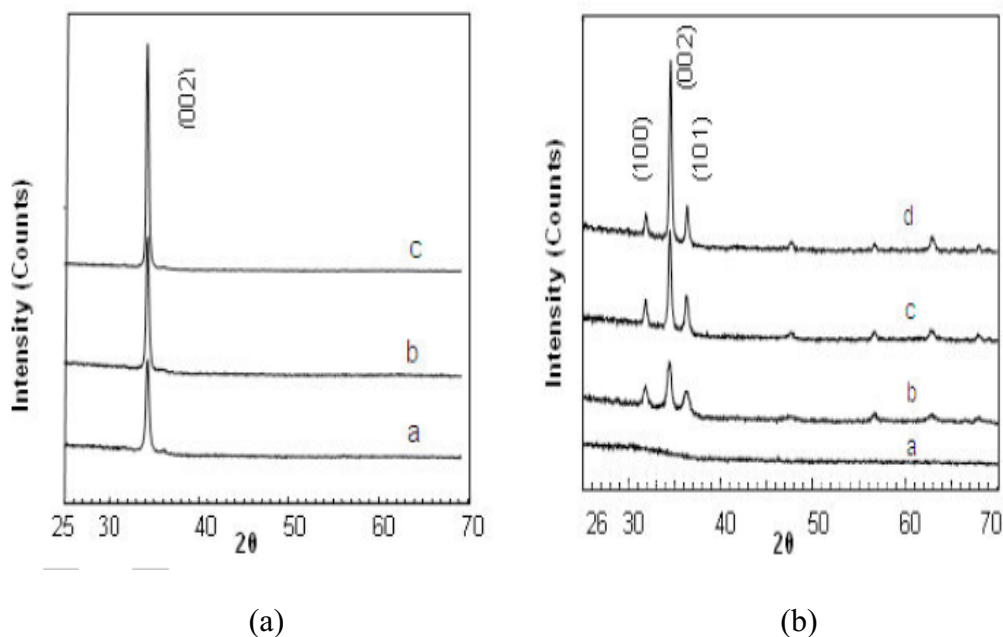
Figure 2-11 XRD results for a) Dip coating b) Spin coating. Sample a,b,c annealed at 350 °C, 450 °C, and 550 °C, respectively. (Adapted with permission from Ref[168]; Copyright Springer.)

Dip coating and spin coating are the main methods used in solution processing. Habibi investigated the effect of coating method on the crystal structure of the ZnO films.[168] Both of the films were deposited using zinc acetate dihydrate as the precursor, isopropanol as the solvent, and monoethanolamine as the stabilizer. Figure 2-11 shows the XRD results for the dip coating and spin coating. As can be seen from figure 2-11 increasing the temperature from 350 °C to 550 °C intensifies the (002) peak. Thin films deposited using dip coating were deposited with the withdrawal speed of 1cm min^{-1}. These films were highly *c*-axis orientated. On the other hand, films deposited using spin coating (3000 rpm) exhibited three XRD peaks with the (002) peak being the stronger peak.[168] Ohyama investigated the effect of withdrawal speed on film characteristics of dip coated films.[84] The results are shown in figure 2-12 for various withdrawal speeds.
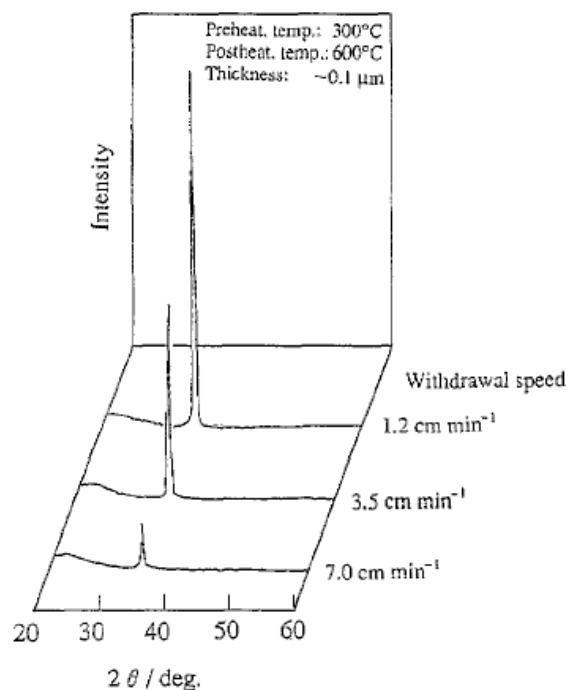
Figure 2-12 XRD results for withdrawal speed of 1.2 cm min^{-1} (five times repetition) 3.5 cm min^{-1} (three time repetition) 7 cm min^{-1} (two time repetition). (Adapted with permission from Ref[84]; Copyright Elsevier.)

The number of repetitions was chosen so that for each withdrawal speed a film thickness of 100 nm is obtained. As is apparent in figure 2-12, by reducing the withdrawal speed the (002) peak intensity increases. At low withdrawal speed films are thinner and the solvent can easily evaporate from the film contributing to the deposition of dense films. The higher (002) peak for smaller withdrawal speed could be explained in two ways: 1- Due to higher density of films more unidirectional film growth is obtained resulting in higher (002) peak. 2- the organic substances and solvent can evaporate more easily from thinner films without changing the crystal structure.[84]

The thickness of the film also influences the crystallinity and electrical properties of ZnO thin films. Mridha studied the effect of film thickness on the crystallinity and electrical properties of thin films.[169] Zinc acetate dihydrate, diethanolamine, and isopropyl alcohol were the used precursor, stabilizer, and solvent, respectively. The solution with concentration of 0.1 mol L^{-1} was spin coated at 2500 rpm for 20 s. Drying and annealing temperatures of 120 $^{\circ}$C and 550 $^{\circ}$C were used, respectively. Figure 2-13(a) shows the XRD results for various thicknesses.
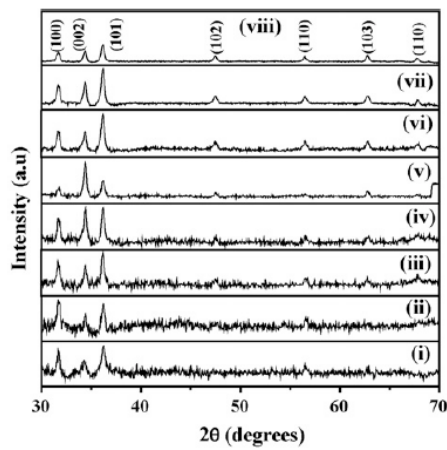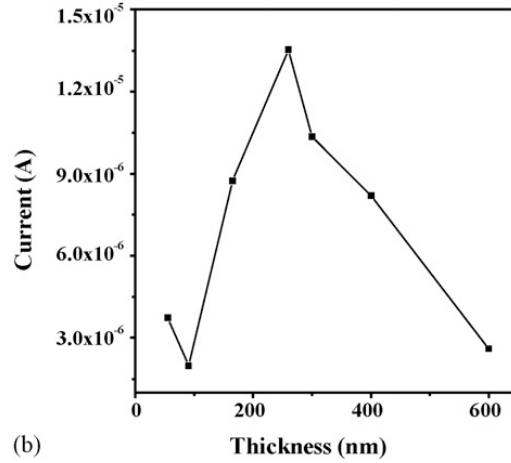
Figure 2-13 a) XRD results for i) 55 nm ii) 90 nm iii) 165 nm iv) 180 nm v) 260 nm vi) 300 nm vii) 400 nm viii) 600 nm thick ZnO films. b) Variation of current with thickness of ZnO films. (Adapted with permission from Ref[169]; Copyright Pergamon.)

As is apparent in figure 2-13, by increasing the film thickness to 260 nm the (002) peak becomes the dominant peak. However, above this thickness the film becomes randomly oriented. This behavior is attributed to the *c*-axis strain of the ZnO crystals. By measuring the strain of the films with thickness, it is observed that films are relaxed and strain is reduced by thickness growth. By increasing the film thickness to 400-600 nm range, strain increases again. The electrical resistivity also increases with film thickness from 27 Ω cm (for thickness of 55 nm) to 256 Ω cm (for thickness of 400 nm). Figure 2-13 (b) shows the variation of current with thickness of the films. This result is surprising since based on the resistivity values, the current is expected to decrease and then increase. This behavior is attributed to the adsorbed oxygen at the surface of the ZnO films. At first by increasing the film thickness the film is more porous which causes more oxygen molecules to get adsorbed to the surface. The adsorbed oxygen molecules trap carriers and as a result the resistivity (current) increases (decreases).[169]

The results reported by Ohyama for dip coating technique are however different.[170] Exhibiting (002) peak even on amorphous glass substrates, it is expected that the (002) peak intensity increases proportionally. However, this was not observed for film thickness below 100 nm. Additionally the peak intensity is very weak for the first dip

59

coating. This is attributed to the effect of amorphous glass substrate on the growth of the film. By deposition of the first layer, this slightly oriented layer improves the orientation of the subsequent layer. Hence a sudden increase in the peak value is observed.[84]

The substrate also affects the crystallinity of the deposited ZnO films. Chakrabarti investigated the effect of substrate on the film crystallinity.[155] Zinc acetate (precursor), diethanolamine (stabilizer), and propanol (solvent) were mixed with the molar ratio of 1:0.006:55, respectively.[155] ZnO films were deposited using dip coating method. The chosen substrates were: soda-lime glass, quartz glass, Corning 7059 glass, p-type Si (100), and polycrystalline alumina. Drying temperature of 100 ^{o}C was used for all films. Annealing temperatures of 500 ^{o}C, 550 ^{o}C, 600 ^{o}C, and 700 ^{o}C were used for different cases. Figure 2-14 (a) shows XRD results for ZnO films deposited on soda-lime glass and annealed at 550 ^{o}C. Films deposited on soda lime glass were annealed at two temperatures of 500 ^{o}C and 550 ^{o}C. The film annealed at 500 ^{o}C showed two equal peaks for (002) and (101) where as for the films annealed at 550 ^{o}C highly c-axis oriented films were obtained. Figure 2-14 (b) is the XRD result for ZnO deposited on quartz annealed at 700 oC. The two peaks of (002) and (101) are observed in this case. For annealing temperatures of 500 ^{o}C and 550 ^{o}C all three peaks are observed. Increasing the temperature intensifies the (002) peak. Figure 2-14 (c) is the XRD result for corning glass annealed at 700 ^{o}C. As for the corning glass, increasing the temperature increased the (002) peak intensity. Hence at 700 ^{o}C the (002) peak orientation was maximum. As for the p-type Si (100), for the annealing temperatures of 500 ^{o}C and 550 ^{o}C all the three peaks were observed. Increasing the temperature to 600 ^{o}C and 700 ^{o}C resulted in the disappearance of (100). For all the annealing temperatures, the (002) peak was the dominant peak. For the Al_2O_3 poly crystalline film all the three peaks are observed for all annealing temperatures.[155]
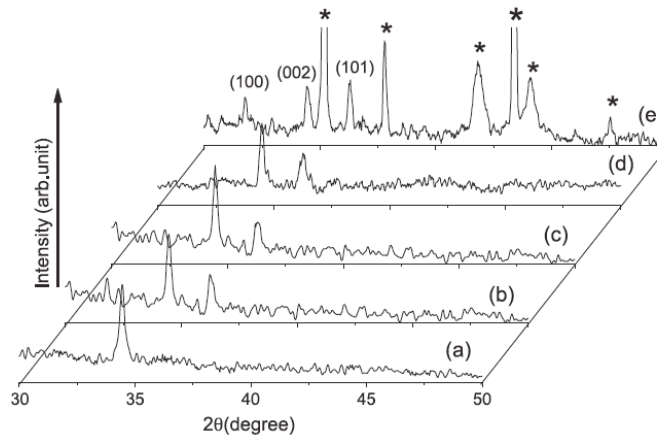
Figure 2-14 XRD results for ZnO films deposited on different substrates with different annealing temperatures a) Soda lime glass at 550 °C. b) Quartz glass substrate 700 °C. c) Corning glass annealed 700 °C. d) ZnO on p-type Si (100) substrate annealed at 700 °C. e) ZnO on polycrystalline alumina glass annealed at 700 °C. (Adapted with permission from Ref[155]; Copyright Elsevier.)

Hence it can be concluded that among all the substrates, soda lime glass slides resulted in the highest orientation with minimum annealing temperature. Corning glass and quartz substrates ranked the second and third for highest orientation. The dense structure of quartz glass did not lead to preferential orientation of (002). Polycrystalline alumina showed the most random orientation, which can be explained by the differences in wide order range. The Si (100) substrate also shows less orientation compared to amorphous substrates.[155]

In this section we compared the crystallinity of the films deposited by dip coating and spin coating methods. It is observed that films deposited using dip coating method are highly *c*-axis oriented compared to the spin coated films. The film thickness shows different effect on the crystallinity of the deposited films using spin coating and dip coating method. As for the role of the substrate, generally amorphous substrates result in higher c-axis orientation compared to other crystalline and poly crystalline substrates.

2.3.2 **Pre-heat and post-heat treatment:**

Heat treatment is another factor affecting the orientation of the films. As mentioned above the pre- and post-heating is consisted of three steps: 1- evaporation 2- decomposition of organic residue 3- crystallization. If any of these steps is not complete before the start of the next step, the crystal growth will be disrupted.

Kim studied the effect of preheating on the structural properties of ZnO thin films.[164] Zinc acetate was dissolved in isopropanol with monoethanolamine as the stabilizer. The solution was stirred at 50 °C for 1 hr. The obtained transparent solution was spin coated at 3000 rpm for 20 s. Preheating temperatures of 200 °C, 225 °C, 250 °C, 275 °C, and 300 °C were chosen for 10 min preheating followed by annealing at 650 °C for 1 hr. Figure 2-15 shows the XRD results of different pre-heating temperatures.
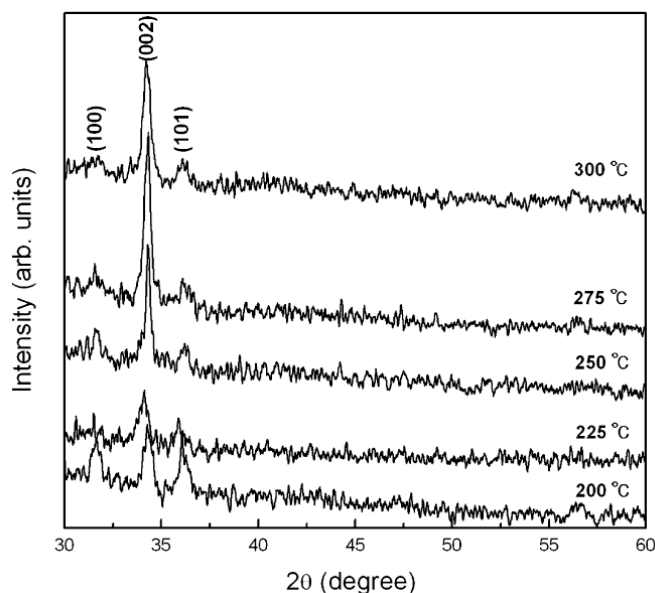
Figure 2-15 XRD results for different pre-heating temperatures. (Adapted with permission from Ref[164]; Copyright Elsevier.)

As can be seen from figure 2-15, at 200 °C and 225 °C pre-heating temperatures, all the three (100), (002), and (101) peaks are observed with similar intensities. Increasing the temperature to 250 °C, causes the (002) peak to become the dominant peak. At 275 °C, the maximum peak value for (002) is observed where as the (100) and (101) peaks are almost vanished. However, increasing the temperature to 300 °C, reduces the (002) orientation. The thermal decomposition of zinc acetate occurs as 240 °C.[84] The boiling point of monoethanolamine, and isopropanol are 170, and 82.4 °C, respectively. By increasing the pre-heating temperature to 300 °C, the vaporization of solvent and stabilizer, decomposition of zinc acetate, and crystallization will occur simultaneously disrupting the preferred orientation growth of the crystal. Using low pre-heating temperatures (like 200 °C), the vaporization of solvents and decomposition of zinc acetate is not complete at the preheating step and is postponed to post-heating step.

Similar to the previous case, the vaporization of solvent and decomposition of acetate occur at the crystallization phase hindering the growth of the preferred orientation.[164] The pre-heat treatment is the most important factor in affecting the crystal orientation. Hence, it can be concluded that removal of solvent and organic substances produced by acetate decomposition before crystallization is an important factor in oriented crystal growth. [141] Wang also studied the effect pre-heating and annealing on the crystal structure of the films.[171] Zinc acetate was dissolved in isopropanol and stirred. When the solution turned milky, diethanolamine and some amount of water was added and the mix was stirred at 60 ^{o}C for 30 min. The molar ratio of zinc acetate to diethanolamine was 1:1. The solution concentration was 0.32 mol L^{-1}. The solution was spin coated on Si-SiO$_2$-Ti-Pt substrates at 3000 rpm for 30 s. The pre-heating was performed at temperatures in the range of 300-450 ^{o}C for 10 min. Subsequently, the films were annealed at temperatures in the range of 550-800 ^{o}C for 30 min.
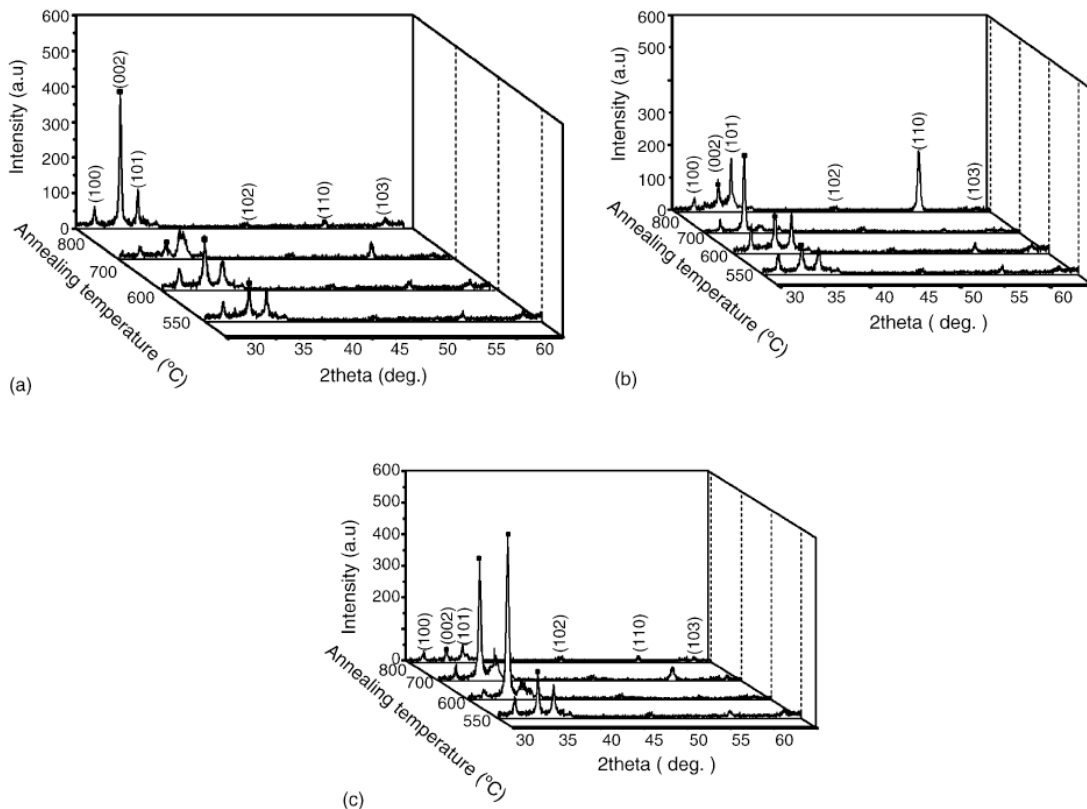
Figure 2-16 XRD results for different preheating and annealing temperatures a) Preheated at 300 ^{o}C b) Preheated at 400 ^{o}C c) Preheated at 450 ^{o}C. (Adapted with permission from Ref[171]; Copyright Elsevier.)

Figure 2-16 (a) shows the XRD results for films pre-heated at 300 ^{o}C. As can be seen from figure 2-16 (a), ZnO films annealed at 550, 600, and 700 ^{o}C have random orientation. However, at annealing temperature of 800 ^{o}C the preferred orientation of (002) is observed. As for pre-heated samples at 400 ^{o}C, the preferred orientation was only obtained at 700 ^{o}C. Increasing the temperature to 800 ^{o}C reduces the crystal orientation. For samples pre-heated at 450 ^{o}C, films annealed at 600 ^{o}C show maximum preferred orientation. Increasing the temperature to 700 ^{o}C, the crystallinity reduces and at 800 ^{o}C random orientation is observed. As for the films pre-heated at 450 ^{o}C, at 500 ^{o}C random orientation is observed. The maximum (002) orientation is obtained for 600 ^{o}C annealing temperature and increasing the temperature beyond that will reduce the crystal orientation.

Hence it can be concluded that for films preheated at the same temperature, there is an optimum temperature in which the maximum (002) orientation is obtained. However, increasing the temperature from that optimum temperature will result in reduction of crystallinity of the films. The preferred orientation (002) is obtained at lower annealing temperatures for samples pre-heated at higher temperatures.[171] Hence it can be concluded that an upper limit exists above which the orientation is lost.

In order to obtain the optimum pre and post-heating temperatures, Ong used thermogravimetric analysis during the deposition of ZnO films. Figure 2-17 shows the thermogravimetric analysis for zinc acetate dehydrate. This analysis proved that $Zn(OAc)_2$ starts decomposing at 190 ^{o}C and the decomposition is complete at 300 ^{o}C. As can be seen from figure 2-17, an exothermic peak is observed in the range of 300-400 ^{o}C. Another small exothermic peak is observed between 400-500 ^{o}C, which is the proof of the continuation of crystallization. In the temperatures above 500 ^{o}C, no heat flow change or weight loss is measured. Hence, it can be concluded that the temperature range of 400-500 ^{o}C is the optimum temperature range for annealing ZnO thin films. Heating profile also has a profound impact on the crystallization of ZnO thin films. As can be seen from the XRD pattern, in the case where the annealing temperature is increased from room temperature to 500 ^{o}C (at the rate of 10 ^{o}C min^{-1}), the crystal orientation is random,

exhibiting three peaks at 31.8°, 34.4°, and 36.6° corresponding to (100), (002), and (101), respectively. On the other hand, if the samples are directly annealed at 500 °C only the (002) peak is observed which indicates crystalline ZnO thin film with the preferred orientation is deposited.[137]
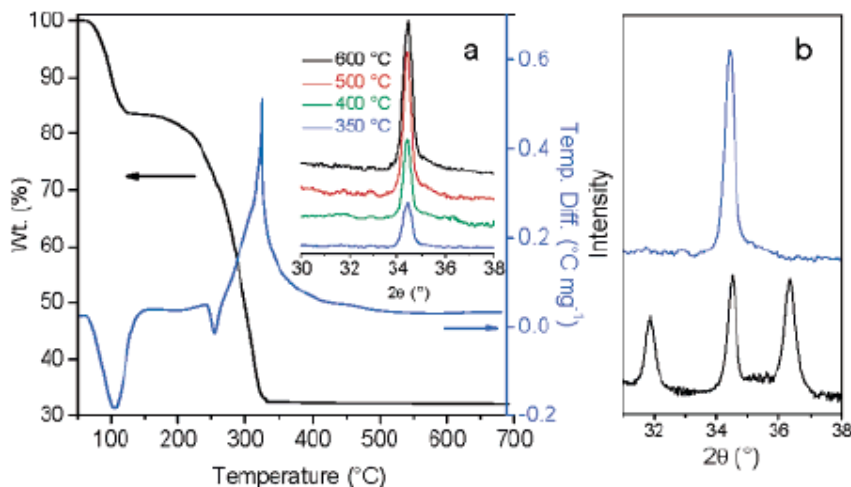
Figure 2-17 a) Thermogravimetric analysis and differential thermal analysis of zinc acetate at the rate of 10 °C min⁻¹. (inset) increase in the (002) peak by increasing the temperature to 500 °C and remaining constant afterwards. b) Comparison of XRD patterns. (Adapted with permission from Ref[137]; Copyright Royal Society of Chemistry)

Hence it can be concluded that the optimum temperature for pre-heat treatment and post-heat treatment using ZAD precursor, monoethanolamine stabilizer, and 2-methoxyethanol solvent is 180 °C and 500 °C, respectively.[137]

In this section we discussed the effect of preheating and annealing temperature on the crystallinity of ZnO films. It is important to choose the preheating temperature in a way that solvent and organic substances produced by acetate decomposition are removed prior to crystallization. As for annealing temperature, for films deposited at a particular preheating temperature an optimum annealing temperature exists in which beyond the *c*-axis orientation is lost. For higher preheating temperatures, the optimum annealing temperature will be lower.

2.4 Summary

In this chapter we discussed some of the parameters affecting the growth and orientation of the solution processed ZnO films. Precursor and its concentration, solvent, stabilizer, coating method, speed of deposition, thickness of the film, substrate, and the chosen temperatures for pre-heating and post-heating are some of the parameters affecting the crystallinity of the ZnO films. The effect of variation of each of the parameters on the crystallinity of the ZnO films was investigated with detail. Among all the different parameters, the pre-heating and post-heating temperatures are the most important parameters affecting the growth of the films. Removal of stabilizer and solvent and other organic species prior to the start of crystallization is an important factor in obtaining desired crystallization. Thermogravemetric analysis was done to measure the optimum pre-heating and post-heating temperatures. The thermogravemetric analysis shows that in the case of zinc acetate precursor, ethanolamine stabilizer, and 2-methoxyethanol solvent the decomposition starts at 190 $^\text{o}$C and is completed at 310 $^\text{o}$C. Separating the drying and annealing steps improves the crystal structure of films. Hence for the case of the above recipe the drying and annealing were preformed at 180 $^\text{o}$C and 500 $^\text{o}$C, respectively.

3   ZnO UV Photodetectors

Recently there has been growing interest in utilizing ZnO for various applications. ZnO is an attractive material with interesting features. ZnO is a wide bandgap semiconductor made from earth abundant material. ZnO has a large exciton binding energy of (60 meV) at room temperature which makes lasing at room temperature feasible.[172],[173],[174],[175] The high break down field and saturation velocity makes ZnO a potential alternative for power devices. Resistance against radiation[176], easy wet chemical etching, and transparency are other useful features of ZnO material. However, difficulty in producing reliable and reproducible p-type ZnO has hindered the wider usage of ZnO.

There is a considerable overlap between ZnO and GaN. In addition to difficulty in p-type production of ZnO, lower mobility, stronger electron-phonon coupling, and lower thermal conductivity are some of the disadvantages of ZnO compared to GaN. The GaN technology is much more mature compared to ZnO. However, ZnO has its own potential applications. Transparent thin film transistor (TTFT) is one of the potential applications of ZnO.[12,13, 177] Scarcity of indium and growing need for indium tin oxide (ITO) is another motivation for wider usage of transparent oxide semiconductors.[99,100,97] Higher exciton binding energy at room temperature for ZnO (60 meV) compared to GaN (25 meV) gives ZnO an edge for excitonic laser applications.[149] ZnO also exhibits large electromechanical coupling (specially in the c direction). This characteristic is utilized in acoustic wave devices.[178,179] Ease of growth for ZnO nanostructures is another important advantage of ZnO. ZnO nanowires are widely used for fabrication of devices like thin film transistors[180],[181], Schottky diodes[182,183], and photodetectors.[184] LEDs[185,186] , solar cells[187,188] and gas sensors[189] are some of the other applications of ZnO.[190]

In this chapter, we will review some of the important works related to ZnO UV MSM photodetectors. Simple structure, Ease of fabrication and integration, and low capacitance per unit area are some of the advantages of MSM photodetectors. MSM photodetectors are two back to back Schottky diodes and interdigitated electrodes are used as Schottky contacts on top of active light collection region. Figure 3-1 shows the structure of the MSM devices.
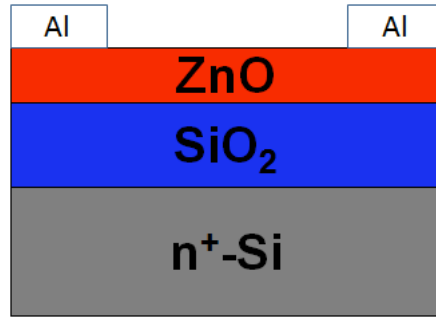
Figure 3-1 Structure of MSM photodetector.

Due to low capacitance per unit area, these devices are fast. The limiting factor in these devices is transit time which by using e-beam lithography and adjusting the distance and width of the electrodes can be minimized. The biggest drawback of these devices is their low responsivity which is due to the blocking of incoming light by the electrodes.[191]

3.1 Vacuum Deposition of ZnO UV photodetectors

Different vacuum deposition methods have been used for the fabrication of ZnO UV detectors. RF magnetron sputtering[192], metal organic chemical vapor deposition (MOCVD)[193], and pulsed laser deposition (PLD) are some of the utilized deposition methods.[194]

Jiang fabricated Schottky type ZnO MSM phot detectors using RF sputtering.[195] The distance between a zinc target and SiO2 substrate was 6 cm. Subsequent to reducing the chamber pressure to 3×10^{-4} Pa, Ar and O_2 gasses were added to the chamber through mass flow controllers with rates of 60 and 20 SCCM (standard cubic centimeter per minute), respectively. The working pressure was kept at 1 Pa and RF power used and substrate temperature were 150 W and 400 $^{\circ}$C, respectively. Au contacts were evaporated at a pressure of 1×10^{-3} Pa. The electrodes had an interdigitated structure with 5 μm width, 500 μm length, and pitch of 2 μm. Figure 3-2 (a) shows the current values under dark and 365 nm illumination. The dark current is 1 nA at 3 V bias. This low dark current is attributed to the high Schottky barrier heights. The maximum responsivity of the device was 0.337 A W^{-1} (at 3 V bias for 2 μm) pitch. The rise and fall time of the ZnO UV photodetector (for 10-90% of peak) 20 ns and 250 ns, respectively. The fall time did not

show a big change for 10um, 5um, and 2um pitches. So the fall time is attributed to the holes being trapped at the ZnO film surface.[195]

(a)   (b)
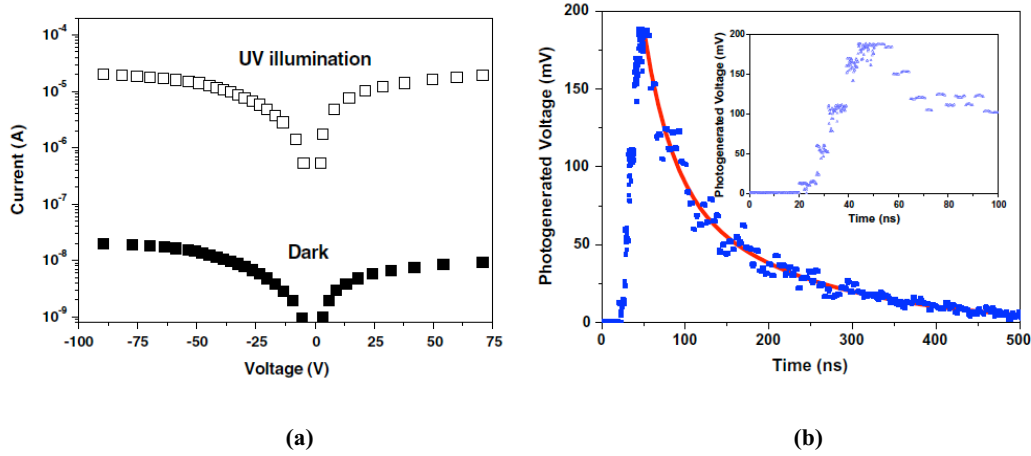
Figure 3-2 a) I-V characteristics of ZnO MSM photodetectors in dark and 365 nm illumination. b) Response time of ZnO UV detector with pitch of 2 um. (Adapted with permission from Ref[195]; Copyright Pergamon.)

Liang fabricated Schottky ZnO UV detectors using MOCVD ZnO films grown on sapphire substrates.[193] The metal-semiconductor-metal (MSM) photodetectors were fabricated using Ag as Schottky and Al as ohmic contacts. The structure of MSM photodetector was circular and interdigital (IDT). In the circular structure, the outer diameter, inner diameter, and gap were 320 μm, 150 μm, and 10 μm, respectively. The Ag-ZnO-Al devices were studied to investigate the properties of Schottky contact. The Ag-ZnO-Ag structures were used for MSM photodetectors. To understand the effect of Schottky contacts, Al-ZnO-Al structures were also fabricated for MSM photodetectors. The Al-ZnO-Al structures exhibit a linear behavior where as the Ag-ZnO-Al structures show a rectifying behavior. This confirms the Schottky behavior of Ag contacts on ZnO. The UV photodetector performance was evaluated the Ag-ZnO-Ag structures. Figure 3-3 (a) shows the dark and UV illuminated I-V characteristics of these devices.
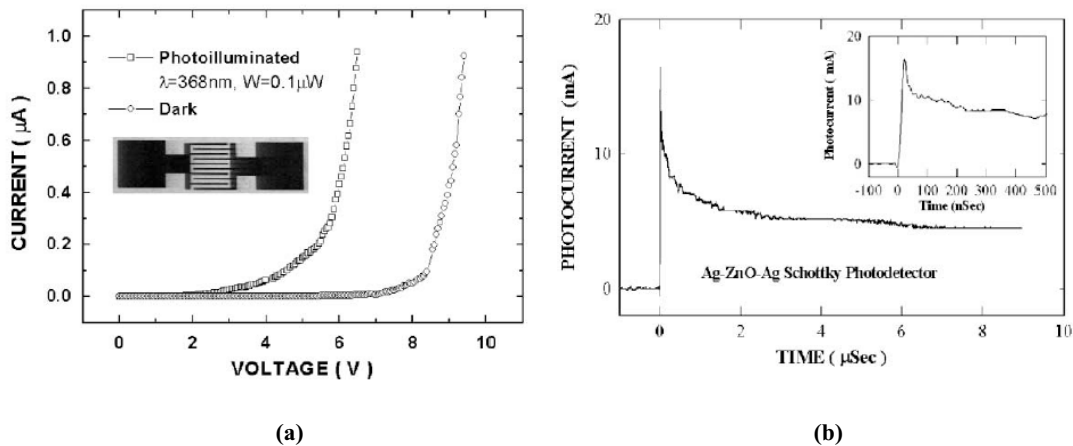
Figure 3-3 a) I-V characteristics of a ZnO Schottky photodetector with an IDT structure. b) photocurrent vs response time of ZnO Schottky photoconductor. (Adapted with permission from Ref[193]; Copyright Elsevier.)

The wavelength and power of the illumination light were 368 nm and 0.1 μW, respectively. The leakage current for 5 V bias was approximately 1 nA. The breakdown starts at 8 V in the dark. The low frequency responsivity was about 1.5 AW^{-1} (corresponding to the gain of 2.5). Figure 3-3 (b) shows the photoresponse of the Schottky MSM photodetector. The photoresponse has a fast component with rise time of 12 ns and fall time of 50 ns. In addition to this fast fall time, a slow fall time is also observed (for 5 ms). The fast response in a ZnO MSM detector is attributed to the transit time of the photo-generated carriers while the slow response is due to adsorption of oxygen to the surface of ZnO.[193]

Lin also fabricated ZnO MSM photodetectors using MBE deposition methods.[196] ZnO epitaxial films were grown on sapphire substrates using molecular beam deposition (MBE). Ruthenium (Ru) was used as the Schottky contact on ZnO which showed a Schottky barrier height of 0.76 eV at ZnO/Ru interface. Figure 3-4 (a) shows the I-V characteristics of the ZnO MSM photodetectors with Ru contacts. At 1 V bias, the measured dark and photocurrent (with a 150 W deuterium lamp (D_2)) values were 8×10^{-8} and 1.8×10^{-5} A, respectively. Hence the photo to dark current ratio of 225 was achieved. This ratio can be improved by annealing the devices in an oxygen-containing environment. In this way the Ru electrode converts to RuO_2, which is highly transparent, electrically conductive, and has a high work function (>5 eV). Additionally, RuO_2 forms

Schottky contacts with high barriers hence suppressing the dark current. Transparency of RuO_2 contacts on the other hand will increase the photocurrent. Hence the photo to dark current ratio will improve. Figure 3-4 (b) shows the decay of photocurrent following removal of the D2 lamp. A third order exponential fit was used to fit the curve. In this way, a time constant of 13 ms was measured for the decay of the photocurrent.[196]

(a)   (b)
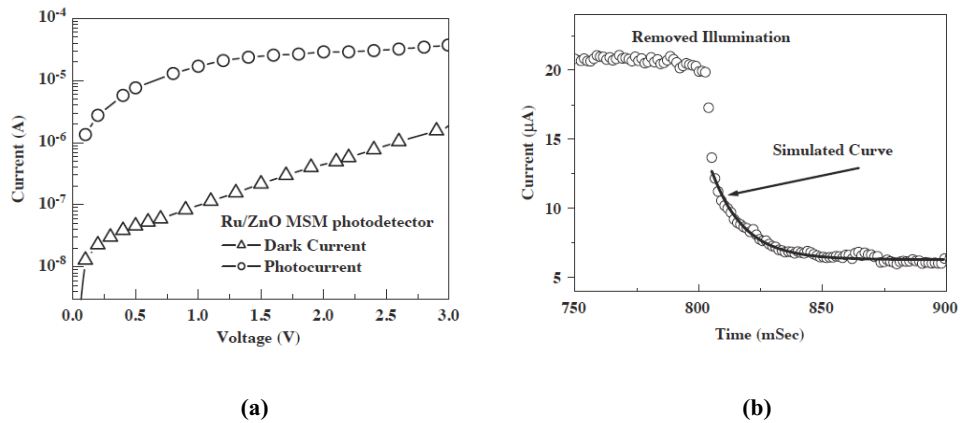
Figure 3-4 I-V characteristics of fabricated ZnO MSM photodetectors with Ru electrodes measured in the dark and under illumination. b) Transient response in the ZnO MSM photodetectors by removal of deuterium lamp. (Adapted with permission from Ref[196]; Copyright Elsevier.)

3.2 Solution Processed ZnO UV Photodetectors

In addition to vacuum deposition methods, ZnO UV photodetectors can also be fabricated using sol-gel method. Basak reported on the photodetectors using sol-gel ZnO thin films.[197] Zinc acetate dehydrate, dimethylamine, and isopropyl alcohol were used as the precursor, stabilizer, and solvent, respectively. Solutions with concentration of 0.6 M were prepared to deposit ZnO films on (0001) sapphire substrates. Drop coating with the withdrawal speed of 6 cm min^{-1} was used for ZnO film deposition. Subsequently the samples were dried at 120 $^{\circ}$C for 20 min and annealed at 550 $^{\circ}$C for 20 min. Several gold electrodes (thickness 30 nm) with diameter of 1 mm and 3 mm spacing are deposited on ZnO films. The Au contact has an ohmic behavior on ZnO thin films. The photocurrent (I_{ph}) value is:

$$I_{ph} = \frac{q\lambda}{hc} GP \tag{3-1}$$

in which P is the incident power and G is the photoconductive gain. Photoconductive gain is defined as the number of electrons detected per incident photon. The responsivity of the photodetector is defined as:

$$R_\lambda = \frac{I_{ph}}{P\lambda} \tag{3-2}$$

The photoconductive gain is written as:

$$G = \frac{\tau}{t_r} \eta \tag{3-3}$$

where η is the quantum efficiency, τ is the excess carrier lifetime, and t_r is the transit time of electrons between two ohmic contacts. The transit time of electrons between two electrodes is calculated as:

$$t_r = \frac{L^2}{\mu_n V} \tag{3-4}$$

where L is the distance of the two contacts, μ_e is the electron mobility, and V is the voltage applied to the contacts. Hence responsivity should exhibit a linear relationship with bias voltage. Figure 3-5 (a) shows the variation of responsivity with bias voltage. As can be seen, the responsivity of the photodetector varies linearly with bias voltage. Figure 3-5 (b) shows the photoresponse of the deposited ZnO films under 5 V bias. As apparent in figure 3-5 (b), it takes 160 s for the signal to reach 50% of its maximum value.[197]
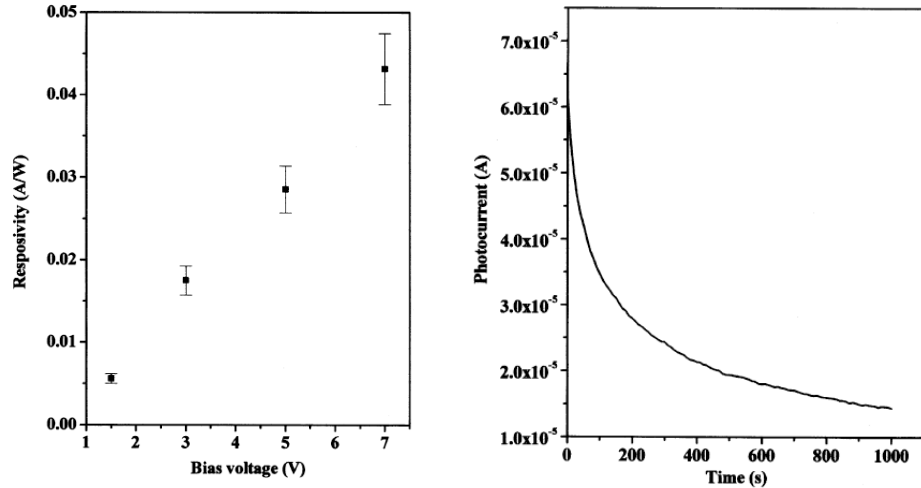
Figure 3-5 a) Variation of responsivity with voltage bias b) photoresponse of ZnO photoconductors. (Adapted with permission from Ref[197]; Copyright Elsevier.)

Jin fabricated MSM ZnO UV photodetectors using colloidal ZnO nanoparticles.[198] Figure 3-6 (a) shows the I-V characteristics of ZnO nanoparticles in the dark and 0.83 mW cm^{-2} UV light illumination. The ZnO nanoparticles show a very high resistance to the dark current, with dark current values smaller than 120 pA. Illumination of the films with power density of 1.06 mW cm^{-2} increases the current values by 6 orders of magnitude. Figure 3-6 (b) shows the dependence of photocurrent to the incident optical power. As can be seen from figure 3-6 (b) increasing the power intensity from 10.3 uW cm^{-2} to 1.06 mW cm^{-2}, increases the current magnitude from 34 nA to 3.1×10^5 nA (4 orders of magnitude increase). The responsivity of the device is 61 A W^{-1} at intensity of 1.06 mW cm^{-2}. Using equations (3-1) and (3-2) photoconductive gain of 203 is calculated. Figure 3-6 (c) shows the response time of the ZnO nanoparticles to the turn-on and turn-off of the UV lamp. In both the turn-on and turn-off case, a rapid response is observed in combination with a slow response. When the lamp is turned on, the device current is increased from 2×10^{-1} nA to 5.5×10^3 nA in 0.1 s followed by a slower response. In the slower response, the current is increased by a factor of 40 in 25 s. As for the decay process, the photocurrent drops by 3 orders of magnitude in the first 9-10 s. Subsequent to this fast response, a slow photoresponse decay follows in which the current reduces by 2-3 orders of magnitude in 2 mins.
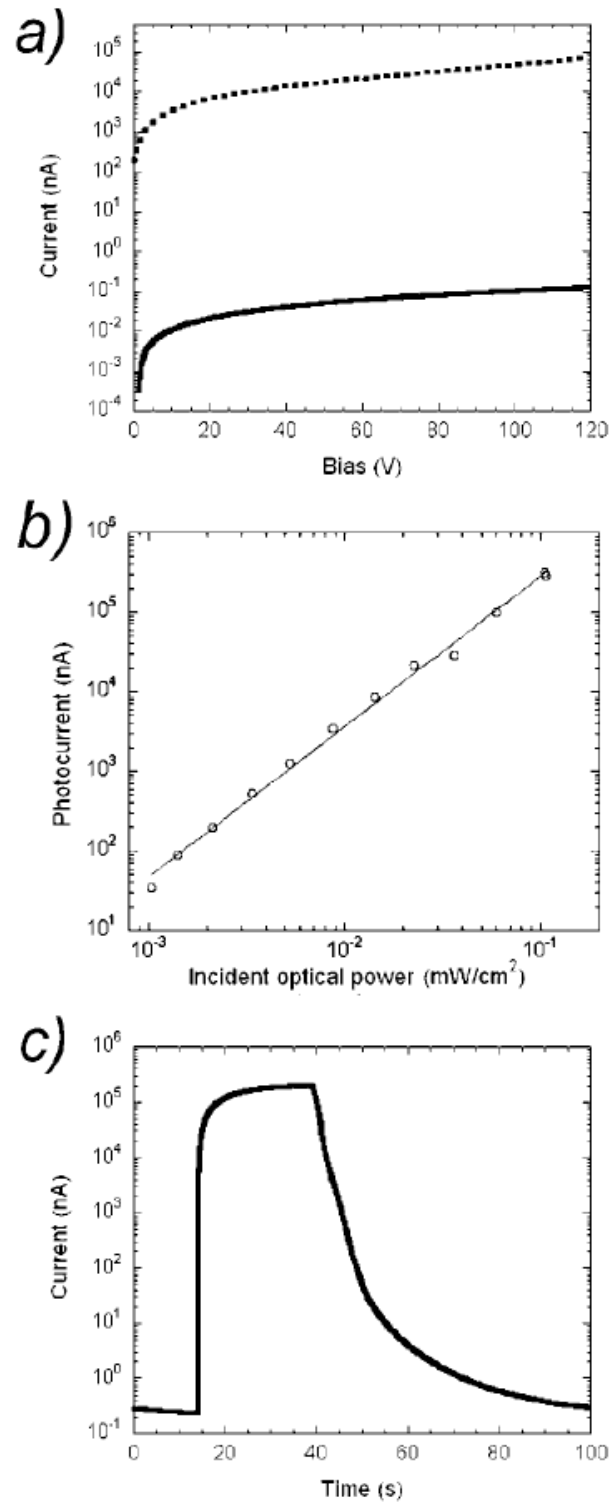
Figure 3-6 a) I-V characteristics in the dark (solid line) and under 0.83 mW cm^{-2} illumination at 370 nm (dashed line) b) Variation of photocurrent with incident power at 370 nm at 120 V bias. c) Photoresponse at 120 V to a 25.5 s light pulse. (Adapted with permission from Ref[198]; Copyright American Chemical Society.)

The high resistivity observed for the dark current case is attributed to adsorbed oxygen at surface of ZnO nanoparticles. These adsorbed oxygen molecules create a low conductivity depletion region, which in the case of nanocrystalline films may extend to the bulk of the film. Upon illumination with photons of higher than bandgap energy and generation of electrons and holes, the holes will move toward the surface due to band bending and discharge the negatively charged adsorbed oxygen ions. Hence the free charge carrier concentration will increase. By desorption of the oxygen from the surface of ZnO films, the depletion layer thickness will reduce, decreasing (increasing) the resistivity (current).[198]

Ahn investigated the effect of atmosphere on the photoresponse of sol-gel ZnO nanowire UV detectors.[199] Aqueous solution of zinc nitrate hexahydrate and methyl amine (ratio 1:1) was prepared. Si-SiO$_2$ substrates were faced downward on the solution in an alumina boat. The solution was heated up to 95 ^{o}C in the furnace for 1-2 hrs. Figure 3-7 shows the I-V characteristics of the ZnO nanowire photodetector. As can be seen from figure 3-7 (a) the I-V relationship is nonlinear. This nonlinearity could be due to the contact barriers of metal electrodes or interfaces of ZnO nanorods. As can be seen from the left inset of figure 3-7 (a), the UV illumination (325 nm) produces photocurrents. Illumination by blue light (450 nm) switches the photocurrent off.
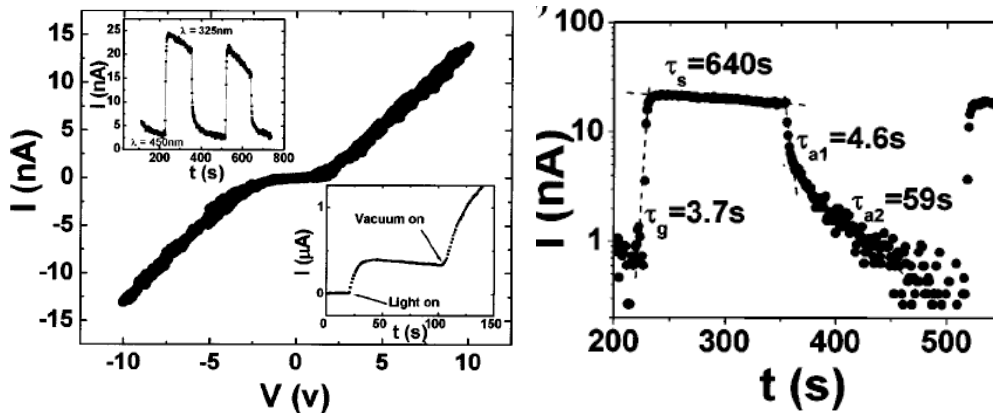
Figure 3-7 a) I-V characteristics of ZnO nanorods. left inset: photocurrent dependent on wavelength of light at 325 nm and 450 nm. Right inset: change of current depending on illumination of light and vacuum states. b)

Exponential behavior of photocurrent. (Adapted with permission from Ref[199]; Copyright American Institute of Physics .)

The right inset of figure 3-7 (a) shows the effect of illumination and vacuum on the conductance of ZnO nanowires. The first increase is due to illumination and second increase is because of vacuum. Figure 3-7 (b) shows the exponential behavior of growing and decaying currents. Current growth had a time constant of τ_g= 3.7 s where as current decay had two time constants of τ_{d1}=4.6 s and τ_{d2}=59 s. The increase of current due to illumination was explained above. However, the change of conductance due to vacuum can not be explained by variation of oxygen pressure since the vacuum can not break the bonds of oxygen with defect sites.[199]

The oxygen vacancies in ZnO are in three states: V_O state which has captured two electrons and is neutral with respect to the lattice, the single ionized state $V_O^{\bullet}$ and the $V_O^{\bullet\bullet}$ which did not trap any electrons and is doubly positively charged. $V_O^{\bullet}$ defect sites are found mostly at the surface of ZnO.[200] Water and oxygen molecules compete to adsorb to the surface defects. The defective sites are more favorable for hydroxyl group adsorption compared to oxygen adsorption.[201]

Water molecules can combine with oxygen vacancies ($V_O^{\bullet}$) hence affecting the conductance of ZnO nanorods. The adsorption process can be done by chemisorption in the form of hydroxyl bonding or physisorption in the form of water molecules. As for the decay time, the high number of oxygen vacancies at the surface increases the water molecule adsorption causing the fast τ_{d1} current delay. As the surface vacancies decrease, the remaining adsorbents should diffuse deeper in the nanorods, which requires thermally activated energy causing the slower decay in the current. Hence the current reduction will be fast at first and with time slows down. As for current generation process, the excitation light will provide enough energy for desorption and diffusion together. Hence the photocurrent generation process will be a fast process.[199] Table 3-1 summarizes some of the results for different MSM photodetectors.

Table 3-1 Summary of some of the ZnO MSM photodetectors in the literature.

Ref	Fabrication Process	Dark Current	Responsivity (A W^{-1})	Response Time
195	RF Sputter	1 nA at 3 V bias	0.337 at 3 V bias	20 ns (rise time) 250 ns (fall time)
193	MOCVD	1 nA at 5 V bias	1.5	12ns (rise time) 50 ns (fast fall time) 5 ms (slow fall time)
196	MBE	8×10^{-8} at 1 V bias	0.337 at 3 V bias	13 ms (fall time)
197	Sol-gel	22×10^{-6} at 5 V bias	0.04	160 (fall time)
198	Sol-gel	120 pA at 120 V bias	61 (1.06 mW cm^{-2})	0.1 s (fast rise time) 25 s (slow rise time) 9-10 s (fast fall time) 2 mins (slow fall time)
202	ALD	100 mA at 2 V bias	0.7 at 370 nm	N/A

3.3 Summary

In this chapter we reviewed some of the MSM photodetectors available in the literature fabricated using various deposition techniques. In all cases the adsorption and desorption of oxygen to the surface of the ZnO has a crucial impact on the photoresponse of the device. Adsorption of oxygen to the surface of ZnO, traps the free charge carrier creating a depletion region at the surface. This depletion region increases the resistivity of the films and causes band bending at the surface. By illuminating the device with UV light, electron-hole pairs are generated. The excited electrons will reach the conduction band while the holes will travel to the surface due to the band bending causing the desorption of oxygen molecules. This will result in a large photocurrent value.

4 Solution Processed ZnO Schottky Barrier Thin Film Transistors

4.1 Introduction

Solution processing is a relatively inexpensive, high-throughput, manufacturing method on large area substrates and is particularly desirable for the fabrication of low cost electronic and optoelectronic devices. ZnO is a wide band-gap semiconductor made from earth-abundant materials which has a combination of promising optoelectronic properties including a large exciton binding energy, high radiation resistance, good electronic mobility, high breakdown field, high saturation velocity and facile solution-based synthesis.[203] These properties render ZnO thin films attractive as active layers in solution processed FETs for use in low-cost electronic displays, radio-frequency identification tags, power inverters, light-emitting devices and transparent electronics.[79, 204] In addition, *n*-ZnO, in conjunction with *p*-type semiconducting thin films of organic small molecules and polymers, can be used to construct circuits that implement complementary logic.[205]

Currently, the two solution-processing methods commonly used to form ZnO thin films are pyrolysis of a coated film of a solution-based ZnO precursor (usually zinc acetate)[170] and the spin-coating of a colloidal dispersion of ZnO nanoparticles, subsequently subjected to sintering.[204b, 205a] In both these methods, it is difficult to control the electrical parameters of the films such as the doping density and defect concentration from run to run, and *p*-type ZnO is not yet reproducibly obtainable.[206] Therefore, better methods to control the electrical characteristics of the FETs incorporating ZnO films are much needed.[207]

The properties of the semiconductor film have a huge impact on the electrical performance of the ZnO TFTs. Hence by reducing the number of defects high performance ZnO TFTs will be obtained.[74]

Another method of improving the TFT performance is by modifying the transistor structure. One method of modifying the transistor structure is through schottky barrier thin film transistor (SB-TFT) or the source gated transistor (SGT).[208,74] The only difference between the SB-TFT with the conventional TFT is that in the SB-TFT the ohmic contact of the conventional TFT is replaced by the schottky source injection barrier.[1] This reduces the off current caused by the back injection of holes at the drain.[209,74] Hence instead of channel conductance, the gate controlled barrier of the schottky source is the main factor in determining the current transport. Higher output impedance, better stability, and lower saturation voltage are the advantages of this architecture.[210,209] The reduction of the drive current is the main drawback of this architecture.[74] In this chapter, we will become familiar with the operating principles of Schottky barrier transistors. Subsequently, the concept of Schottky barrier will be applied to ZnO thin film transistors. This is the first Schottky barrier transistor fabricated for solution processed ZnO active layer thin films.

4.2 Schottky Barrier Transistors

The structure of source-gated transistor is shown in figure 4-1. The main idea behind this type of transistor is controlling the current by changing the barrier height at the source. Hence a source barrier is used to constrict the flow of carriers and the field effect is used to change the barrier height and hence the current value. Unlike the conventional FET where the saturation occurs by depletion of the channel at the drain, in the source-gated transistors the depletion occurs at the source end of the channel. By increasing the drain voltage, the region between the source and the gate is depleted of free charge. Hence the source current becomes independent of the drain voltage and is determined only by the gate voltage. Schottky contacts, MIS barriers, and space charge limited currents are some of the ways of producing a barrier at the source.
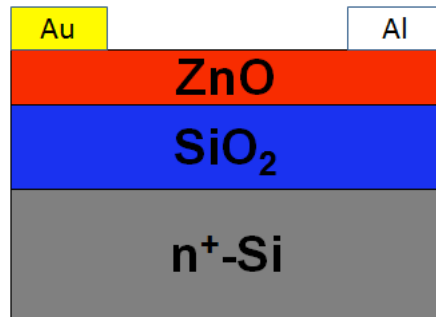
Figure 4-1 Structure of source gated transistor.(Adapted with permission from Ref[1] ;Copyright American Chemical Society)

Figure 4-2 shows the band diagram from the source electrode. The electrons at the source trying to enter the semiconductor encounter a barrier at the source-semiconductor interface ϕ_B. This barrier could be made by using a metal-semiconductor Schottky barrier. By applying a positive voltage to the gate, electrons are accumulated at the semiconductor-insulator interface. Applying a positive voltage to the drain will reverse bias the Schottky barrier. Increasing the drain voltage, results in the extension of the depletion region. Hence the semiconductor around the source region will be depleted of free charge carriers causing the drain current to saturate.[210]

In addition to Schottky barriers, other barriers could be used in the source contact. The important character required for the barrier is the capability of depleting the semiconductor-insulator interface of free charge carriers. Unipolar diode structure, metal-insulator-semiconductor barrier, and space charge limited sources are other potential options used for barrier sources.[208]

Generally source-gated transistors are suitable candidates for poor quality semiconductors. Defects and impurities introduce a wide range of defects in the bandgap. The defects in the bandgap could be due to bond angle and bond length variations, coordination defects (in amorphous materials), and grain boundaries (in polycrystalline materials). Stutzmann suggests defect formation under charge injection is a general phenomena for disordered semiconductors.[211] Based on this theory, occupation of localized defect states causes defect formation. Hence states are created in disordered

semiconductor to minimize the excess carrier concentration. For instance in the amorphous silicon electrons can break weak silicon-silicon bonds creating defect states deep in the bandgap.[212] The columbic interaction between carriers or ionized dopants and carriers is another source for creating deep states in the bandgap. Hence it can be concluded that in order to reduce the defect formation when the transistor is on, the excess charge carrier concentration must be small.[212]

Mobility is another important parameter in transistor operation. Increasing the number of defects degrades the mobility causing the carriers to be trapped in the localized states. In these cases the charge transport occurs by hopping or tunneling between states. Hence these cases exhibit low mobility values. By increasing the carrier velocities by applying high internal fields, the issue of low mobility in highly disordered semiconductors can be mitigated. Hence, in designing a transistor in order to obtain high operational speeds, the active region of the transistor must have high internal fields and this region must have small dimensions. Hence stable transistors have the following conditions: 1- low carrier concentration 2- operation with high internal fields in the active part with small dimensions. The first condition increases device stability while condition two increases the speed of transistor.[212] The source gated transistor is compatible with all these requirements.

The reverse bias Schottky contact will influence the performance of the device. Due to the limiting effect of the barrier on the current, the current of Schottky contact transistor is smaller than conventional FETs. In conventional FETs, at a drain voltage equal to the difference of gate voltage and threshold voltage, the transistor saturates. In the case of source-gated transistors, for small positive drain voltages the semiconductor-insulator interface will have electron accumulation and source barrier will be under reverse bias (figure 4-2 (a)). Increasing the drain bias extends the depletion region to the semiconductor-insulator interface. In this case ($V_D=V_{sat}$) the source can be modeled as two dielectrics in series (figure 4-2 (b)). In this case increasing the drain voltage has no effect on the voltage at the interface. By changing the voltage at the gate, the voltage change in the interface is:

$$\Delta\psi = \frac{C_G}{C_G + C_S}\Delta V_G = \Delta V_{sat} \qquad (4\text{-}1)$$

where C_G and C_S are capacitances of insulator and semiconductor layers, respectively. In this case the change in the electric field at the barrier is $\Delta\psi/t_s$ where t_s is the semiconductor thickness. The drain voltage has to be more positive than ψ to sweep out the electrons. Hence for source-gated transistors we have:

$$V_{sat} = \frac{C_G}{C_S + C_G}(V_G - V_{TH}) + K \qquad (4\text{-}2)$$

where V_{TH} is the threshold voltage for accumulation, and K is a constant that takes in to account the drain voltage required to deplete the semiconductor and interface at $V_G = V_{TH}$.[213] From the above equation it is observed that using a thin semiconductor layer or a thick dielectric layer can reduce the saturation voltage for source-gated transistor compared to conventional FETs. For a given drain current, the power dissipation of each device is proportional to the voltage drop on each device. Hence lower saturation voltage is equivalent to lower power dissipation. However, lower saturation voltage results in lower transconductance for the transistors as well.[214]
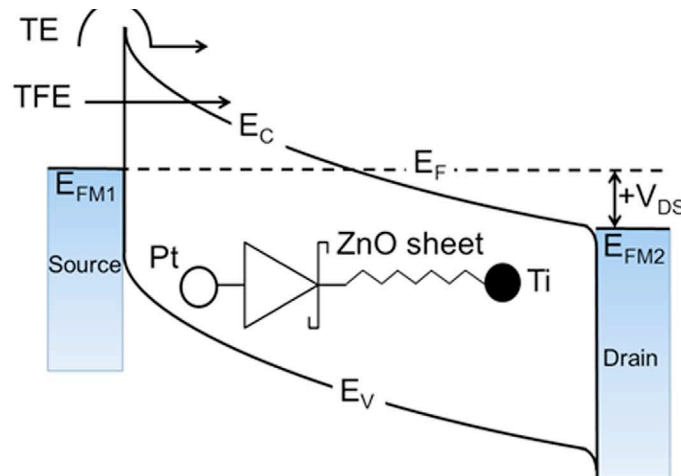
Figure 4-2 Band diagram of source gated transistor. (Adapted with permission of Ref[215] ; Copyright nature publishing group)

Hence saturation voltage well below $V_D=V_G-V_{TH}$ can be obtained. In this case when the transistor is saturated, the characteristic becomes extremely flat (hard saturation) which is a desirable aspect in analog amplifiers and current sources. Additionally hard saturation behavior results in power saving since by increasing the drain voltage the current shows a constant behavior.[214] As for the frequency response of the source-gated transistors, by performing first order analysis using small signal equivalent circuit, it can be proven:

$$f_T \approx \frac{q}{kT} \frac{\alpha J_S}{2\pi\varepsilon_s\varepsilon_0} \tag{4-3}$$

where α is the effective barrier lowering constant (tunneling constant) for cases which thermionic-field emission dominates the current, J_S is the average current density and ε_s is the semiconductor permittivity. Hence as long as the current is determined by source barrier (not the parasitic FET), f_T is independent of insulator and semiconductor thicknesses, insulator permittivity, and carrier mobility. Hence, by reducing the source length the current density and operating frequency will increase.[216] Additionally, it is observed that the distance between the drain and source plays no role in frequency response. Reducing the drain-source voltage can increase the internal fields of SGT transistors.[214] As for the effect of process variation on the drain current, the current is insensitive to the variation of separation between source-drain contacts and source length. However, insulator thickness and barrier height variation play a crucial role on the drain current variation.[217]

As mentioned above, the excess carrier concentration could cause stability issues in the transistor operation. The number of excess carriers can be controlled by controlling the source barrier height in source-gated transistors. This reduces the charge carrier concentration compared to conventional FETs leading to improved stability. This improved stability to electrical stress is crucial for analog applications and results in elimination of compensating circuitry reducing circuit complexity.[214]

The drain current also exhibits temperature dependence in source-gated transistors. By increasing the barrier height, the drain current is highly temperature dependent which could be useful in temperature sensor applications. On the other hand by using low

barrier heights low temperature coefficients are obtained.[214] In the next part, we will fabricate solution processed ZnO Schottky barrier transistor.

4.3   Experimental procedure

The precursor solution consisted of zinc acetate dihydrate (Fisher Scientific) mixed with triethylamine (99%, Sigma-Aldrich) in a 1:1 ratio. 2-Methoxyethanol (99%, Acros Organics) was added to make 100 mL of the solution. The solution was stirred and heated at 120 ^{o}C for 4 hr until it became transparent. Two solutions of 0.1 M and 0.25 M zinc acetate were made using this recipe and spin coated on to 200 nm-thick thermally grown oxide-coated n^+-type silicon wafers. The $n+$-Si/SiO$_2$ substrates were dried at 130 ^{o}C. Subsequently, they were annealed at 500 ^{o}C for 90 minutes. This process was repeated three times. The 0.1 M, 0.25 M, and 0.25 M solutions were used for each cycle, respectively. The thickness of the film measured using ellipsometry was 46 nm and confirmed by stylus profilometry to be ~50 nm. Film morphology was imaged using a Hitachi S-4800 cold cathode high resolution field emission scanning electron microscope (FESEM). Au and Al were used as the Schottky and ohmic contacts, respectively. Metallization was performed using DC sputtering on photolithographically patterned substrates. A three-step photolithography process was used to define the electrodes including a mesa step to electrically isolate individual TFTs. X-ray diffraction (XRD) patterns were collected from the ZnO films at glancing incidence using a Rigaku Ultima IV diffractometer. The electrical characteristics of the ZnO devices were measured on a Signatone Probe Station using a Keithley 4200-SCS semiconductor parameter analyzer.

4.4   Results and discussion

4.4.1   Film Growth
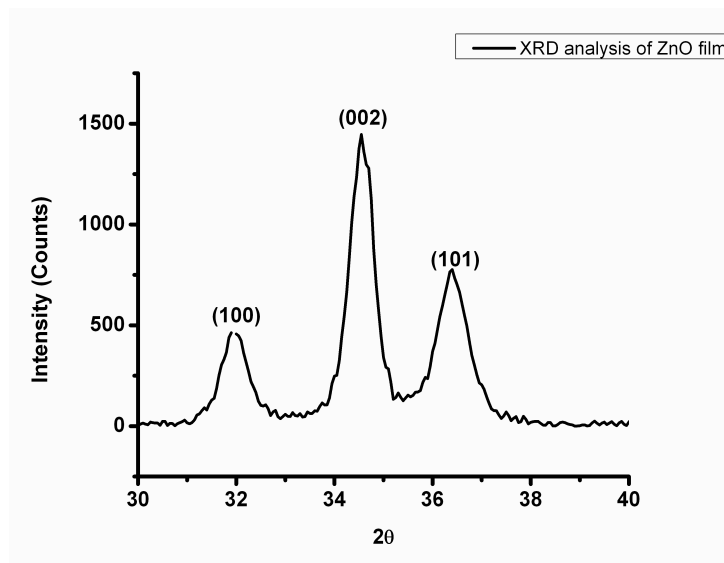
Figure 4-3 X-ray diffraction of ZnO film. Three peaks observed for sol-gel ZnO:(100),(002),(101). The (002) peak is not dominant. Using Scherrers formula grain size is calculated as 16nm. (Adapted with permission from Ref[1] ;Copyright American Chemical Society)

It is known from several prior studies that the temperature and duration of pre- and post-annealing processes determine the orientation of ZnO films prepared using zinc acetate as the precursor, monoethanolamine as the stabilizer and 2-methoxyethanol as the solvent.[135,164,171,85,218] The effect of the precursor is well-studied with reports showing that zinc nitrate results in a rough dendritic film morphology with smaller grain sizes compared to zinc acetate, which results in smoother, larger-grained films.[144] Likewise, it is also known that higher precursor concentrations[219] and higher boiling point solvents favor larger grain sizes. However, the effect of stabilizer on the properties of films has not been explored yet.

We used triethylamine as the stabilizer in the solution growth process because of its ability to coordinate to Zn^{2+} ions and prevent premature methathesis reactions. The Triethylamine adduct of dimethylzinc is widely used as a precursor for the growth of ZnS, ZnSe and ZnO.[220, 29] Triethylamine also assists in the hydrolysis of zinc acetate to form ZnO. The XRD patterns collected from the ZnO thin films are shown in figure 4-3 and indicate three major peaks: (100), (002) and (101) which are commonly observed for solution-processed ZnO. In order to achieve better crystallinity, the preheating method proposed by Ong et al[137] was used for annealing the ZnO films. This method is reported

to generate ZnO films with a preferred (002) orientation which results in better charge transport.[137] The replacement of monoethanolamine by triethylamine as the stabilizer in our process significantly influenced the doping and crystallinity of the film. The ZnO films no longer possess a preferred orientation as can be seen in figure 4-3. This shows that the result obtained by the preheating annealing method is sensitive to the recipe used.

An FESEM image of the morphology of the obtained ZnO film is shown in figure 4-4. The lateral grain size was observed to be 15-40 nm from the FESEM image while the value deduced from XRD measurements using the Scherrer equation was found to be 16 nm. Since the ZnO film was formed in a sequence of 3 cycles as indicated in the experimental details, we surmise that smaller grains closer to the interface are obtained in the first cycle using lower concentration ZnO precursor which are responsible for the peak broadening in the XRD pattern. These grains act as nucleation sites for larger grains that form in the subsequent cycles using higher concentration ZnO precursor. These larger grains constitute the top surface of the film imaged by FESEM. As can be seen from the image, the surface of the film is very smooth with no cracks and pores.

Compared to results obtained in the literature with monoethanolamne as the stabilizer, the ZnO films grown by us using triethylamine as the stabilizer have smaller grain sizes and are less orientated in the (002) direction. Since the c-axis is the most facile direction of growth for ZnO, we infer from the FESEM and XRD results that the complexation of zinc cations with triethylamine results in a lower nucleation barrier and a higher crystallization barrier when compared to complexation with monoethanolamine. This is likely due to the differences in bonding and boiling points between the two stabilizers (boiling point=170 °C for monoethanolamine and boiling point=89 °C for triethylamine).[221]
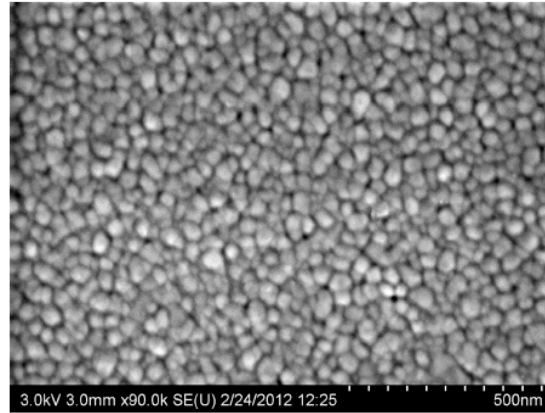
Figure 4-4 FESEM image of the morphology of the ZnO film. The film is continuous with no pores or cracks. The grain size is 15-40nm. (Adapted with permission from Ref[1] ;Copyright American Chemical Society)
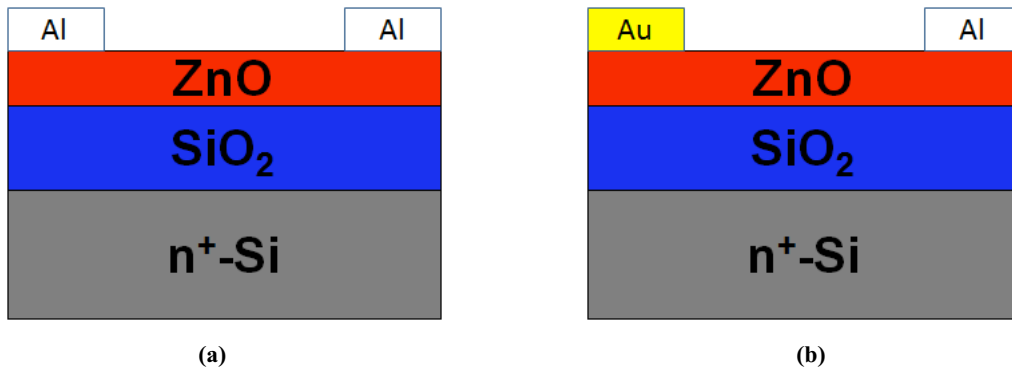
Figure 4-5 Structure of a) typical symmetrical ZnO TFT on a Si substrate and (b) asymmetrical TFT used in this work.work. In the symmetrical TFT, both contacts are ohmic. In the asymmetrical TFT, one contact is ohmic and another is a rectifying contact due to the Schottky barrier. When the Schottky junction is forward biased, the asymmetrical TFT behaves similar to the symmetrical TFT.   When the Schottky junction is reverse biased, the behavior of the asymmetrical TFT diverges from that of the symmetrical TFT. (Adapted with permission from Ref[1] ;Copyright American Chemical Society)

4.4.2   Device configuration and theory of operation

FETs employ the field effect of the gate to modulate the conductance of the channel between two ohmic contacts. The FET is in saturation when the semiconductor channel is pinched off at the drain. Metal-semiconductor field-effect transistors (MESFETs) offer higher channel mobilities than metal-insulator-semiconductor field-effect transistors (MISFETs) due to lower scattering at the semiconductor-gate dielectric interface but present the problem of a higher leakage current. Schottky barrier gate electrodes have been used in ZnO MESFETs to retain the advantage of high mobility while decreasing

the leakage current.[222] In contrast, Schottky barrier thin film transistors (SB-TFTs) use a Schottky contact as the source or drain electrode to limit the drain current of the transistor.[223] Other methods to limit the drain current include the use of a unipolar barrier, MIS barrier, and space charge limited barrier.[208]

Among these methods, the Schottky barrier method is the simplest. By changing the height of the barrier by varying the gate electric field, the magnitude of the drain current is changed. In figure 4-5, we have drawn a distinction in the back-gated configuration between the structure of a typical TFT with symmetrical source/drain electrodes and the asymmetrical SB-TFT, which is the subject of the present study. As shown in figure 4-5, we used Al as the ohmic contact at the drain electrode and Au as the Schottky contact at the source electrode.

Figure 4-6 is a schematic diagram of the band line-up at the source-semiconductor-insulator interfaces. At zero gate bias (V_{GS}), the semiconductor is depleted of charge carriers near the source due to the presence of the Schottky barrier and its accompanying depletion region. Therefore, the TFT is in the OFF-state at zero gate bias. The Schottky contact at the source is reverse-biased by the application of a positive drain bias (V_{DS}) and thus limits the injection of electrons from the source into the channel. Therefore, by applying a positive voltage at the drain, and increasing the same, the semiconductor near the source becomes further depleted of free charge carriers and the channel remains switched OFF. In this regime, the drain current becomes independent of the drain voltage and will only depend on the gate voltage. By applying a suitable positive voltage to the gate, the electrons are accumulated at the semiconductor-gate dielectric interface and the channel becomes conducting corresponding to the TFT being ON. The positive V_{DS} will increase the size of the depletion region under the source and cause it to extend to the semiconductor-gate dielectric interface as the drain voltage is increased. Hence no free charge carriers will be present in the semiconductor under the source. At this point the drain current saturates. As a result the drain voltage will have no further effect on the magnitude of the drain current. The Schottky barrier causes the transistor to saturate at lower voltages. Hence the transistor can operate at lower voltages which in turn reduces

the power consumption.[210] It is well-known that the threshold voltage of polycrystalline ZnO TFTs shifts with time due to changes in the distribution of traps at grain boundaries and at the gate dielectric interface.[224] By making the threshold voltage dependent on the source injection barrier, such variations in the threshold voltage are circumvented. Furthermore, since a positive gate voltage is required to make the channel conductive, the device operates in enhancement mode.
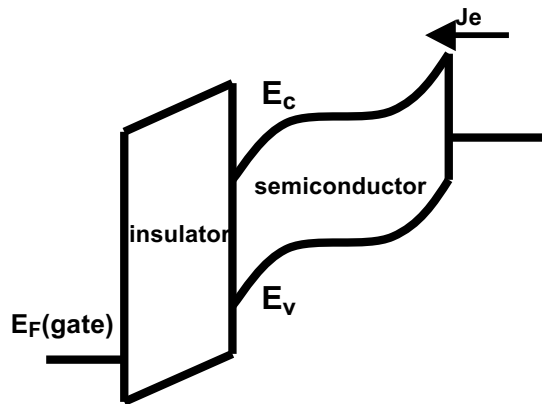
Figure 4-6 Source-semiconductor-insulator band diagram.
(Adapted with permission from Ref[1] ;Copyright American
Chemical Society)

When V_{DS} >0 the Schottky contact will be reverse biased widening the depletion region, making the region around the source depleted from free charge carriers. Hence the amount of current will be independent of drain voltage (pinch off). By applying a positive voltage, the channel is formed by the accumulation of negative charge carriers.

4.5 Electrical characteristics of ZnO SB-TFTs

Figure 4-7 shows the electrical characteristics of Schottky TFTs for different gate voltages and device dimensions. In figure 4-7, the I_D-V_{DS} characteristic of a device with channel length of 20 μm and width of 100 μm is plotted for both negative and positive values of the drain voltage. Unlike a regular TFT, which is expected to exhibit symmetrical characteristics for $\pm V_{DS}$, the n-ZnO SB-TFT fabricated by us exhibits highly unsymmetrical I-V characteristics. At negative V_{DS}, the Au-ZnO Schottky barrier at the source is forward biased and there is a very small barrier to injection. Furthermore, the ZnO films formed using the above procedure are heavily n-doped, as will be shown

91

below. Consequently, except for a small region of sub-linear slope at low V_{DS}, the I_D-V_{DS} characteristics are linear like those of a simple resistor when the Au-ZnO junction is forward biased. In contrast, for positive V_{DS}, the Au-ZnO junction is reverse-biased and the I-V characteristics are those of a transistor for lower drain source voltages. Likewise, the SB-TFT with a channel length of 50 μm and a width of 200 μm in figure 4-7(b) shows a nearly ideal transistor characteristic at positive V_{DS}. The slope of I_D-V_{DS} is very small in the saturation region, which indicates that the transistor is in hard saturation. This proves that the transistor has high output impedance, which is a desirable feature for most applications.

(a)

(b)

(c)
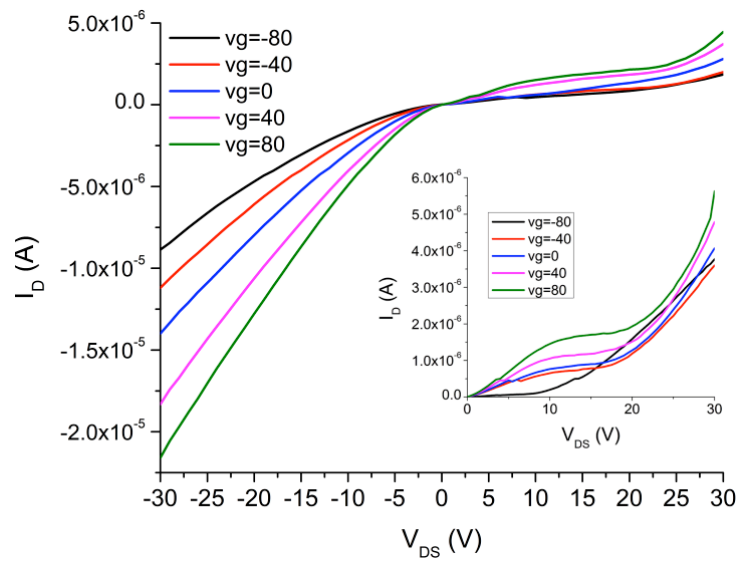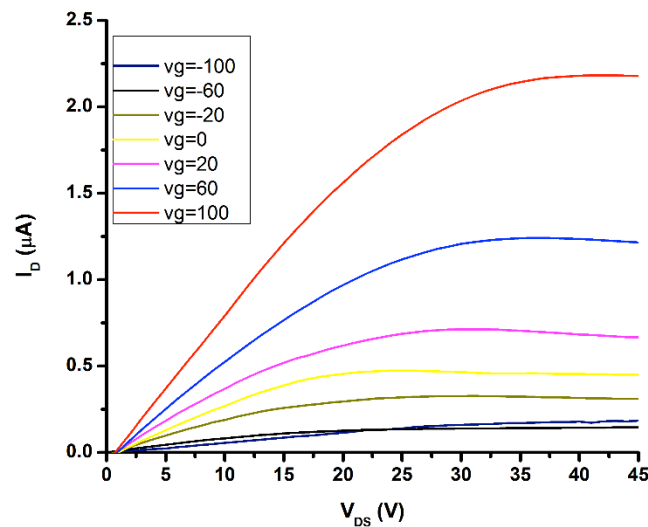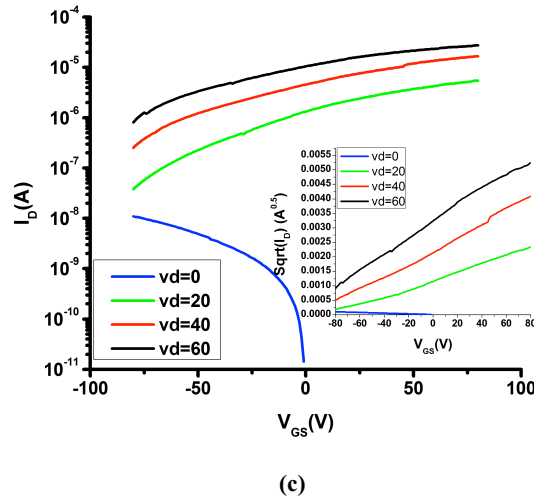
Figure 4-7 I_D-V_{DS} **of ZnO TFT with Au Schottky contact and Al ohmic contact a)** I_D-V_{DS} **of TFT (***W*=100 um,** *L*=20 um). Inset showing the bias of the same device under positive device. b)** I_D-V_{DS} **of TFT with** *W*=200 um** *L*=50 um. c) Log** I_D-V_{GS} **for (***W*=200 um *L*=50 um). (Adapted with permission from Ref[1] ;Copyright American Chemical Society)**

It is clear that each device has two points in reverse bias at which it's behavior changes. One point is the drain voltage (V_{DSat}) at which the drain current saturates. Another point is the voltage at which the saturated drain current begins to sharply increase again (V_{Rt}). The lateral electric field in the channel for the same drain voltage increases with decreasing channel length. This causes lower channel length devices to saturate at smaller values of the drain voltage (lower V_{DSat}) and allows the reverse tunneling currents to re-assert themselves at smaller values of the drain voltage (lower V_{Rt}). Thus at channel lengths at the lower end of the range used in our study, contact effects dominate the transport and the influence of the gate is reduced.

Figure 4-7(c) shows the I_D-V_{GS} characteristic, which shows an on/off current ratio of 100. The behavior of the TFT at V_{DS} =0 is different from other values of drain-source voltage. This is because when V_{DS} =0 the only voltage that affects the Schottky barrier is the V_{GS} voltage. As V_{GS} decreases, the barrier height reduces resulting in an increase in the current. However, when a positive value of V_{DS} is applied, the drain bias dominates the behavior of the Schottky contact making it reverse biased. As the V_{GS} increases in this case, more negative charge carriers are accumulated in the channel and the current

increases. A threshold voltage of -110 V and a saturation mobility of 0.01 $cm^2V^{-1}s^{-1}$ were extracted from the slope of $\sqrt{I_D}$- V_{GS} characteristic (figure 4-7(c)). A linear mobility of 5.7×10^{-3} $cm^2V^{-1}s^{-1}$ was obtained from the transconductance curve.

As mentioned previously, the ZnO TFT behaves as a resistor when the Schottky barrier is forward biased. As can be seen from figure 4-7, the Schottky barrier causes the transistor to saturate at lower gate voltages. Due to the low threshold voltage of -110 V, the transistor turns off at gate biases lower than -110 V, which can not be applied to the gate due to instrument limitations. This shows that the transistor is an *n*-type depletion mode transistor since negative voltage is needed to turn the device off. Our best devices yielded on/off current ratios of ~10^3. The reason behind both the low on/off current ratio and the low threshold voltage is the high doping level of ZnO. The present charges in the bulk region is another factor contributing to the off current of the transistor hence reducing the on/off current ratio.

High doping increases the charge carrier tunneling thus increasing the leakage current. Since charge injection from the source into the channel is controlled by tunneling, the width of the barrier plays an important role along with the height of the barrier. In our device configuration, the gate bias modulates not only the resistance of the ZnO in the channel region but also modulates the resistance of the rectifying contact. When the Schottky junction is reverse biased, the gate voltage modulates the conductance of the channel as follows[225] : at gate bias lower than the threshold voltage, the width of the tunneling barrier is significant and injection from the source is limited due to the confinement of electrons by the Schottky barrier – this corresponds to the OFF state ; at gate bias larger than the threshold voltage, the width of the tunnel barrier is reduced by the gate electric field rendering the barrier nearly transparent thus allowing electron injection from the source by field emission – this corresponds to the ON state.

Despite the high doping level of the ZnO and the poor rectification provided by the Au-ZnO junction, SB-TFTs allowed control over the electrical characteristics, which approached ideal transistor behavior. The effectiveness of the asymmetrical SB-TFT concept is thus demonstrated. Our results clearly indicate that moderately doped ZnO

coupled with strongly rectifying contacts could be used to change the threshold voltage of ZnO devices and achieve stable enhancement mode operation.

One of the issues in fabricating schottky barrier TFTs is the difficulty of fabricating Schottky barriers on sol-gel ZnO. The Au contacts on ZnO behave unpredictably, occasionally resulting in ohmic behavior. The diffusion of Au in to ZnO and the trapped charges at the interface changing the barrier height are some of the possible explanations for this ohmic behavior. Hence choosing metals with a more reliable behavior is crucial. Among the different metals, Ag-ZnO always showed a schottky behavior. This schottky behavior is attributed to the oxidation of silver which can either 1- increase the Ag work function[226] or 2- introduce an intermediate dielectric layer.[203b] Thus we modified the TFT structure by replacing gold(Au) with silver(Ag). In addition we replaced triethylamine with ethanolamine, which results in slightly less doping of the ZnO films. The other fabrication steps are similar to the steps described in the experimental section. Figure 4-8 shows the SEM image of the film deposited using the ethanolamine stabilizer.

Image remove due to lack of copyright permission

Figure 4-8 SEM image of ZnO film deposited using ethanolamine as the stabilizer. (Adapted with permission from Ref[227]; Copyright American Society of Mechanical Engineers)

Figure 4-9 shows the XRD results of the ZnO films.

Image removed due to lack of copyright permission.

Figure 4-9 XRD results of ZnO thin films deposited using ethanolamine as the stabilizer. (Adapted with permission from Ref[227]; Copyright American Society of Mechanical Engineers)

As can be seen from figure 4-9, three peaks are observed for ZnO thin films: (100), (101), and (002). This is an indication of the growth of ZnO films in different directions. Using the Scherer's formula a grain size of approximately 33nm is calculated.

In order to study the effect of schottky contact, two TFTs were fabricated. In the conventional TFT both contacts were ohmic which were fabricated using Al where as in the schottky barrier TFT the source used silver (Ag) as the electrode. Figure 4-10 compares the I_D-V_{DS} curves of the conventional TFT with SB-TFT.

Image removed due to lack of copyright permission

Figure 4-10 Characteristics of TFT with a) schottky source contact b) ohmic source contact (W=200 um L=50 um). (Adapted with permission from Ref[227]; Copyright American Society of Mechanical Engineers)

As can be seen from figure 4-10, the Schottky barrier TFTs, unlike the conventional TFTs, are operating in "hard saturation". This means that the drain current is showing minimum variation. As explained above, this saturation is due to the depletion of the reverse biased source Schottky contacts from free charge carriers. As the voltage of reverse bias is increased, the width of the depletion region also increases resulting in the drain contact being independent of the drain-source voltage.

Figure 4-11 compares the I_D-V_{GS} curves for the conventional and SB-TFTs.

Image removed due to lack of copyright permission

Figure 4-11 Characteristics of TFT with a) ohmic source contact b) schottky source contact (W=200 um, L= 50 um). (Adapted with permission from Ref[227]; Copyright American Society of Mechanical Engineers)

As can be seen from figures 4-10 and 4-11, the conventional TFT has a higher current compared to the SB-TFT. This is expected since the source Schottky contact is reverse biased, thus increasing the contact resistance. Similar to the previous case, both devices are depletion mode devices, which means a negative voltage is required at the gate to turn them off. This results in increased power dissipation and additional complexity in circuit design. Using the slope of $\sqrt{I_D}$-V_{GS} for the drain current in saturation, mobility values of 0.34 and 0.15 $cm^2V^{-1}s^{-1}$ are calculated for conventional and SB-TFTs, respectively. Due to the same deposition conditions, this difference in mobility is attributed to the sensitivity of the TFT measured mobility to the contact resistance.

4.6 Summary

In this chapter we discussed the operating principles of source-gated transistor. Source-gated transistors are suitable candidates for fabricating devices using poor quality semiconductors. Subsequently, we fabricated Schottky barrier thin film transistors using

solution processed ZnO as the active layer with Au as the source Schottky contact. The reversed biased Schottky contact (formed by Au contact on ZnO) depleted the source region from free charge carriers hence driving the device in to saturation whereas in forward bias no saturation was observed. Due to the unpredictable behavior of Au on ZnO, the structure of Schottky barrier was modified by replacing Au with Ag.

5 Effect of Sol Stabilizer on the Structure and Electronic Properties of Solution-Processed ZnO Thin Films

5.1 Introduction

Solution-processed ZnO films are attracting increasing attention for optoelectronic applications due to the unique combination of properties in ZnO such as high transparency at visible wavelengths, high potential carrier mobility, large exciton binding energy and high breakdown electric field, as well as the favorable economics enabled by earth abundance and high-throughput solution processing.

The sol stabilizer used in the solution processing of ZnO functions variously as a sol homogenizer, chelating agent, wettability improver and capping agent. In spite of its obvious importance to influencing ZnO film properties, the effect of the sol stabilizer has not been systematically studied and is generally unknown. Although there are a few papers examining different stabilizers,[155, 162, 228, 163] these studies have been mainly restricted to alkaline short chain ligand bearing species such as ethanolamine, diethanolamine, triethanolamine, etc. Furthermore, these prior reports did not examine the effect of the stabilizers on the performance of the resulting ZnO thin films in optoelectronic devices. Our study also examines longer chain and acidic stabilizers such as oleic acid, oleylamine and octadecene, which are used extensively in the synthesis of colloidal II-VI quantum dots, but have not been used to form ZnO thin films.

We examined the effect of six different sol stabilizers -triethylamine, oleylamine, oleic acid, octadecene, triethanolamine and ethanolamine (along with a sol without any stabilizer), on the grain size, crystallographic texture, and resistivity of solution processed ZnO films on thermal oxide-coated silicon substrates, and found large variations in the structural and electrical properties as a consequence of the choice of sol stabilizer.

In this chapter, we synthesized ZnO films using various sol stabilizers and studied the effect of the stabilizing agent on the morphology, orientation, optical, and electrical

characteristics of the deposited films. The effect of different sol stabilizers on the crystal texture of the films was investigated by studying the XRD results of the films. Raman studies were preformed on the solutions and the films to understand the nucleation and growth of the ZnO films. Four point probe measurements were performed to compare the resistivity of the films. The ratio of the photocurrent to dark current was measured in steady state photoconductivity measurements. By measuring the transient photoconductivity, mobility−lifetime product for photogenerated charge carriers was measured for each film. By performing C-V measurements using impedance spectroscopy, the doping value of each of the films deposited with different stabilizers was measured. Thin film transistors were fabricated and the effect of different stabilizers on their parameters like mobility and threshold voltage was studied. Using the doping values extracted from C-V measurements and the field effect mobility of the TFTs the barrier height of the grain boundaries and the trapped charge density at grain boundaries was calculated.

5.2   Experimental

Zinc acetate dihydrate (ZAC, Fisher Scientific) was the salt used for deposition of ZnO thin films. The sol stabilizers used were as follows: oleic acid (Fisher Scientific, 97 %), triethylamine (Sigma-Aldrich, 99 %), triethanolamine (Fisher Scientific, 97 %), ethanolamine (Acros Organics, 99 %), octadecene (Acros Organics, 90 %) and oleylamine (Acros Organics, C18 content 80-90%). 2-methoxyethanol (Sigma- Aldrich, 99%) was the solvent used. The Si-SiO$_2$ substrates were cleaned in piranha (H$_2$SO$_4$/H$_2$O$_2$ 3:1) solution for 20 minutes.[229]

Three sols of 0.05 M, 0.1 M, and 0.25 M were prepared for each of the stabilizers while maintaining the ratio of [stabilizer]/[Zn^{2+}] at 1. For octadecene and oleic acid as stabilizers and also when no stabilizer was used, the sols were turbid due to insufficient solubility of the precursor in methoxyethanol. These sols were heated while stirring until fully transparent while triethanolamine, triethylamine, ethanolamine, and oleylamine solutions required no heating to form clear, homogeneous solutions. The solutions were spin-coated on to 250 nm thermal oxide-coated Si substrates at 1000 rpm for 60 sec and dried at 120 ^{o}C for 10 minutes and annealed at 500 ^{o}C for an hour.. For each stabilizer,

deposition from solution was performed from lowest to highest concentration (0.05 M to 0.25 M) in sequential order in order to separate the seeding, coarsening and aggregation stages as much as possible. The Al electrodes were deposited using magnetron sputtering at back pressure of 10^{-4} Torr after one step lithography followed by lift-off. The size of electrodes and fabricated devices were 100 μm×80 μm and 500 μm×100 μm, respectively.[229]

The morphologies of the ZnO thin films were imaged using a Hitachi S-4800 field emission scanning electron microscope (FESEM). The X-ray diffraction data was collected in glancing angle mode as well as powder mode by a Bruker D8 Discover system. Raman spectroscopic studies were carried out on both liquid samples (i.e. sols used to deposit ZnO) and films in back scattering mode using Nicolet Almega XR Raman Microscope. Micro-Raman imaging using a 532 nm laser excitation source and a beam spot size of 2 μm was used to record the Raman spectra from the samples. Macro-Raman studies were carried out on the sols. Resistivity measurements were performed using a four-point probe (Lucus Pro 4 4000). Electrical characteristics of the fabricated field-effect transistors were measured in a probe station (Creative Devices) using a Keithley 4200 semiconductor parameter analyzer. For steady-state and transient photoconductivity measurements, 254 nm illumination from a Spectroline E-series UV lamp was used as the excitation source while the electrical characteristics were measured by the Keithley-4200 mentioned above. Electrochemical impedance spectroscopy (EIS) and impedance versus potential data were collected in a three-electrode electrochemical cell with a Ag/AgCl reference electrode, by using a CHI 600D potentiostat (CH Instruments Inc.). All electrochemical measurements used a 0.1 M KCl solution electrolyte at room temperature. Samples were prepared by wrapping parafilm all around except for a 0.5 cm x 0.5 cm area exposed to the electrolyte.

5.3 Results and Discussion

5.3.1 Raman studies of sols containing different stabilizers

Raman spectroscopy is a potent characterization technique for understanding the vibrational properties of ZnO structures. Raman studies were carried out on both solution

samples and the deposited films, using different stabilizers to understand the nucleation and growth of ZnO films. Local vibration modes of ZnO observed in the Raman spectra are shown in figure 5-1. Figure 5-1(a)-(c) show the Raman spectra of zinc acetate dissolved in 2-methoxyethanol. A1(TO), E2(high), and B2(silent mode) are modes related to Zn-o covalent bonds.[229]

Table 5-1 Raman modes acquired from zinc acetate dissolved in methoxyethanol. (Adapted with permission from Ref[229] ;Copyright Royal Society of Chemistry)

Modes present	Raman Shift (cm^{-1})
A1(TO)	375
E2(high)	431.1
B2(silent mode)	540
C-H bond	832.2
Ethanol	891.7
(C-C) vibrations, zinc acetate in ethanol	971.1
(C-O-C) stretching	1126.6
In plane bending vibrations	1281
CH_3 asymmetric bending due to methoxy	1455.2
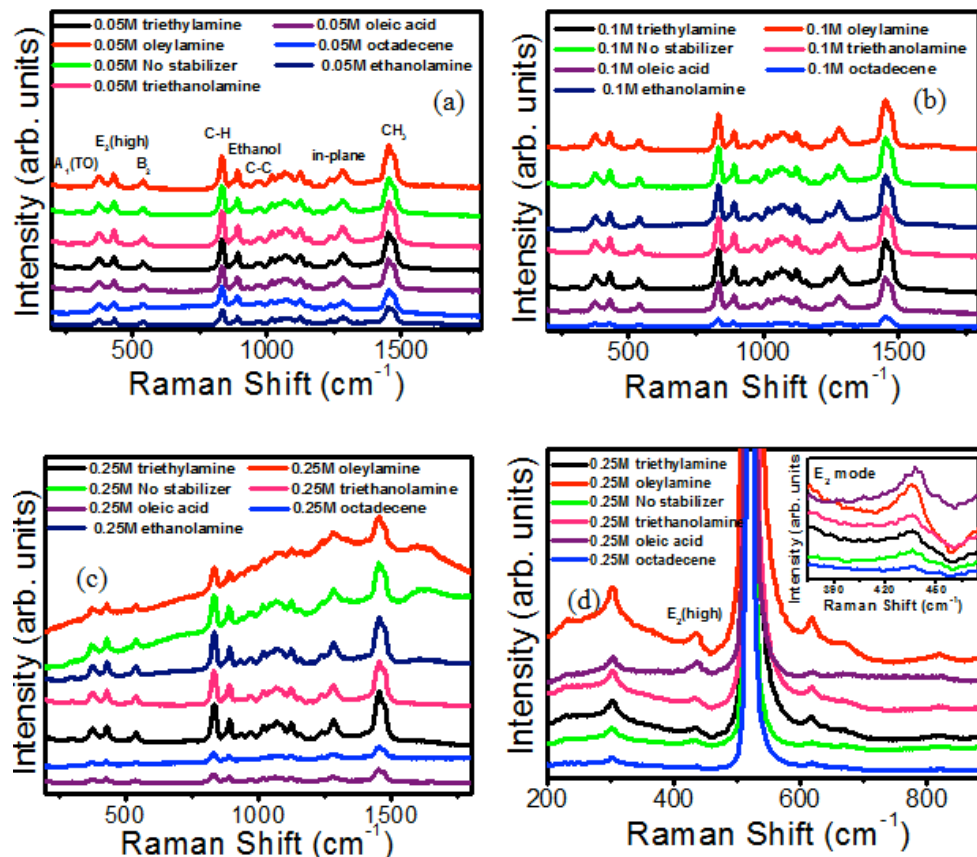
Figure 5-1 (a-c) Raman spectra of zinc acetate solutions dissolved in methoxyethanol using various stabilizers at concentrations a) 0.05 M b) 0.1 M c) 0.25 M. d) Raman spectra of ZnO films on Si substrates. (Adapted with permission from Ref[229] ;Copyright Royal Society of Chemistry)

The spectra were acquired using various stabilizers for the three sols with precursor and stabilizer concentrations of 0.05 M, 0.1 M and 0.25 M, respectively, used for the growth of ZnO samples. The results revealed the presence of ZnO and the various chemical entities involved during initial growth, and support the results of two other studies that also reported the formation of ZnO seed crystals in methoxyethanol sols prior to spin-coating and subsequent pyrolysis. The presence of a peak at a wavenumber of 431 cm^{-1} is due to the Zn-O bond with presence of A1 and B2 modes.[230] The presence of these modes confirm the nucleation of ZnO in liquid while the amplitudes of A1, B2 and E2 modes suggest homogeneous nucleation to be similar in all the sols studied with the exception of the heated octadecene sol, where it was significantly weaker for all the three concentrations studied.[229]

Another interesting observation was that homogeneous nucleation in ethanolamine-based sols became stronger as the concentrations (of precursor and stabilizer) increased while the reverse was true of the oleic acid sol. Raman modes towards higher wave number (800 cm^{-1}- 1500 cm^{-1}) originate due to C-O, C-H bonds and various carbon entities involved.[231] The Raman modes present are indicated in Table 5-1. The presence of all the mentioned peaks were found for sols of all the three different concentrations used in this study. However, in oleylamine sols and sols containing no stabilizer samples with 0.25 M precursor concentration, a few of the modes disappeared owing to the less stable solutions.[229]

5.3.2 Raman studies of ZnO films:

Raman studies were also carried out on the solution-deposited films to confirm the presence of the ZnO mode as observed for liquid samples. ZnO is a semiconductor with wurtzite crystal structure that belongs to C46v space group.[232] The Raman active phonon modes predicted by group theory are, respectively, A1, E1 and 2E2. Raman spectra of ZnO film is shown in figure 5-1(d). The peak at 436 cm^{-1} is due the presence of E2 (high) mode and corresponds to hexagonal wurtzite phase of ZnO. This is the main ZnO mode that confirms its crystalline nature and phase orientation.[229]

A comparison of the main E2 mode of ZnO films with different stabilizers is shown in an inset image of figure 5-1(d). Highly intense peaks were seen with oleic acid and oleylamine stabilizers in comparison to other stabilizers. The variation in intensities and broadening of peaks with different stabilizers may be attributed to the variation in crystallinity of ZnO thin films using different stabilizers. A very small shift of ~ 2 cm^{-1} is observed in ZnO film with oleic acid (437 cm^{-1}) in comparison to the other stabilizers (436 cm^{-1}). Furthermore, a shift is also seen in the ZnO film samples in comparison to liquid ZnO phase, which may be due to the stresses acquired in the ZnO films on Si substrate. No other Raman modes for ZnO were found in the film spectra. Raman modes at around 302 cm^{-1}, 520 cm^{-1}, and 620 cm^{-1} are due to optic and acoustic modes of silicon substrate.[229]

5.3.3 Effect of sol stabilizer on the morphology and structure of ZnO films

Figure 5-2 shows the morphology of ZnO thin films formed using different sol stabilizers. It is evident that the grain sizes of the octadecene and the no-stabilizer films are smaller compared to the other films. Oleic acid and oleylamine stabilizers result in discontinuous films consisting of large aggregates of ZnO film on different parts of the substrate (Figures 5-2(d) and (e)). The other films are relatively continuous. Triethylamine stabilizer gives a continuous non-porous film with the largest mean grain size of 41.4 nm observed in this study. Figure 5-2(g) shows the films deposited using the ethanolamine stabilizers.[229]

Figure 5-3(a) shows the glancing incidence X-ray diffraction (GIXRD) results of the different films. The (100), (101), and (002) peaks are observed in all the diffractograms but the peak intensities are strongest for films formed from oleic acid-stabilized sols and weakest for films made using oleylamine and octadecene.[229]
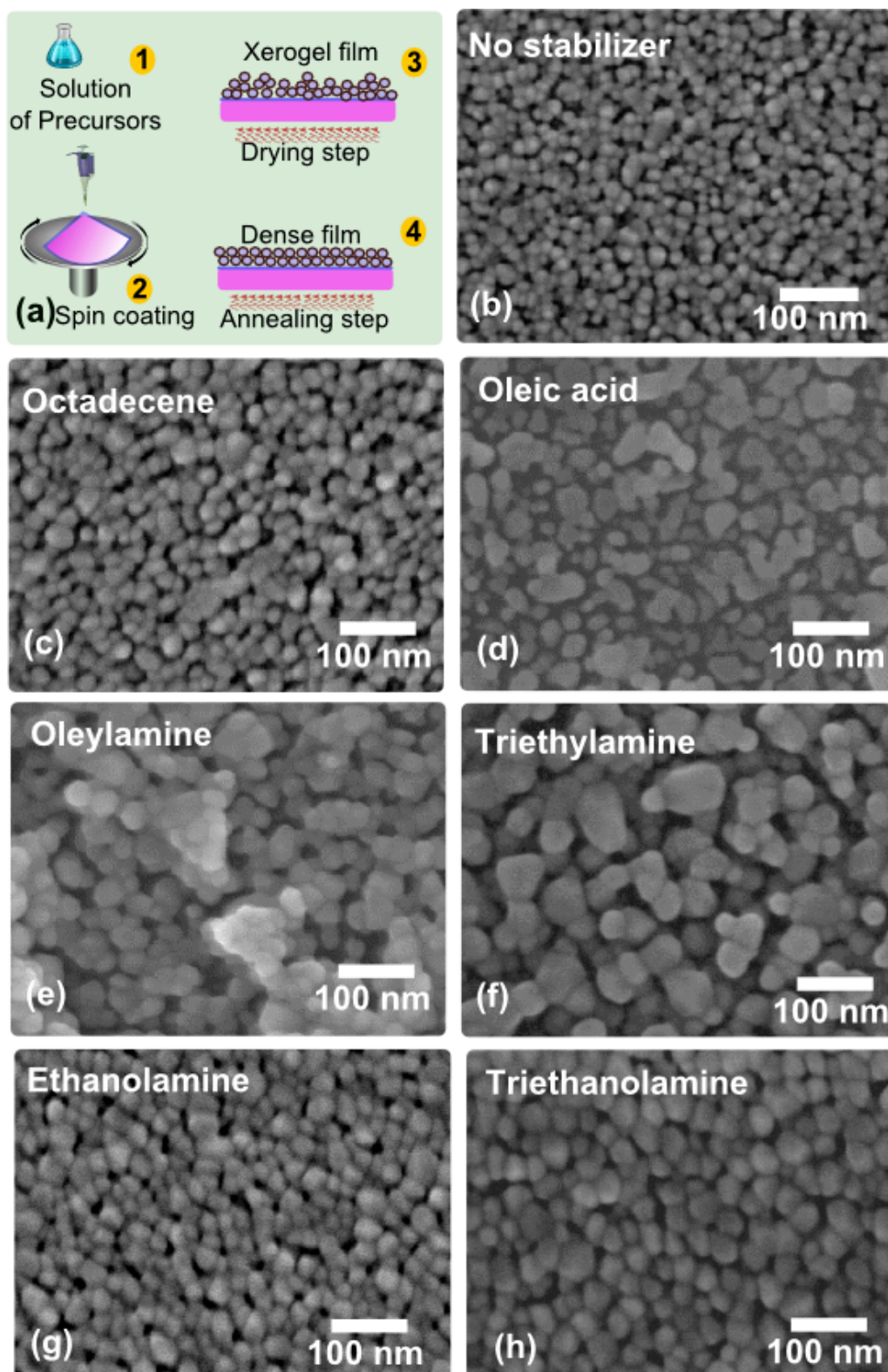
Figure 5-2 a) ZnO thin film deposition method (b-h) SEM images of ZnO films deposited using different sol stabilizers b) no stabilizer c) octadecene d) oleic acid e) oleylamine f) triethylamine g) ethanolamine h) triethanolamine. (Adapted with permission from Ref[229] ;Copyright Royal Society of Chemistry)

Figure 5-3(a) shows the glancing incidence X-ray diffraction (GIXRD) results of the different films. The (100), (101), and (002) peaks are observed in all the diffractograms but the peak intensities are strongest for films formed from oleic acid-stabilized sols and weakest for films made using oleylamine and octadecene. Perusal of the powder XRD data in figure 5-3(b) reveals that the acid-stabilized sol-gel ZnO film alone exhibits a nearly exclusive (002) reflection. The dominance of the (002) reflection in the powder X-ray diffractogram of the oleic acid-stabilized ZnO film demonstrates that the crystallites in the film are arranged such that (002) planes are parallel to the substrate plane or the *c*-axis of the majority of crystallites is oriented perpendicular to the plane of the film.[229] Such a (002) orientation is the preferred orientation for optimal in-plane transport in ZnO thin film transistors.[135]
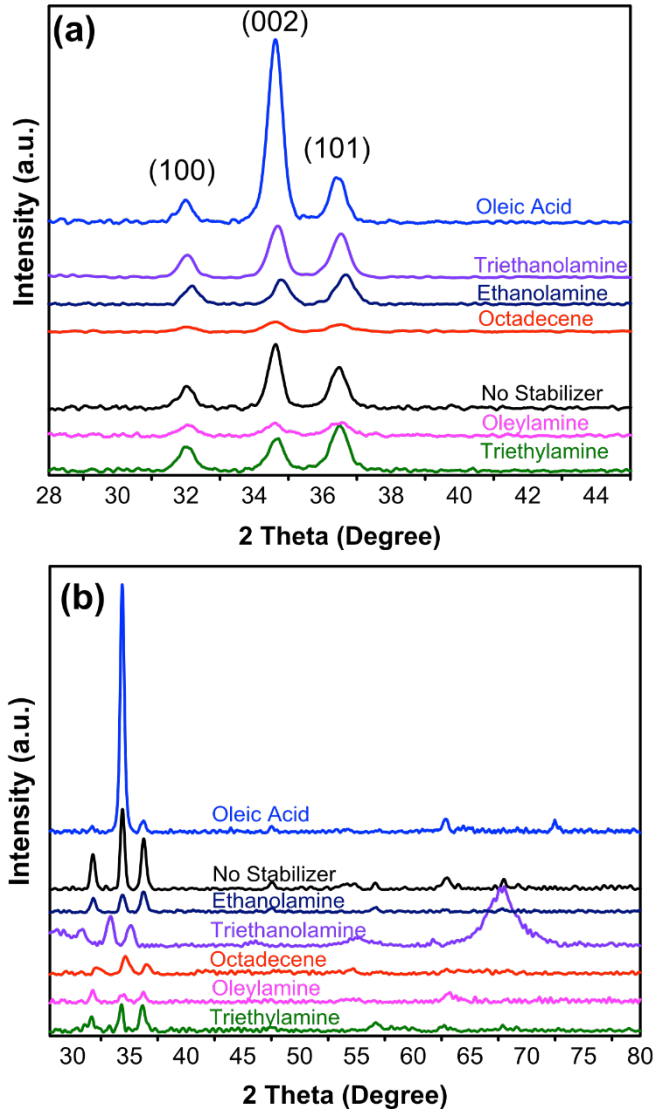
Figure 5-3 X-ray diffractograms of ZnO films deposited using different stabilizers obtained in a) glancing angle b) powder mode. (Adapted with permission from Ref[229] ;Copyright Royal Society of Chemistry)

Since the preferential orientation of the crystallites is an important factor influencing the electrical behavior of the thin films, it is useful to compare the (002) orientation in films deposited using different stabilizers. In order to compare the preferred orientation for different stabilizers, powder XRD data must be used. Figure 5-3(b) shows the powder XRD data for different stabilizers. The Lotgering factor (LF) is a quantitative measure of crystallographic texture and is given by

$$LF = \frac{p - p_0}{1 - p_0} \qquad\qquad (5\text{-}1)$$

where p is the ratio of the summation of integrated intensities of peaks with preferred orientation to the summation of all peaks in the scanned range in the oriented material, and p_0 is the equivalent value for a randomly oriented material.[233] In addition to texture, information about the size of the crystallites can be obtained from the XRD peak widths, which is useful since crystallite size is known to play a significant role in determining the electrical properties of polycrystalline films. Using the Scherer formula, the crystallite size can be calculated as:

$$D = \frac{k\lambda}{\beta_{2\theta}Cos\theta} \qquad\qquad (5\text{-}2)$$

where k is a constant (depends on the particle shape), λ is the wavelength of the used X-ray (λ=1.54 A), and $\beta_{2\theta}$ is subtraction of the instrumental width (0.228^{o}) the full-width at half maximum of (002) peak. Table 5-2 compiles the results and parameters extracted from glancing incidence and powder X-ray diffractograms. As confirmed by the Lotgering factor, in addition to having a large crystallite size, oleic acid produces the highest preferred orientation among the stabilizers. On the other hand, films from oleylamine-stabilized sols are almost randomly oriented with a Lotgering factor of only $0.06.$[229] This is surprising since it is usually thought that increasing the pH using alkaline stabilizers and use of higher pH solvents results in a higher c-axis texture with associated good electrical properties.[234]

Table 5-2 Comparison of the (002) peak location, FWHM, grain size with XRD and SEM and crystal orientation using Lotgering factor. (Adapted with permission from Ref[229] ;Copyright Royal Society of Chemistry)

Stabilizer	Peak Location (002)	FWHM	Grain Size (nm)	Lotgering Factor (LF)	SEM Grain Size(nm)
No stabilizer	34.63	0.47	39.2	0.24	27.5
Octadecene	34.64	0.68	21	0.226	20.6
Oleic acid	34.62	0.5	34.9	0.86	33.5
Oleylamine	34.62	0.52	32.5	0.06	31.6
Triethylamine	34.71	0.48	37.6	0.16	41.4
Ethanolamine	34.79	0.49	36.2	0.138	32.3
Triethanolamine	34.69	0.55	29.5	0.179	29.8

Table 5-3 Resistivity measurements for ZnO films deposited with different stabilizers. (Adapted with permission from Ref[229] ;Copyright Royal Society of Chemistry)

Stabilizer	Resistivity (ohm-cm)	Thickness (nm)
No stabilizer	2.9	19
Octadecene	17.4	20
Oleic acid	138070.5	18(*)
Oleylamine	123191.5	16(*)
Triethylamine	42.5	28
Ethanolamine	169.0	40
Triethanolamine	8.8	32

(*) Oleic acid and oleylamine thickness unreliable due to discontinuity of the films.

Four point probe measurements were performed on the films to understand their electrical properties, and the results are presented in Table 5-3. The thickness of the films was

measured using ellipsometry. The no-stabilizer and triethanolamine films exhibit the lowest resistivities. Among all the films oleic acid and oleylamine have the highest resistivity values. This is expected since both of these are highly discontinuous. Hence the oleic acid films have better crystallinity but are discontinuous. As shown in Table 5-3, except for ZnO thin films synthesized using oleic acid and oleylamine (which have also poor film continuity), the resistivities of the films are quite low due to high bulk dopant densities. The electron mobilities of the polycrystalline ZnO films also differ depending on the stabilizer used, and we show later in this chapter that this arises due to the different inter-grain energy barriers for charge transport.[229]

5.3.4 Photoconductivity of ZnO Thin Films Deposited with Various Stabilizers

In order to study the effect of different stabilizers on the electronic properties of the ZnO films deposited using different stabilizers, steady-state and transient photoconductivity measurements were performed on the films using bandgap illumination at 254 nm. The Al contact electrodes used for figure 5-4 shows on the dark current and photocurrent for films deposited using each of the different stabilizers.
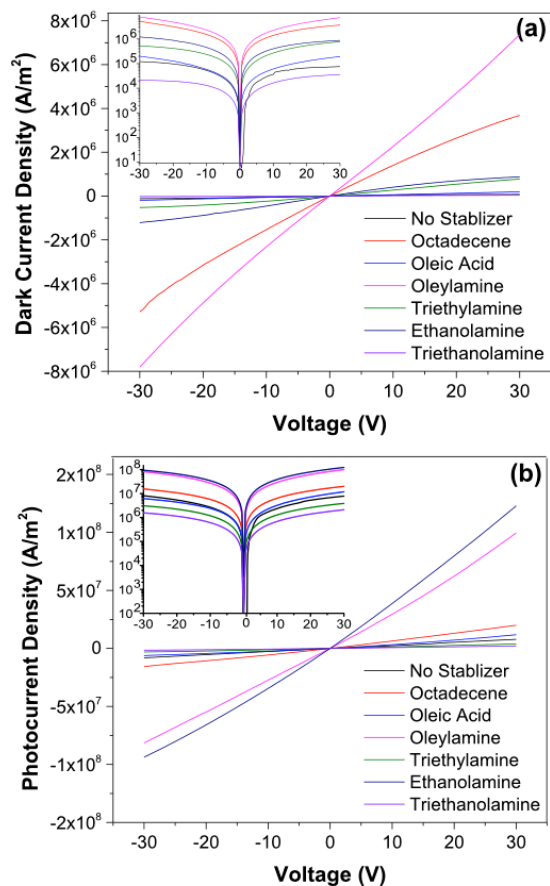
Figure 5-4 Comparison of dark and photocurrent for various stabilizers a) dark current density b) photocurrent density. (Adapted with permission from Ref[229] ;Copyright Royal Society of Chemistry)

Table 5-4 Comparison of drak current and photocurrent density for different stabilizers at 5 V. (Adapted with permission from Ref[229] ;Copyright Royal Society of Chemistry)

Stabilizer	Dark current density (A/m^2)	Photocurrent density (A/m^2)	Photo-to Dark current ratio
No stabilizer	1.75×10^4	1.1×10^6	62.9
Octadecene	7.2×10^5	3.1×10^6	4.3
Oleic acid	3×10^4	1.5×10^6	50
Oleylamine	1.1×10^6	1.4×10^7	13
Triethylamine	1.3×10^5	6.3×10^5	4.8
Ethanolamine	2.1×10^5	1.89×10^7	90
Triethanolamine	8.2×10^3	3.3×10^5	40

The linear and bias-symmetric I-V relationships in the dark current characteristic in figure 5-5 are indicative of ohmic contacts between the Al electrodes and the ZnO films. Under 254 nm illumination, the measured photocurrents also exhibited roughly linear relationships with applied bias and did not saturate for any of the films, confirming secondary photoconductivity to be operating in these films. The lack of saturation also indicates that the applied lateral electric fields are not sufficient to sweep out all the minority carriers (i.e. holes in our case) before recombination with electrons.[229]

Table 5-4 compares the dark current and photocurrent density values for different stabilizers at 5 V bias voltage. As can be seen, for all the stabilizers the amount of photocurrent is higher than the dark current. However, the amount of increase is different for different stabilizers. Ethanolamine and no stabilizer cases show the highest photo-to-dark current ratios (PDR) of 90 and 63 respectively whereas octadecene (PDR of 4.3) and triethylamine (PDR of 4.8) exhibit the lowest ratios.[229] In spite of the simple structure used for the devices, the obtained results for the PDR are in good agreement with the other works available in the literature.[235,64a] These results are also consistent with the PDR obtained using other deposition methods like MBE[236] and CVD[237].

It is well-established that the adsorption interactions of the ZnO surface with ambient oxygen play a huge role in the trapping and recombination kinetics during band gap illumination, resulting in the phenomenon of persistent photoconductivity and concomitant very high photoconductive gain.[198, 238] In the dark, adsorbed oxygen molecules capture free electrons. Hence a depletion region is created near the surface, which degrades the conductivity. This negative depletion region at the surface also causes an upward band bending at the surface. When films are illuminated with energy higher than the bandgap of ZnO film, electron-hole pairs are generated. The electrons will travel to the conduction band while the generated holes will travel to the surface due to the band bending and get trapped with the adsorbed oxygen at the surface. This will result in the desorption of oxygen molecules and lowering of barrier height. Trapping of photogenerated holes at the surface produces desorption of oxygen molecules and also

removes the recombination pathway for photogenerated electrons while the high resulting electron concentration in the ZnO film lowers inter-grain energy barriers. Hence, it can be concluded that both the photogenerated electrons and lowering of barrier height contribute to the current increase.[85]

The differences in the photoresponse of the different stabilizers can be attributed to the different surface states, which are related to the different morphologies of the films.[85] Hence by affecting the actual surface area of the films (which will affect the number of adsorbed oxygen molecules to the surface of the films), the sol-stabilizers cause the steady state responses of the ZnO films to be different for various stabilizers.[229] Using steady state photoconductivity measurements, the mobility−lifetime product of films deposited using different stabilizers can be calculated.[239]

The photoconductivity can be measured as:

$$\sigma_{ph} = eG\left(\mu_n \tau_n + \mu_p \tau_p\right) \tag{5-3}$$

where G is the generation rate, μ_n (μ_p) is the electron (hole) mobility, τ_n (τ_p) is the lifetime for electrons (holes), and σ_{ph} is the photoconductivity which is defined as $J_{diff}=\sigma_{ph}E$ and $J_{diff}=J_{on}-J_{off}$ where J_{on} and J_{off} correspond to the current densities when the UV lamp is turned on and off, respectively. Generation (G) can be defined as:

$$G = \frac{\eta I_0}{h\upsilon}(1-R)\alpha \tag{5-4}$$

where $\eta(=1)$ is the quantum efficiency, I_0 is the intensity of light at the surface of the film (620 μW cm^{-2}), h is the Planck's constant, υ is the frequency, R is the reflection coefficient, and α is the absorption coefficient. Using the values of $\alpha=120000$ cm^{-1} and $R=0.1$ for the wavelength of 254 nm, the generation rate of $G=8.5\times10^{19}$ cm^{-3} s^{-1} is obtained. The product of mobility-lifetime for different stabilizers is shown in table 5-5.

stabilizer	mobility×lifetime (cm^2/V)
No stabilizer	$1.53×10^{-2}$
Octadecene	$3.56×10^{-2}$
Oleic acid	$2.18×10^{-2}$
Oleylamine	$6.80×10^{-2}$
Triethylamine	$7.34×10^{-3}$
Ethanolamine	$2.75×10^{-1}$
Triethanolamine	$4.80×10^{-3}$

The growth and decay times for various stabilizers is shown in figure 5-5.
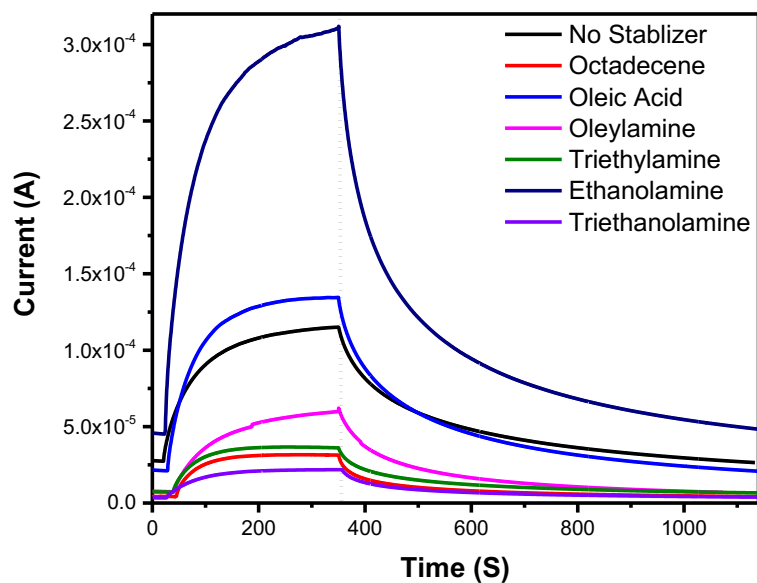
Figure 5-5 Growth and decay time for different stabilizers. (Adapted with permission from Ref[229] ;Copyright Royal Society of Chemistry)

The growth and decay times were measured with a UV lamp of 254 nm wavelength. When the UV lamp was turned on, it was given enough time for the current to stabilize and become constant. The decay diagram of all the stabilizers was best fitted by a bi-exponential curve as:

$$y = y_0 + A_1 e^{-\frac{t}{\tau_1}} + A_2 e^{-\frac{t}{\tau_2}} \tag{5-5}$$

The total time constant of the decay is defined as:

$$\tau_{total} = \frac{A_1 \tau_1^2 + A_2 \tau_2^2}{A_1 \tau_1 + A_2 \tau_2} \tag{5-6}$$

Table 5-6 Fitting parameters for decay of different stabilizers. (Adapted with permission from Ref[229] ;Copyright Royal Society of Chemistry)

Stabilizer	A1	τ1	A2	τ2	τtotal	Reduced chi-sqr	Adj R-sqr
No stabilizer	0.76	41.7	2.2×10^{-4}	315.8	42.3	9.7×10^{-14}	0.99973
Octadecene	60.8	25.3	6.3×10^{-5}	235.4	25.33	3.4×10^{-14}	0.99846
Oleic acid	3×10^{-4}	276.6	1.1	39.7	40.17	7.8×10^{-15}	0.99924
Oleylamine	270.1	37.7	0.001	244	37.7	2.2×10^{-12}	0.99982
Triethylamine	5.6×10^{-4}	272.8	0.73	32	32.34	2.3×10^{-14}	0.99923
Ethanolamine	5.7×10^{-4}	270	4	37.8	38.03	1.9×10^{-12}	0.99931
Triethanolamine	0.33	33.7	3.5×10^{-5}	260.3	34	7.8×10^{-15}	0.99924

As explained above, the adsorbed oxygen at the surface of the ZnO thin films has an important effect on the photoconductive behavior of ZnO thin films. Higher surface area films will have more adsorbed oxygen, which will influence their photoconductive

response.[229] Therefore measurement of the surface areas of the films is useful in order to understand the photoconductivity response of ZnO thin films. In the next section by measuring the actual surface area of the films using the EIS method the relationship between the surface area and time decay constant will be discussed.

The measurement of two time constants from the decay graph can also be explained from the adsorption of oxygen molecules. The smaller time constant is related to the surface states. The oxygen molecules fill these surface traps faster. As for the bulk traps, the oxygen molecules need to diffuse through the ZnO film and fill the traps. The larger time constant of the decay curve is attributed to the diffusion of oxygen molecules and filling the traps.[229]

5.4 EIS Measurements

The surface area and doping of ZnO films were measured using impedance spectroscopy. EIS data was collected in the capacitive regime where blocking behavior is observed. This occurs at potentials more positive, but close to the open circuit potentials which for the ZnO films were obtained from Tafel plots (shown in Fig. S1 in the appendix section). Nyquist plots (Fig. S2a in appendix section) show EIS data for ZnO films grown using various stabilizers. The lumped equivalent circuit obtained from the Nyquist plots is shown in Fig. S2b in the appendix section. The effective capacitance (C_{eff}) was calculated in terms of the electrolyte resistance (R_s), constant phase element (CPE) Q_1, and n_1, which is the exponent of Q_1.[240] Values of Q_1 and n_1 were obtained by solving the equivalent circuit model for EIS (Fig. S2a) which were collected at the potential of −0.2 V (w.r.t. Ag/AgCl). Values of n_1 varied between 0.8 and 1, implying capacitive behavior.

$$C_{eff} = Q_1^{\frac{1}{n_1}} R_s^{\frac{1-n_1}{n_1}}$$

(5-7)

The actual surface area of ZnO films is given in the equation below, and can be expressed in terms of C_{eff}, vacuum permittivity (ε_0), dielectric constant of zinc oxide (ε_s), and thickness of the zinc oxide film (L).[241]

$$A = \frac{C_{eff}}{\varepsilon_s \varepsilon_0} L \qquad (5\text{-}8)$$

The thickness of each ZnO film was measured with ellipsometry and confirmed with profilometry. For geometrical surface areas of 0.5×0.5 cm^2, the actual to geometrical surface ratios were calculated and also listed in Table 5-7.

Table 5-7 Actual/geometrical surface area and charge carrier concentration (cm^{-3}) measured with EIS for ZnO thin films of various stabilizers. (Adapted with permission from Ref[229] ;Copyright Royal Society of Chemistry)

Stabilizer type	Actual / geometrical surface area	Charge carrier concentration [cm^{-3}]
Oleylamine	3.75	6.26×10^{16}
Oleic acid	5.00	2.10×10^{17}
Ethanolamine	13.8	4.7×10^{18}
Octadecene	2	3.5×10^{16}
Triethylamine	4.67	7.05×10^{16}
Triethanolamine	8.4	7×10^{16}
No stabilizer	6.50	9.40×10^{16}

These actual to geometrical surface area ratios are qualitatively consistent with surface roughness of the films, shown in figure 5-2 and are factored into capacitance values that were extracted from impedance versus potential data, in order to plot the Mott Schottky's plots (shown in Fig. S2c in ESI†).

Comparing the surface area of the continuous films with the tabulated values of the photo-to-dark current ratio (Table 5-4), it is observed that excluding the no stabilizer case, films with a higher surface area also exhibit a higher PDR and a higher photoconductive decay lifetime (Table 5-5). This is consistent with stated mechanism of hole trapping by surface adsorbed oxygen species, which in turn increases the photoconductive gain and photoconductive decay lifetime by removing recombination pathways for electrons. As for the no stabilizer case, we surmise that the high PDR and relatively long decay lifetime result from a high density of impurities (acting as color centers) in addition to surface traps since nucleation and growth of the ZnO films occurred without the presence of coordinating ligands save the solvent itself.[229]

For the discontinuous films (oleylamine and oleic acid) we observe a different behavior. For instance triethylamine has a higher surface ratio compared to oleylamine. However, oleylamine shows a higher PDR. The same behavior is observed for triethanolamine and oleic acid. As mentioned before, oleic acid and oleylamine are rough discontinuous films, which make the measurement of film thickness very difficult. This will lead to errors in calculating the surface area, which causes deviations from the proposed behavior.[229] Table 5-8 ranks the different ZnO films on the basis of their surface area and shows that excepting the no stabilizer case and the discontinuous films discussed above, the trends in PDR and lifetime follow the surface area of the films.

Table 5-8 Relation between the surface area, photo to dark current ratio, lifetime. (Adapted with permission from Ref[229] ;Copyright Royal Society of Chemistry)

Ranking based on ratio of actual to geometric surface area	Photo to dark current ratio	Lifetime (s)	Bulk mobility (cm^2 V^{-1} s^{-1})	Doping (cm^{-3})
Ethanolamine (13.8)	Ethanolamine (90)	No stabilizer (42.3)	No stabilizer (23)	Ethanolamine (4.7E18)
Triethanolamine (8.4)	No stabilizer (62.9)	Ethanolamine (38.03)	Octadecene (11)	No stabilizer (9.4E16)
No stabilizer (6.5)	Triethanolamine (40)	Triethanolamine (34)	Triethanolamine(10)	Triethanolamine (7E16)
Triethylamine (4.67)	Triethylamine (4.8)	Triethylamine (32.34)	Triethylamine (2)	Triethylamine (7E16)
Octadecene (2)	Octadecene (4.3)	Octadecene (25)	Ethanolamine (7.8E-3)	Octadecene (3.5E16)

5.5 Thin Film Transistor Measurements

In order to obtain a better understanding of the electrical properties of the ZnO thin films, TFTs with different stabilizers were fabricated using the bottom gate top contact structures. Figure 5-6 shows the I_D-V_{DS} and I_D-V_{GS} curves of the different stabilizer TFTs.

As can be seen from the I_D-V_{DS} curves, the oleic acid and oleylamine stabilized ZnO films do not show saturation behavior. The other devices exhibit different saturation levels (hard vs soft saturation). Hard saturation is the flatness of the variation of the drain current (I_D) for large drain bias (V_{DS}) and occurs when the entire thickness of the ZnO channel is depleted of free electrons in the drain contact. Devices showing hard saturation have higher output impedance, which is a desirable feature for transistors in circuit applications. Due to the increase of free electrons in the transistor channel at higher

positive gate voltages, achieving hard saturation at higher gate voltages is challenging. As can be seen from the I_D-V_{DS} curves, the TFTs fabricated without stabilizer and with triethylamine stabilizer operate in hard saturation at high gate voltages. As for octadecene and triethanolamine, at high gate voltages soft saturation behavior while hard saturation is observed at low gate voltages.[229]
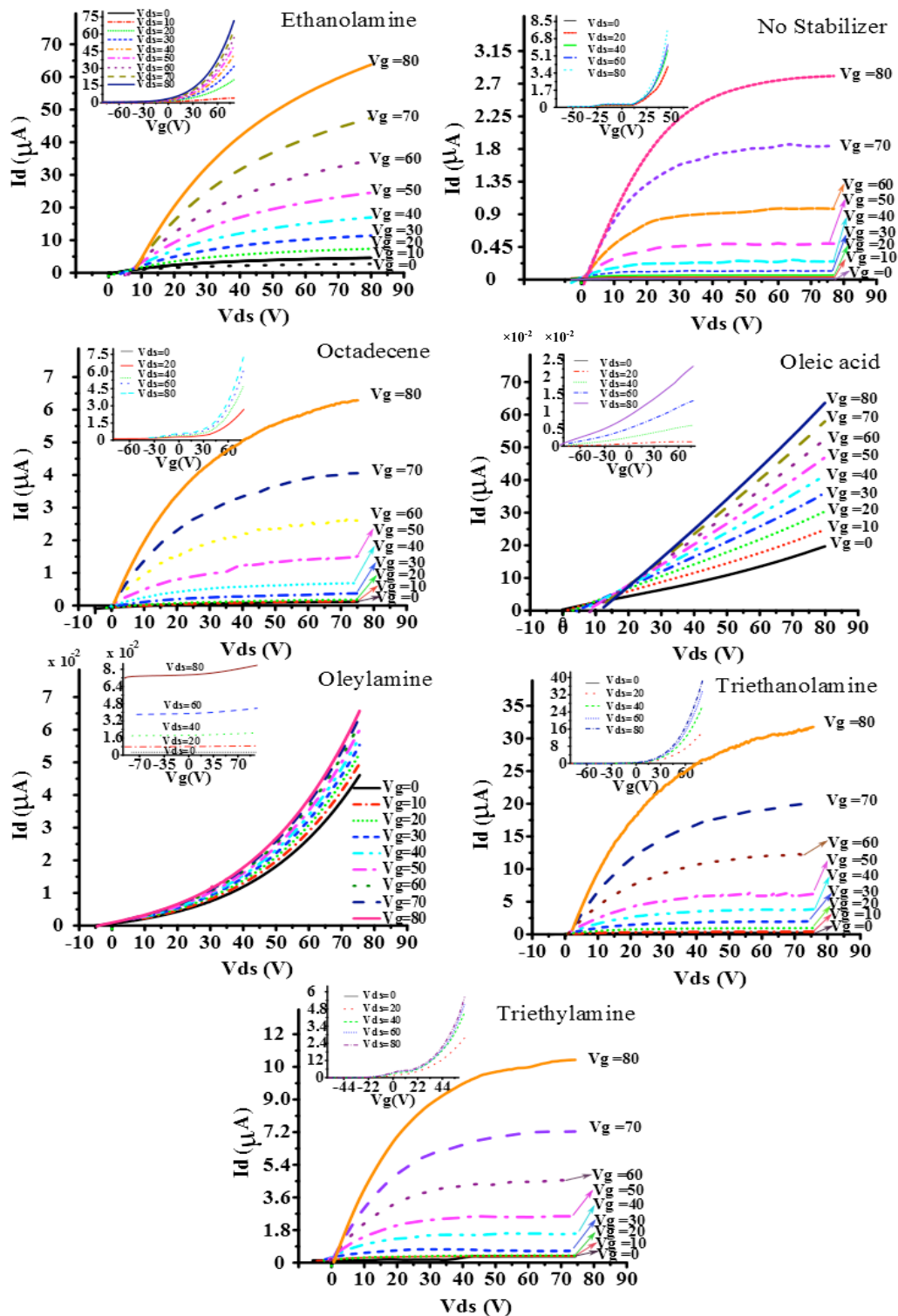
Figure 5-6 Operating characteristics (I_D-V_{DS}) and (insets) transfer characteristics (I_D-V_{GS}) of the TFTs fabricated from ZnO thin films formed using different stabilizers. (Adapted with permission from Ref[229] ;Copyright Royal Society of Chemistry)

121

Further analysis was performed to measure the saturation mobility, threshold voltage and effective mobility. The drain current of the TFT in saturation regime is given by:

$$I_D = \frac{1}{2}\mu_n C_{ox}\left(\frac{W}{L}\right)(V_{GS} - V_{TH})^2 \tag{5-9}$$

Using the slope of the $\sqrt{I_D}$-V_{GS} curve and the intersection of this curve with the x-axis, the saturation mobility and threshold voltage were respectively calculated. The electron saturation field-effect mobility (μ_{sat}) is insensitive to threshold voltage and is less dependent on the contact resistance. However, it describes the pinched-off model where the effective channel length (L_{eff}) of the device is smaller than the actual channel.[2] The polycrystalline nature of ZnO films causes a large number of electron traps to be formed at grain boundaries. Application of a positive gate voltage produces trap filling, thus enhancing the electrical performance of the device. This is not accounted for in the saturation mobility. In order to separate out the effect of gate voltage on the mobility, a parameter known as the effective mobility is used which is defined at low drain voltage as follows:

$$\mu_{eff} = \frac{g_d}{C_{ox}\left(\frac{W}{L}\right)(V_{GS} - V_{TH})} \tag{5-10}$$

The effective mobility (μ_{eff}) takes the variation of mobility due to gate voltage into account. However, the threshold voltage must be known and μ_{eff} shows a higher sensitivity to contact resistance compared to μ_{sat}.[2] In order to overcome the issue of the dependence of effective mobility on the threshold voltage, the field effect mobility (also known as the mobility in the linear region of the operating characteristic) is defined as (at low drain voltage) follows:

$$\mu_{FE} = \frac{g_m}{C_{ox}\left(\frac{W}{L}\right)V_{DS}} \tag{5-11}$$

122

Due to the high dopant density, bulk conduction forms an alternate path for charge transport from source to drain in addition to the channel. Hence the device exhibits a bulk depletion mode regime in addition to the channel accumulation and depletion regimes (similar to gated resistor-type FETs).[180] A clear transition from accumulation to bulk conduction in the form of a plateau region is seen for nearly all the stabilizers used in the I_D-V_{GS} plots (insets in figure 5-6). This bulk current contributes to the leakage current in the off-state of the transistors. The I_D-V_{DS} and I_D-V_{GS} characteristics of such bulk depletion transistors can be used to obtain a wealth of detail regarding the bulk properties of the ZnO. The saturation mobility, effective mobility, field effect mobility, and threshold voltage values for different stabilizers are shown in table 5-9.

As can be seen from the devices, the linear region field effect mobility is surprisingly higher than saturation mobility. This is due to the fact that the saturation mobility, unlike the field effect mobility, ignores the effect of gate voltage. At higher gate voltages, charge carriers fill the traps at the interface hence improving the mobility of the device. The field effect and effective mobility values were measured at V_{GS}=80 V. This high voltage value resulted in filling of traps by carriers, which caused the field effect mobility to be higher than saturation mobility. Ethanolamine, triethanolamine, and triethylamine are stabilizers that show higher mobility values. On the other hand, the discontinuity in oleic acid and oleylamine stabilized ZnO films results in lower mobility values compared to other films.[229] The main limiting factor(s) in charge transport in polycrystalline ZnO films are the grain boundaries. Hence characterizing the grain boundaries can lead to a better understanding of the charge transport in the ZnO films of different stabilizers.

Hossain et al. developed a two dimensional model for modeling the grain boundary effects on the charge transport in ZnO TFTs. Each grain boundary is modeled as a double Schottky barrier in which the barrier height was analyzed as a function density and gate bias. Figure 5-7 shows the model for multiple grain boundaries (dotted lines). It is assumed that all grain boundaries are placed in equal distances. In the case where l_g<2λ (where l_g is the grain size and λ is the decay length of potential for gradual potential) potential barriers overlap each other. Figure 5-7 shows the potential distribution for three

different grain sizes. In all three cases it is assumed $N_d=10^{16}$ cm^{-3} and $N_t=10^{12}$ cm^{-2}. In figure 5-7 (a), the depletion regions

Table 5-9 Extracted parameters from I_D-V_{DS} and I_D-V_{GS} curves of TFTs (W=40 μm, L=20 μm). (Adapted with permission from Ref[229] ;Copyright Royal Society of Chemistry)

Stabilizer	Triethylamine	Triethanolamine	Octadecene	No stabilizer	Oleic acid	Oleylamine	Ethanolamine
Saturation mobility (cm^{2}V^{-1}s^{-1})	0.15	0.4	0.12	0.02	N/A	N/A	0.6
Effective mobility (cm^{2}V^{-1}s^{-1})	0.25	0.7	0.08	0.11	N/A	N/A	0.87
Threshold Voltage V_{th} (V)	1.9	8.7	14.8	9.0	N/A	N/A	-9.1
Field Effect Mobility (cm^{2}V^{-1}s^{-1})	0.33	1.7	0.29	0.05	0.007	0.00002	2.0
Dopant density N_d (cm^{-3})	7.1×10^{16}	7×10^{16}	3.5×10^{16}	9.4×10^{16}	$2.1\times10^{17(*)}$	$6.3\times10^{16(*)}$	4.7×10^{18}
Bulk mobility (cm^{2}V^{-1}s^{-1})	2.1	10	11	23	2.1×10^{-4}	8.1×10^{-4}	7.8×10^{-3}
Inter-grain activation barrier V_b (V)	0.23	0.19	0.22	0.28	0.33	0.46	0.17
Trap density N_t (cm^{-2})	8.0×10^{11}	7.3×10^{11}	5.5×10^{11}	10^{12}	1.6×10^{12}	1.1×10^{12}	5.6×10^{12}

(*) doping values of oleic acid and oleylamine unreliable due to film discontinuity.

associated with different grain boundaries do not overlap with each other. In this case the minimum conduction band energy (activation energy) is equal to qV_n where $V_n=kT/q$ Ln (N_c/n). In this case the condition $N_t(\text{cm}^{-2})\leq N_d(\text{cm}^{-3})$ l_g is valid and the only factor limiting the current is the thermionic emission over the barrier height. In figure 5-7 (b) the grain boundaries are closer to each other resulting in the overlap of depletion regions. The overlapping of the depletion regions lifts up the minimum conduction band from the Fermi level increasing the activation energy to $E_a=E_c-E_f$ (which is higher than qV_n). As a result the concentration of thermally activated carriers becomes smaller. This behavior is observed in the subthreshold region of transfer characteristics of TFTs. Decreasing the grain size as shown in figure 5-7 (c), creates the condition of $N_t(\text{cm}^{-2})\geq N_d(\text{cm}^{-3})$ l_g (cm) causing the depletion region overlap to extend to the entire film resulting in the films to become highly resistive. This behavior corresponds to the off-state of the TFT. Hence it can be concluded that three parameters N_t, N_d, and l_g determine the mode of operation of the TFT.[242]

At high positive gate voltages where the TFT is operating in accumulation mode the potential barrier is calculated as:

$$V_b = \frac{qN_t^2}{8\varepsilon_s N_d} \tag{5-12}$$

The current density through the grain boundary barrier is calculated as:[242]

$$J_{gb} = qv_n n \exp(-\frac{qV_b}{kT})(\exp(\frac{q\Delta V_b}{kT})-1) \tag{5-13}$$

where $v_n=AT^2/qN_C$ is the thermal velocity of electron and ΔV_b is the voltage drop across each grain boundary. If the drain bias is high enough it can be assumed that $q\Delta V_b>>kT$. Thus equation (5-13) can be written as:[242]

$$J_{gb} = qv_n n \exp(-\frac{qV_b}{kT})\exp(\frac{q\Delta V_b}{kT}) \tag{5-14}$$

Assuming n_g grain boundaries in the channel length (L), ΔV_b will be equal to V_{ds}/n_g. The conductivity in the channel with uniform electric can be expressed as:[242]

$$\sigma = \frac{q\upsilon_n nL}{V_{ds}}\exp(-\frac{qV_b}{kT})\exp(\frac{qV_{ds}}{n_g kT})$$ (5-15)

Using the conductivity relationship it can be written:[242]

$$\mu^* = \frac{\upsilon_n L}{V_{ds}}\exp(\frac{qV_{ds}}{n_g kT})\exp(-\frac{qV_b}{kT})$$ (5-16)
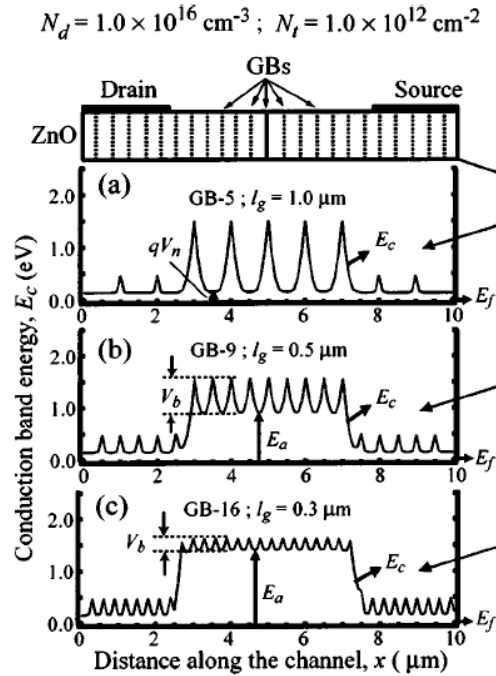
Figure 5-7 Potential values along the surface of ZnO thin film along drain-source electrodes with a) grain size of 1 μm b) grain size of 0.5 μm c) grain size of 0.3 μm. (Adapted with permission from Ref[242]; Copyright American Institute of Physics .)

μ^* is the field effect mobility. Using the field effect mobility value of TFTs, the potential barrier V_b can be calculated using equation (5-16) (at V_g=80 V). Using the doping values

extracted from C-V measurements and the potential barrier values (V_b), the density of trapped charge density at the grain boundary can be calculated using (5-12). The potential barrier (V_b) and the trapped charge density of grain boundaries are shown in table 5-8. As can be seen from values ethanolamine with barrier height of 0.17 V and oleylamine with a barrier height of 0.46 V have the lowest and highest potential barrier height.[229] The trapped charge density for ZnO thin films deposited using various stabilizers are in the same range and correspond to the values previously reported in the literature.[14] In this analysis it is assumed that all the traps are in the grain boundary. Although this assumption is very crude, it is still possible to see the potential profile in the channel. Using this analysis the trapped charge density in the grain boundaries can be calculated without requiring spectroscopic measurements.[242]

5.6 Conclusion

In this chapter, we described the effect of stabilizer on the morphology, electrical, and optical performance of ZnO thin films. The grain size and the preferred orientation of the films were compared using glancing and powder XRD, respectively. Among all the stabilizers, oleic acid resulted in a single (002) crystal orientation, which is the preferred orientation for electrical transport. However, due to the discontinuity of the film the electrical performance of the oleic acid was poor. The photoconductivity of the films deposited using different stabilizers was also studied. Films deposited using different stabilizers exhibited different photoconductive gains and life-times which could be due to the different number of surface states. Measuring the surface area using EIS measurements, it was found that in the case of continuous films, for higher surface area films the photo to dark current ratio and lifetime was larger compared to films with smaller surface area which could be due to the larger number of surface states. Thin film transistors (TFTs) were also fabricated and different parameters like threshold voltage and mobility were measured for various devices. Additionally, using a model developed by Hossain et al the density of trapped charge at the grain boundaries and potential barrier at grain boundaries was calculated and compared for different stabilizers.

6 Summary and Future Work

In this chapter, we summarize the results of the thesis and suggest some potential future work, which can be done to improve the results.

In this thesis, we first introduced solution processed Schottky barrier ZnO TFT. Solution-processed ZnO thin films are attractive as active materials in thin film transistors (TFTs) for low cost electronic device applications. However, the lack of true enhancement mode operation, low mobility and unreliability in transistor characteristics due to the high density of traps and other defects present challenges in using such TFTs in circuits. In this thesis, we demonstrated that the electrical characteristics of such TFTs can be improved by source injection barriers. Asymmetrical Schottky source metal–oxide–semiconductor field-effect transistors (MOSFETs) have been fabricated by utilizing heavily doped solution-processed ZnO as the active layer. $n+$-ZnO was obtained by using triethylamine as the stabilizer in the solution process instead of the more commonly used monoethanolamine. Au was chosen for source metallization to create a Schottky contact to the ZnO and an Al ohmic contact was chosen as the drain. Voltage applied to the gate induced field emission through the Schottky barrier and allowed modulation of the drain current by varying the width of the barrier. By operating the asymmetrical MOSFET when the Schottky contact is reverse biased, effective control over the transistor characteristics was obtained. Due to the unreliable behavior of Au contacts on ZnO, Au contact was replaced by Ag to obtain a better rectifying behavior.

In the next chapter, we described the effect of sol stabilizer on the morphology, crystal orientation, and electrical and optical properties of the deposited ZnO films. The sol stabilizer used in the solution processing of ZnO functions variously as a sol homogenizer, chelating agent, wettability improver and capping agent We examined the effect of six different sol stabilizers -triethylamine, oleylamine, oleic acid, octadecene, triethanolamine and ethanolamine (along with a sol without any stabilizer), on the grain size, crystallographic texture, and resistivity of solution processed ZnO films on thermal oxide-coated silicon substrates, and found large variations in the structural and electrical

properties as a consequence of the choice of sol stabilizer. We found that ZnO films formed using oleic acid as the sol stabilizer possessed a strong (002) preferred orientation with a Lotgering factor as high as 0.86. The key insight we obtained is that the sol stabilizer strongly influences the activation energy barriers for inter-grain transport.

In addition to that, we comprehensively studied the steady state and transient behavior of ZnO films deposited using different stabilizers and compared their lifetime and lifetime – mobility products. When exposed to illumination, the conductivity of the deposited films increased by several orders of magnitude. This is attributed to the trapping of the nonequilibrium holes by the surface oxygen states, which produces equivalent number of excess electrons in the conduction band. Trap-mediated reduction of recombination enables the achievement of very high photoconductive gains in solution-processed ZnO films, pointing to the attractiveness of their use in ultraviolte photodetectors. The ratio of photocurrent to dark current ratio is related to the number of surface states. Hence using EIS measurement the surface area and doping of ZnO thin films were measured. In the case of continuous films, the films with higher surface area exhibit a larger photo to dark current ratio and lifetime. Additionally thin film transistors were fabricated using each of the films. The devices were characterized by measuring some of the parameters like the effective mobility, field effect mobility, saturation mobility and threshold voltage. The main limiting factor for charge transport in poly crystalline ZnO thin films is the grain boundaries. Hence characterizing these grain boundaries is an important step in understanding the charge transport in ZnO thin films. Using the models available in the literature, the trapped charge and the potential barrier of each grain boundary for each film is calculated.

This work has some drawbacks that can be the basis for the further improvements. Doping of ZnO films is one of the ways for improvement of the electrical properties of the films. By doping the ZnO films with the right elements (and right values) the electrical performance of the devices can be enhanced. This will enhance the electrical properties of the ZnO films. Doping of ZnO films can change the carrier concentration of the ZnO thin films. For instance doping the films with Ga reduces the charge carrier

concentration where as indium increases the carrier concentration of the films.[2] Doping of ZnO films with Li has also led to some promising results.[54] The change in the carrier concentration with doping is attributed to changing the concentration of oxygen vacancies, substitution of zinc sites, and occupation of interstitial sites by other metal atoms.

Improving the electrical performance of the fabricated ZnO TFTs is another potential approach. One of the ways of achieving higher performance for the TFTs is by using a different dielectric layer. Increasing the dielectric constant of the gate dielectric results in the filling of the traps by applying a lower voltage to the gate of the transistor. Additionally the expensive vacuum deposition for the gate dielectric can be replaced by the cheap and easy solution processing method, which will increase the throughput. Some of available works in the literature show the considerable improvement of the TFT performance with using the appropriate dielectric layer. For instance TFTs using SiN as the gate dielectric exhibit a better performance compared to the devices using SiO_2.[243] As another example solution processed yttrium oxide as the dielectric layer, improved the electrical performance of ZnO TFTs.[244]

The high annealing temperature used for fabrication of ZnO thin films is another part of the approached used here that requires modification. This high annealing temperature is required for generating crystalline phase and impurity free semiconductor film. This high processing temperatures (400 ^{o}C and above) can be used in depositing ZnO thin films on rigid substrates like glass and silicon. However, this process is incompatible with plastic substrates. Using processes such as electrodeposition and chemical bath deposition with lower annealing temperatures, rendering compatibility with flexible electronics, is another potential constituent of future work.

References:

1.   Adl, A. H.; Ma, A.; Gupta, M.; Benlamri, M.; Tsui, Y. Y.; Barlage, D. W.; Shankar, K., Schottky Barrier Thin Film Transistors Using Solution-Processed n-ZnO. *ACS Appl. Mater. Interfaces* **2012,** *4* (3), 1423-1428.

2.   Fortunato, E.; Barquinha, P.; Martins, R., Oxide Semiconductor Thin-Film Transistors: A Review of Recent Advances. *Adv. Mater.* **2012,** *24* (22), 2945-2986.

3.   Sze, S. M.; Ng, K. K., *Physics of Semiconductor Devices*. Wiley: 2006.

4.   Edgar, L. J., Device for controlling electric current. Google Patents: 1933.

5.   Weimer, P. K., The TFT a new thin-film transistor. *Proceedings of the IRE* **1962,** *50* (6), 1462-1469.

6.   Weimer, P. K., CITATION CLASSIC - THE TFT - A NEW THIN-FILM TRANSISTOR. *Current Contents/Engineering Technology & Applied Sciences* **1983,** (3), 16-16.

7.   Klasens, H. A.; Koelmans, H., A TIN OXIDE FIELD-EFFECT TRANSISTOR. *Solid-State Electron.* **1964,** *7* (9), 701-702.

8.   Boesen, G. F.; Jacobs, J. E., ZNO FIELD-EFFECT TRANSISTOR. *Proceedings of the Institute of Electrical and Electronics Engineers* **1968,** *56* (11), 2094-&.

9.   Aoki, A.; Sasakura, H., TIN OXIDE THIN FILM TRANSISTORS. *Jpn. J. Appl. Phys.* **1970,** *9* (5), 582-&.

10.   Prins, M. W. J.; GrosseHolz, K. O.; Muller, G.; Cillessen, J. F. M.; Giesbers, J. B.; Weening, R. P.; Wolf, R. M., A ferroelectric transparent thin-film transistor. *Applied Physics Letters* **1996,** *68* (25), 3650-3652.

11.   Seager, C. H.; McIntyre, D. C.; Warren, W. L.; Tuttle, B. A., Charge trapping and device behavior in ferroelectric memories. *Applied Physics Letters* **1996,** *68* (19), 2660-2662.

12.   Hoffman, R. L.; Norris, B. J.; Wager, J. F., ZnO-based transparent thin-film transistors. *Applied Physics Letters* **2003,** *82* (5), 733-735.

13.   Masuda, S.; Kitamura, K.; Okumura, Y.; Miyatake, S.; Tabata, H.; Kawai, T., Transparent thin film transistors using ZnO as an active channel layer and their electrical properties. *J. Appl. Phys.* **2003,** *93* (3), 1624-1630.

14.   Carcia, P. F.; McLean, R. S.; Reilly, M. H.; Nunes, G., Transparent ZnO thin-film transistor fabricated by rf magnetron sputtering. *Applied Physics Letters* **2003,** *82* (7), 1117-1119.

15.   Nomura, K.; Ohta, H.; Ueda, K.; Kamiya, T.; Hirano, M.; Hosono, H., Thin-film transistor fabricated in single-crystalline transparent oxide semiconductor. *Science* **2003,** *300* (5623), 1269-1272.

16.   Nomura, K.; Ohta, H.; Takagi, A.; Kamiya, T.; Hirano, M.; Hosono, H., Room-temperature fabrication of transparent flexible thin-film transistors using amorphous oxide semiconductors. *Nature* **2004,** *432* (7016), 488-492.

17.   Chiang, H.; Wager, J.; Hoffman, R.; Jeong, J.; Keszler, D. A., High mobility transparent thin-film transistors with amorphous zinc tin oxide channel layer. *Applied Physics Letters* **2005,** *86* (1), 013503.

18.   Seo, S. J.; Choi, C. G.; Hwang, Y. H.; Bae, B. S., High performance solution-processed amorphous zinc tin oxide thin film transistor. *J. Phys. D-Appl. Phys.* **2009,** *42* (3).

19.   Choi, C. G.; Seo, S. J.; Bae, B. S., Solution-processed indium-zinc oxide transparent thin-film transistors. *Electrochem. Solid State Lett.* **2008,** *11* (1), H7-H9.

20.   Koo, C. Y.; Song, K.; Jun, T.; Kim, D.; Jeong, Y.; Kim, S. H.; Ha, J.; Moon, J., Low Temperature Solution-Processed InZnO Thin-Film Transistors. *J. Electrochem. Soc.* **2010,** *157* (4), J111-J115.

21.   Chen, T. C.; Chang, T. C.; Tsai, C. T.; Hsieh, T. Y.; Chen, S. C.; Lin, C. S.; Hung, M. C.; Tu, C. H.; Chang, J. J.; Chen, P. L., Behaviors of InGaZnO thin film transistor under illuminated positive gate-bias stress. *Applied Physics Letters* **2010,** *97* (11).

22.   Kang, D.; Lim, H.; Kim, C.; Song, I.; Park, J.; Park, Y.; Chung, J., Amorphous gallium indium zinc oxide thin film transistors: Sensitive to oxygen molecules. *Applied Physics Letters* **2007,** *90* (19).

23.   Tickle, A. C., *Thin-film transistors: a new approach to microelectronics*. Wiley: 1969.

24.   Kagan, C. R.; Andry, P., *Thin-film transistors*. CRC Press: 2003.

25.   Street, R. A., *Technology and Applications of Amorphous Silicon*. Springer: 2000.

26.   Zeghbroeck, B. V., Principles of Semiconductor Devices. 2011. http://ecee.colorado.edu/~bart/book/book/title.htm.

27.   Conwell, E.; Weisskopf, V., Theory of impurity scattering in semiconductors. *Physical review* **1950,** *77* (3), 388.

28.   Bardeen, J.; Shockley, W., Deformation potentials and mobilities in non-polar crystals. *Physical review* **1950,** *80* (1), 72.

29.   Nickel, N. H.; Terukov, E., *Zinc Oxide-A Material for Micro-and Optoelectronic Applications: Proceedings of the NATO Advanced Research Workshop on Zinc Oxide as a Material for Micro-and Optoelectronic Applications, held in St. Petersburg, Russia, from 23 to 25 June 2004*. Springer Science & Business Media: 2006; Vol. 194.

30.   Li, F.; Nathan, A.; Wu, Y.; Ong, B. S., *Organic Thin Film Transistor Integration*. Wiley: 2011.

31.   Bao, Z. N., Materials and fabrication needs for low-cost organic transistor circuits. *Adv. Mater.* **2000,** *12* (3), 227-+.

32.   Gurski, J.; Quach, L. M., Display technology overview. *Lytica White Paper* **2005**, 37.

33.   Sun, J.; Mourey, D. A.; Zhao, D. L.; Park, S. K.; Nelson, S. F.; Levy, D. H.; Freeman, D.; Cowdery-Corvan, P.; Tutt, L.; Jackson, T. N., ZnO thin-film transistor ring oscillators with 31-ns propagation delay. *IEEE Electron Device Lett.* **2008,** *29* (7), 721-723.

34.   Kawamura, T.; Wakana, H.; Fujii, K.; Ozaki, H.; Watanabe, K.; Yamazoe, T.; Uchiyama, H.; Torii, K., Oxide TFT Rectifier Achieving 13.56-MHz Wireless Operation. *IEEE Trans. Electron Devices* **2012,** *59* (11), 3002-3008.

35.   Ozaki, H.; Kawamura, T.; Wakana, H.; Yamazoe, T.; Uchiyama, H., Wireless operations for 13.56-MHz band RFID tag using amorphous oxide TFTs. *IEICE Electron. Express* **2011,** *8* (4), 225-231.

36.   Cho, S. H.; Kim, S. W.; Cheong, W. S.; Byun, C. W.; Hwang, C. S.; Cho, K. I.; Bae, B. S., Oxide Thin Film Transistor Circuits for Transparent RFID Applications. *IEICE Trans. Electron.* **2010,** *E93C* (10), 1504-1510.

37.   Fiore, V.; Battiato, P.; Abdinia, S.; Jacobs, S.; Chartier, I.; Coppard, R.; Klink, G.; Cantatore, E.; Ragonese, E.; Palmisano, G., An Integrated 13.56-MHz RFID Tag in a Printed Organic Complementary TFT Technology on Flexible Substrate. *IEEE Trans. Circuits Syst. I-Regul. Pap.* **2015,** *62* (6), 1668-1677.

38.   Jeong, J. K., The status and perspectives of metal oxide thin-film transistors for active matrix flexible displays. *Semicond. Sci. Technol.* **2011,** *26* (3).

39.   Yoo, G.; Lee, H.; Kanicki, J., Electrical Stability of Hexagonal a-Si:H TFTs. *IEEE Electron Device Lett.* **2010,** *31* (1), 53-55.

40.   Lee, J. M.; Cho, I. T.; Lee, J. H.; Kwon, H. I., Bias-stress-induced stretched-exponential time dependence of threshold voltage shift in InGaZnO thin film transistors. *Applied Physics Letters* **2008,** *93* (9).

41.   Street, R. A., Thin-Film Transistors. *Adv. Mater.* **2009,** *21* (20), 2007-2022.

42.   Gleskova, H.; Wagner, S.; Soboyejo, W.; Suo, Z., Electrical response of amorphous silicon thin-film transistors under mechanical strain. *J. Appl. Phys.* **2002,** *92* (10), 6224-6229.

43.   Stewart, M.; Howell, R. S.; Pires, L.; Hatalis, M. K., Polysilicon TFT technology for active matrix OLED displays. *IEEE Trans. Electron Devices* **2001,** *48* (5), 845-851.

44.   Fortunato, G., Polycrystalline silicon thin-film transistors: A continuous evolving technology. *Thin Solid Films* **1997,** *296* (1-2), 82-90.

45.   Pecora, A.; Schillizzi, M.; Tallarida, G.; Fortunato, G.; Reita, C.; Migliorato, P., OFF-CURRENT IN POLYCRYSTALLINE SILICON THIN-FILM TRANSISTORS - AN ANALYSIS OF THE THERMALLY GENERATED COMPONENT. *Solid-State Electron.* **1995,** *38* (4), 845-850.

46.   Brotherton, S. D.; Ayres, J. R.; Young, N. D., CHARACTERIZATION OF LOW-TEMPERATURE POLY-SI THIN-FILM TRANSISTORS. *Solid-State Electron.* **1991,** *34* (7), 671-679.

47.   Kohno, A.; Sameshima, T.; Sano, N.; Sekiya, M.; Hara, M., HIGH-PERFORMANCE POLY-SI TFTS FABRICATED USING PULSED-LASER ANNEALING AND REMOTE PLASMA CVD WITH LOW-TEMPERATURE PROCESSING. *IEEE Trans. Electron Devices* **1995,** *42* (2), 251-257.

48.   Kouvatsos, D. N.; Voutsas, A. T.; Hatalis, M. K., Polycrystalline silicon thin film transistors fabricated in various solid phase crystallized films deposited on glass substrates. *J. Electron. Mater.* **1999,** *28* (1), 19-25.

49.   Pecora, A.; Maiolo, L.; Cuscuna, M.; Simeone, D.; Minotti, A.; Mariucci, L.; Fortunato, G., Low-temperature polysilicon thin film transistors on polyimide substrates for electronics on plastic. *Solid-State Electron.* **2008,** *52* (3), 348-352.

50.   Thompson, M. O.; Galvin, G. J.; Mayer, J. W.; Peercy, P. S.; Poate, J. M.; Jacobson, D. C.; Cullis, A. G.; Chew, N. G., MELTING TEMPERATURE AND EXPLOSIVE CRYSTALLIZATION OF AMORPHOUS-SILICON DURING PULSED LASER IRRADIATION. *Phys. Rev. Lett.* **1984,** *52* (26), 2360-2363.

51.   Kuriyama, H.; Nohda, T.; Aya, Y.; Kuwahara, T.; Wakisaka, K.; Kiyama, S.; Tsuda, S., COMPREHENSIVE STUDY OF LATERAL GRAIN-GROWTH IN POLY-SI FILMS BY EXCIMER-LASER ANNEALING AND ITS APPLICATION TO THIN-FILM TRANSISTORS. *Japanese Journal of Applied Physics Part 1-Regular Papers Short Notes & Review Papers* **1994,** *33* (10), 5657-5662.

52.   Carluccio, R.; Stoemenos, J.; Fortunato, G.; Meakin, D. B.; Bianconi, M., MICROSTRUCTURE OF POLYCRYSTALLINE SILICON FILMS OBTAINED BY COMBINED FURNACE AND LASER ANNEALING. *Applied Physics Letters* **1995,** *66* (11), 1394-1396.

53.   Bayraktaroglu, B.; Leedy, K.; Neidhard, R., Microwave ZnO thin-film transistors. *IEEE Electron Device Lett.* **2008,** *29* (9), 1024-1026.

54.   Adamopoulos, G.; Bashir, A.; Thomas, S.; Gillin, W. P.; Georgakopoulos, S.; Shkunov, M.; Baklar, M. A.; Stingelin, N.; Maher, R. C.; Cohen, L. F.; Bradley, D. D. C.; Anthopoulos, T. D., Spray-Deposited Li-Doped ZnO Transistors with Electron Mobility Exceeding 50 cm(2)/Vs. *Adv. Mater.* **2010,** *22* (42), 4764-+.

55.   Cheng, H. C.; Chen, C. F.; Tsay, C. Y., Transparent ZnO thin film transistor fabricated by sol-gel and chemical bath deposition combination method. *Applied Physics Letters* **2007,** *90* (1).

56.   Han, S. Y.; Herman, G. S.; Chang, C. H., Low-Temperature, High-Performance, Solution-Processed Indium Oxide Thin-Film Transistors. *J. Am. Chem. Soc.* **2011,** *133* (14), 5166-5169.

57.   Choi, C. H.; Han, S. Y.; Su, Y. W.; Fang, Z.; Lin, L. Y.; Cheng, C. C.; Chang, C. H., Fabrication of high-performance, low-temperature solution processed amorphous indium oxide thin-film transistors using a volatile nitrate precursor. *Journal of Materials Chemistry C* **2015,** *3* (4), 854-860.

58.   Hwang, S.; Lee, J. H.; Woo, C. H.; Lee, J. Y.; Cho, H. K., Effect of annealing temperature on the electrical performances of solution-processed InGaZnO thin film transistors. *Thin Solid Films* **2011,** *519* (15), 5146-5149.

59.   Moon, Y. K.; Lee, S.; Kim, W. S.; Kang, B. W.; Jeong, C. O.; Lee, D. H.; Park, J. W., Improvement in the bias stability of amorphous indium gallium zinc oxide thin-film transistors using an O-2 plasma-treated insulator. *Applied Physics Letters* **2009,** *95* (1).

60.   Kim, G. H.; Kim, H. S.; Shin, H. S.; Ahn, B. D.; Kim, K. H.; Kim, H. J., Inkjet-printed InGaZnO thin film transistor. *Thin Solid Films* **2009,** *517* (14), 4007-4010.

61.   Liu, P. T.; Chou, Y. T.; Teng, L. F., Environment-dependent metastability of passivation-free indium zinc oxide thin film transistor after gate bias stress. *Applied Physics Letters* **2009,** *95* (23).

62.   Chong, E.; Jo, K. C.; Lee, S. Y., High stability of amorphous hafnium-indium-zinc-oxide thin film transistor. *Applied Physics Letters* **2010,** *96* (15).

63.   Kim, C. J.; Kim, S.; Lee, J. H.; Park, J. S.; Kim, S.; Park, J.; Lee, E.; Lee, J.; Park, Y.; Kim, J. H.; Shin, S. T.; Chung, U. I., Amorphous hafnium-indium-zinc oxide semiconductor thin film transistors. *Applied Physics Letters* **2009,** *95* (25).

64.   (a) Foo, K. L.; Kashif, M.; Hashim, U.; Ali, M. E., Sol-gel derived ZnO nanoparticulate films for ultraviolet photodetector (UV) applications. *Optik* **2013,** *124* (22), 5373-5376; (b) Hwang, Y. H.; Seo, S. J.; Bae, B. S., Fabrication and characterization of sol-gel-derived zinc oxide thin-film transistor. *J. Mater. Res.* **2010,** *25* (4), 695-700.

65.   Wollenstein, J.; Jagle, M.; Bottner, H., A Gas Sensitive Tin Oxide Thin-Film Transistor. *Advanced Gas Sensing: The Electroadsorptive Effect and Related Techniques* **2003**, 85.

66.   Jang, J.; Kitsomboonloha, R.; Swisher, S. L.; Park, E. S.; Kang, H.; Subramanian, V., Transparent High‑Performance Thin Film Transistors from Solution‑Processed SnO2/ZrO2 Gel‑like Precursors. *Adv. Mater.* **2013,** *25* (7), 1042-1047.

67.   Presley, R.; Munsee, C.; Park, C.; Hong, D.; Wager, J.; Keszler, D., Tin oxide transparent thin-film transistors. *Journal of Physics D: Applied Physics* **2004,** *37* (20), 2810.

68.   Huang, G.; Duan, L.; Dong, G.; Zhang, D.; Qiu, Y., High-Mobility Solution-Processed Tin Oxide Thin-Film Transistors with High-κ Alumina Dielectric Working in Enhancement Mode. *ACS Appl. Mater. Interfaces* **2014,** *6* (23), 20786-20794.

69.   Wang, L.; Yoon, M.-H.; Lu, G.; Yang, Y.; Facchetti, A.; Marks, T. J., High-performance transparent inorganic–organic hybrid thin-film n-type transistors. *Nat. Mater.* **2006,** *5* (11), 893-900.

70.   Liu, A.; Liu, G. X.; Zhu, H. H.; Xu, F.; Fortunato, E.; Martins, R.; Shan, F. K., Fully Solution-Processed Low-Voltage Aqueous In2O3 Thin-Film Transistors Using an Ultrathin ZrO x Dielectric. *ACS Appl. Mater. Interfaces* **2014,** *6* (20), 17364-17369.

71.   Zou, X.; Liu, X.; Wang, C.; Jiang, Y.; Wang, Y.; Xiao, X.; Ho, J. C.; Li, J.; Jiang, C.; Xiong, Q., Controllable electrical properties of metal-doped In2O3 nanowires for high-performance enhancement-mode transistors. *ACS nano* **2012,** *7* (1), 804-810.

72.   Thomas, S. R.; Adamopoulos, G.; Lin, Y.-H.; Faber, H.; Sygellou, L.; Stratakis, E.; Pliatsikas, N.; Patsalas, P. A.; Anthopoulos, T. D., High electron mobility thin-film transistors based on Ga2O3 grown by atmospheric ultrasonic spray pyrolysis at low temperatures. *Applied Physics Letters* **2014,** *105* (9), 092105.

73.   Shin, P. K.; Aya, Y.; Ikegami, T.; Ebihara, K., Application of pulsed laser deposited zinc oxide films to thin film transistor device. *Thin Solid Films* **2008,** *516* (12), 3767-3771.

74.   Ma, A. M.; Gupta, M.; Chowdhury, F. R.; Shen, M.; Bothe, K.; Shankar, K.; Tsui, Y.; Barlage, D. W., Zinc oxide thin film transistors with Schottky source barriers. *Solid-State Electron.* **2012,** *76*, 104-108.

75.   Lim, S. J.; Kwon, S. J.; Kim, H.; Park, J. S., High performance thin film transistor with low temperature atomic layer deposition nitrogen-doped ZnO. *Applied Physics Letters* **2007,** *91* (18).

76.   Carcia, P.; McLean, R.; Reilly, M., High-performance ZnO thin-film transistors on gate dielectrics grown by atomic layer deposition. *Applied Physics Letters* **2006,** *88* (12), 3509.

77.   Navamathavan, R.; Lim, J.; Hwang, D.; Kim, B.; Oh, J.; Yang, J.; Kim, H.; Park, S.; Jang, J., Thin-film transistors based on ZnO fabricated by using radio-frequency magnetron sputtering. *JOURNAL-KOREAN PHYSICAL SOCIETY* **2006,** *48* (2), 271.

78.   Navamathavan, R.; Choi, C. K.; Yang, E.-J.; Lim, J.-H.; Hwang, D.-K.; Park, S.-J., Fabrication and characterizations of ZnO thin film transistors prepared by using radio frequency magnetron sputtering. *Solid-State Electron.* **2008,** *52* (5), 813-816.

79.   Cheng, H.-C.; Chen, C.-F.; Tsay, C.-Y., Transparent ZnO thin film transistor fabricated by sol-gel and chemical bath deposition combination method. *Applied Physics Letters* **2007,** *90* (1), 012113-3.

80.   Fortunato, E. M. C.; Barquinha, P. M. C.; Pimentel, A.; Goncalves, A. M. F.; Marques, A. J. S.; Martins, R. F. P.; Pereira, L. M. N., Wide-bandgap high-mobility ZnO

thin-film transistors produced at room temperature. *Applied Physics Letters* **2004,** *85* (13), 2541-2543.

81.   Levy, D. H.; Freeman, D.; Nelson, S. F.; Cowdery-Corvan, P. J.; Irving, L. M., Stable ZnO thin film transistors by fast open air atomic layer deposition. *Applied Physics Letters* **2008,** *92* (19), 2101.

82.   Lim, S.; Kwon, S.; Kim, H., ZnO thin films prepared by atomic layer deposition and rf sputtering as an active layer for thin film transistor. *Thin Solid Films* **2008,** *516* (7), 1523-1528.

83.   Zhao, J.-L.; Li, X.-M.; Bian, J.-M.; Yu, W.-D.; Gao, X.-D., Structural, optical and electrical properties of ZnO films grown by pulsed laser deposition (PLD). *J. Cryst. Growth* **2005,** *276* (3), 507-512.

84.   Ohyama, M.; Kozuka, H.; Yoko, T., Sol-gel preparation of ZnO films with extremely preferred orientation along (002) plane from zinc acetate solution. *Thin Solid Films* **1997,** *306* (1), 78-85.

85.   Ghosh, R.; Paul, G. K.; Basak, D., Effect of thermal annealing treatment on structural, electrical and optical properties of transparent sol-gel ZnO thin films. *Mater. Res. Bull.* **2005,** *40* (11), 1905-1914.

86.   Lee, J. H.; Ko, K. H.; Park, B. O., Electrical and optical properties of ZnO transparent conducting films by the sol-gel method. *J. Cryst. Growth* **2003,** *247* (1-2), 119-125.

87.   Yaglioglu, B.; Yeom, H.; Beresford, R.; Paine, D., High-mobility amorphous In2O3–10wt% ZnO thin film transistors. *Applied Physics Letters* **2006,** *89* (6), 062103.

88.   Paine, D. C.; Yaglioglu, B.; Beiley, Z.; Lee, S., Amorphous IZO-based transparent thin film transistors. *Thin Solid Films* **2008,** *516* (17), 5894-5898.

89.   Cheng, H.-C.; Tsay, C.-Y., Flexible a-IZO thin film transistors fabricated by solution processes. *Journal of Alloys and Compounds* **2010,** *507* (1), L1-L3.

90.   Jeong, W. H.; Kim, G. H.; Shin, H. S.; Du Ahn, B.; Kim, H. J.; Ryu, M.-K.; Park, K.-B.; Seon, J.-B.; Lee, S. Y., Investigating addition effect of hafnium in InZnO thin film transistors using a solution process. *Applied Physics Letters* **2010,** *96* (9), 093503.

91.   Ebata, K.; Tomai, S.; Tsuruma, Y.; Iitsuka, T.; Matsuzaki, S.; Yano, K., High-Mobility Thin-Film Transistors with Polycrystalline In–Ga–O Channel Fabricated by DC Magnetron Sputtering. *Applied Physics Express* **2012,** *5* (1), 011102.

92.   Gonçalves, G.; Barquinha, P.; Pereira, L.; Franco, N.; Alves, E.; Martins, R.; Fortunato, E., High mobility a-IGO films produced at room temperature and their application in TFTs. *Electrochemical and Solid-State Letters* **2010,** *13* (1), H20-H22.

93.   Park, J. H.; Choi, W. J.; Chae, S. S.; Oh, J. Y.; Lee, S. J.; Song, K. M.; Baik, H. K., Structural and Electrical Properties of Solution-Processed Gallium-Doped Indium Oxide Thin-Film Transistors. *Jpn. J. Appl. Phys.* **2011,** *50* (8R), 080202.

94.   Jeong, S.; Lee, J.-Y.; Lee, S. S.; Choi, Y.; Ryu, B.-H., Impact of metal salt precursor on low-temperature annealed solution-derived Ga-doped In2O3 semiconductor for thin-film transistors. *The Journal of Physical Chemistry C* **2011,** *115* (23), 11773-11780.

95.   McFarlane, B. R.; Kurahashi, P.; Heineck, D. P.; Presley, R. E.; Sundholm, E.; Wager, J. F., AC/DC rectification with indium gallium oxide thin-film transistors. *Electron Device Letters, IEEE* **2010,** *31* (4), 314-316.

96.   Presley, R.; Hong, D.; Chiang, H.; Hung, C.; Hoffman, R.; Wager, J., Transparent ring oscillator based on indium gallium oxide thin-film transistors. *Solid-State Electron.* **2006,** *50* (3), 500-503.

97.   Minami, T.; Takata, S.; Sato, H.; Sonohara, H., Properties of transparent zinc‐stannate conducting films prepared by radio frequency magnetron sputtering. *Journal of Vacuum Science & Technology A* **1995,** *13* (3), 1095-1099.

98.   Perkins, J.; Del Cueto, J.; Alleman, J.; Warmsingh, C.; Keyes, B.; Gedvilas, L.; Parilla, P.; To, B.; Readey, D.; Ginley, D., Combinatorial studies of Zn-Al-O and Zn-Sn-O transparent conducting oxide thin films. *Thin Solid Films* **2002,** *411* (1), 152-160.

99.   Minami, T., Transparent conducting oxide semiconductors for transparent electrodes. *Semicond. Sci. Technol.* **2005,** *20* (4), S35.

100.   Minami, T., Substitution of transparent conducting oxide thin films for indium tin oxide transparent electrode applications. *Thin Solid Films* **2008,** *516* (7), 1314-1321.

101.   Young, D. L.; Moutinho, H.; Yan, Y.; Coutts, T. J., Growth and characterization of radio frequency magnetron sputter-deposited zinc stannate, Zn2SnO4, thin films. *J. Appl. Phys.* **2002,** *92*, 310-319.

102.   Jackson, W.; Hoffman, R.; Herman, G., High-performance flexible zinc tin oxide field-effect transistors. *Applied Physics Letters* **2005,** *87* (19), 193503.

103.   Hong, D.; Chiang, H. Q.; Wager, J. F., Zinc tin oxide thin-film transistors via reactive sputtering using a metal target. *J. Vac. Sci. Technol. B* **2006,** *24* (5), L23-L25.

104.   Chang, Y. J.; Lee, D. H.; Herman, G. S.; Chang, C. H., High-performance, spin-coated zinc tin oxide thin-film transistors. *Electrochem. Solid State Lett.* **2007,** *10* (5), H135-H138.

105.   Jeong, S.; Jeong, Y.; Moon, J., Solution-processed zinc tin oxide semiconductor for thin-film transistors. *The Journal of Physical Chemistry C* **2008,** *112* (30), 11082-11085.

106.   Jeong, Y.; Song, K.; Kim, D.; Koo, C. Y.; Moon, J., Bias stress stability of solution-processed zinc tin oxide thin-film transistors. *J. Electrochem. Soc.* **2009,** *156* (11), H808-H812.

107.   Fung, T. C.; Abe, K.; Kumomi, H.; Kanicki, J., Electrical Instability of RF Sputter Amorphous In-Ga-Zn-O Thin-Film Transistors. *J. Disp. Technol.* **2009,** *5* (12), 452-461.

108.   Yabuta, H.; Sano, M.; Abe, K.; Aiba, T.; Den, T.; Kumomi, H.; Nomura, K.; Kamiya, T.; Hosono, H., High-mobility thin-film transistor with amorphous InGaZnO4 channel fabricated by room temperature rf-magnetron sputtering. *Applied Physics Letters* **2006,** *89* (11).

109.   Lim, J. H.; Shim, J. H.; Choi, J. H.; Joo, J.; Park, K.; Jeon, H.; Moon, M. R.; Jung, D.; Kim, H.; Lee, H. J., Solution-processed InGaZnO-based thin film transistors for printed electronics applications. *Applied Physics Letters* **2009,** *95* (1).

110.   Nayak, P. K.; Busani, T.; Elamurugu, E.; Barquinha, P.; Martins, R.; Hong, Y.; Fortunato, E., Zinc concentration dependence study of solution processed amorphous indium gallium zinc oxide thin film transistors using high-k dielectric. *Applied Physics Letters* **2010,** *97* (18), 183504.

111.   Yang, Y.-H.; Yang, S. S.; Kao, C.-Y.; Chou, K.-S., Chemical and Electrical Properties of Low-Temperature Solution-Processed In–Ga–Zn-O Thin-Film Transistors. *Electron Device Letters, IEEE* **2010,** *31* (4), 329-331.

112. Kim, G. H.; Du Ahn, B.; Shin, H. S.; Jeong, W. H.; Kim, H. J.; Kim, H. J., Effect of indium composition ratio on solution-processed nanocrystalline InGaZnO thin film transistors. *Applied Physics Letters* **2009,** *94* (23), 233501.

113. Kim, Y.-H.; Han, M.-K.; Han, J.-I.; Park, S. K., Effect of metallic composition on electrical properties of solution-processed indium-gallium-zinc-oxide thin-film transistors. *Electron Devices, IEEE Transactions on* **2010,** *57* (5), 1009-1014.

114. Suresh, A.; Muth, J. F., Bias stress stability of indium gallium zinc oxide channel based transparent thin film transistors. *Applied Physics Letters* **2008,** *92* (3).

115. Reese, C.; Roberts, M.; Ling, M. M.; Bao, Z. N., Organic thin film transistors. *Mater. Today* **2004,** *7* (9), 20-27.

116. Braga, D.; Horowitz, G., High-Performance Organic Field-Effect Transistors. *Adv. Mater.* **2009,** *21* (14-15), 1473-1486.

117. Chesterfield, R. J.; Newman, C. R.; Pappenfus, T. M.; Ewbank, P. C.; Haukaas, M. H.; Mann, K. R.; Miller, L. L.; Frisbie, C. D., High electron mobility and ambipolar transport in organic thin-film transistors based on a pi-stacking quinoidal terthiophene. *Adv. Mater.* **2003,** *15* (15), 1278-+.

118. Fukuda, K.; Takeda, Y.; Mizukami, M.; Kumaki, D.; Tokito, S., Fully Solution-Processed Flexible Organic Thin Film Transistor Arrays with High Mobility and Exceptional Uniformity. *Scientific Reports* **2014,** *4*.

119. Dimitrakopoulos, C. D.; Mascaro, D. J., Organic thin-film transistors: A review of recent advances. *IBM J. Res. Dev.* **2001,** *45* (1), 11-27.

120. Karl, N.; Marktanner, J.; Stehle, R.; Warta, W., HIGH-FIELD SATURATION OF CHARGE CARRIER DRIFT VELOCITIES IN ULTRAPURIFIED ORGANIC PHOTOCONDUCTORS. *Synth. Met.* **1991,** *42* (3), 2473-2481.

121. Schoonveld, W. A.; Wildeman, J.; Fichou, D.; Bobbert, P. A.; van Wees, B. J.; Klapwijk, T. M., Coulomb-blockade transport in single-crystal organic thin-film transistors. *Nature* **2000,** *404* (6781), 977-980.

122. Crone, B. K.; Dodabalapur, A.; Sarpeshkar, R.; Filas, R. W.; Lin, Y. Y.; Bao, Z.; O'Neill, J. H.; Li, W.; Katz, H. E., Design and fabrication of organic complementary circuits. *J. Appl. Phys.* **2001,** *89* (9), 5125-5132.

123. Lin, Y. Y.; Dodabalapur, A.; Sarpeshkar, R.; Bao, Z.; Li, W.; Baldwin, K.; Raju, V. R.; Katz, H. E., Organic complementary ring oscillators. *Applied Physics Letters* **1999,** *74* (18), 2714-2716.

124. Crone, B. K.; Dodabalapur, A.; Sarpeshkar, R.; Gelperin, A.; Katz, H. E.; Bao, Z., Organic oscillator and adaptive amplifier circuits for chemical vapor sensing. *J. Appl. Phys.* **2002,** *91* (12), 10140-10146.

125. Ma, L. P.; Liu, J.; Yang, Y., Organic electrical bistable devices and rewritable memory cells. *Applied Physics Letters* **2002,** *80* (16), 2997-2999.

126. Baeg, K. J.; Noh, Y. Y.; Ghim, J.; Kang, S. J.; Lee, H.; Kim, D. Y., Organic non-volatile memory based on pentacene field-effect transistors using a polymeric gate electret. *Adv. Mater.* **2006,** *18* (23), 3179-+.

127. Cantatore, E.; Geuns, T. C. T.; Gelinck, G. H.; van Veenendaal, E.; Gruijthuijsen, A. F. A.; Schrijnemakers, L.; Drews, S.; de Leeuw, D. M., A 13.56-MHz RFID system based on organic transponders. *IEEE J. Solid-State Circuit* **2007,** *42* (1), 84-92.

128. Hoppe, H.; Sariciftci, N. S., Organic solar cells: An overview. *J. Mater. Res.* **2004,** *19* (7), 1924-1945.

129.   Gunes, S.; Neugebauer, H.; Sariciftci, N. S., Conjugated polymer-based organic solar cells. *Chem. Rev.* **2007,** *107* (4), 1324-1338.

130.   Liao, F.; Chen, C.; Subramanian, V., Organic TFTs as gas sensors for electronic nose applications. *Sensors and Actuators B-Chemical* **2005,** *107* (2), 849-855.

131.   Torsi, L.; Dodabalapur, A.; Sabbatini, L.; Zambonin, P. G., Multi-parameter gas sensors based on organic thin-film-transistors. *Sensors and Actuators B-Chemical* **2000,** *67* (3), 312-316.

132.   Gelinck, G. H.; Huitema, H. E. A.; Van Veenendaal, E.; Cantatore, E.; Schrijnemakers, L.; Van der Putten, J.; Geuns, T. C. T.; Beenhakkers, M.; Giesbers, J. B.; Huisman, B. H.; Meijer, E. J.; Benito, E. M.; Touwslager, F. J.; Marsman, A. W.; Van Rens, B. J. E.; De Leeuw, D. M., Flexible active-matrix displays and shift registers based on solution-processed organic transistors. *Nat. Mater.* **2004,** *3* (2), 106-110.

133.   Kumar, B.; Kaushik, B. K.; Negi, Y. S., Perspectives and challenges for organic thin film transistors: materials, devices, processes and applications. *J. Mater. Sci.-Mater. Electron.* **2014,** *25* (1), 1-30.

134.   Horowitz, G., Organic thin film transistors: From theory to real devices. *J. Mater. Res.* **2004,** *19* (7), 1946-1962.

135.   Li, C. S.; Li, Y. N.; Wu, Y. L.; Ong, B. S.; Loutfy, R. O., Fabrication conditions for solution-processed high-mobility ZnO thin-film transistors. *J. Mater. Chem.* **2009,** *19* (11), 1626-1634.

136.   Sharma, B. K.; Khare, N.; Ahmad, S., A ZnO/PEDOT:PSS based inorganic/organic hetrojunction. *Solid State Commun.* **2009,** *149* (19-20), 771-774.

137.   Ong, B. S.; Li, C. S.; Li, Y. N.; Wu, Y. L.; Loutfy, R., Stable, solution-processed, high-mobility ZnO thin-film transistors. *J. Am. Chem. Soc.* **2007,** *129* (10), 2750-+.

138.   El-Shaer, A.; Mofor, A. C.; Bakin, A.; Kreye, M.; Waag, A., High-quality ZnO layers grown by MBE on sapphire. *Superlattices Microstruct.* **2005,** *38* (4-6), 265-271.

139.   Sbrockey, N. M.; Ganesan, S., ZnO thin films by MOCVD. *III-VS Rev.* **2004,** *17* (7), 23-25.

140.   Cruickshank, A. C.; Tay, S. E. R.; Illy, B. N.; Da Campo, R.; Schumann, S.; Jones, T. S.; Heutz, S.; McLachlan, M. A.; McComb, D. W.; Riley, D. J.; Ryan, M. P., Electrodeposition of ZnO Nanostructures on Molecular Thin Films. *Chem. Mat.* **2011,** *23* (17), 3863-3870.

141.   Znaidi, L., Sol-gel-deposited ZnO thin films: A review. *Materials Science and Engineering B-Advanced Functional Solid-State Materials* **2010,** *174* (1-3), 18-30.

142.   Livage, J.; Ganguli, D., Sol-gel electrochromic coatings and devices: A review. *Sol. Energy Mater. Sol. Cells* **2001,** *68* (3-4), 365-381.

143.   Hu, M. Z. C.; Payzant, E. A.; Byers, C. H., Sol-gel and ultrafine particle formation via dielectric tuning of inorganic salt-alcohol-water solutions. *Journal of Colloid and Interface Science* **2000,** *222* (1), 20-36.

144.   Bahadur, H.; Srivastava, A. K.; Sharma, R. K.; Chandra, S., Morphologies of sol-gel derived thin films of ZnO using different precursor materials and their nanostructures. *Nanoscale Res. Lett.* **2007,** *2* (10), 469-475.

145.   (a) Quiñones-Galván, J. G.; Sandoval-Jiménez, I. M.; Tototzintle-Huitle, H.; Hernández-Hernández, L. A.; de Moure-Flores, F.; Hernández-Hernández, A.; Campos-González, E.; Guillén-Cervantes, A.; Zelaya-Angel, O.; Araiza-Ibarra, J. J., Effect of precursor solution and annealing temperature on the physical properties of Sol–Gel-

deposited ZnO thin films. *Results in Physics* **2013,** *3* (0), 248-253; (b) Guglielmi, M.; Carturan, G., PRECURSORS FOR SOL-GEL PREPARATIONS. *J. Non-Cryst. Solids* **1988,** *100* (1-3), 16-30.

146.　Bahnemann, D. W.; Kormann, C.; Hoffmann, M. R., PREPARATION AND CHARACTERIZATION OF QUANTUM SIZE ZINC-OXIDE - A DETAILED SPECTROSCOPIC STUDY. *J. Phys. Chem.* **1987,** *91* (14), 3789-3798.

147.　Bacaksiz, E.; Parlak, M.; Tomakin, M.; Özçelik, A.; Karakız, M.; Altunbaş, M., The effects of zinc nitrate, zinc acetate and zinc chloride precursors on investigation of structural and optical properties of ZnO thin films. *Journal of Alloys and Compounds* **2008,** *466* (1), 447-450.

148.　Armelao, L.; Fabrizio, M.; Gialanella, S.; Zordan, F., Sol-gel synthesis and characterisation of ZnO-based nanosystems. *Thin Solid Films* **2001,** *394* (1-2), 90-96.

149.　Znaidi, L.; Illia, G.; Benyahia, S.; Sanchez, C.; Kanaev, A. V., Oriented ZnO thin films synthesis by sol-gel process for laser application. *Thin Solid Films* **2003,** *428* (1-2), 257-262.

150.　Hosono, E.; Fujihara, S.; Kimura, T.; Imai, H., Non-basic solution routes to prepare ZnO nanoparticles. *Journal of Sol-Gel Science and Technology* **2004,** *29* (2), 71-79.

151.　Sun, D. Z.; Wong, M. H.; Sun, L. Y.; Li, Y. T.; Miyatake, N.; Sue, H. J., Purification and stabilization of colloidal ZnO nanoparticles in methanol. *Journal of Sol-Gel Science and Technology* **2007,** *43* (2), 237-243.

152.　Hu, Z. S.; Oskam, G.; Searson, P. C., Influence of solvent on the growth of ZnO nanoparticles. *Journal of Colloid and Interface Science* **2003,** *263* (2), 454-460.

153.　Znaidi, L.; Illia, G.; Le Guennic, R.; Sanchez, C.; Kanaev, A., Elaboration of ZnO thin films with preferential orientation by a soft chemistry route. *Journal of Sol-Gel Science and Technology* **2003,** *26* (1-3), 817-821.

154.　Raoufi, D.; Raoufi, T., The effect of heat treatment on the physical properties of sol-gel derived ZnO thin films. *Appl. Surf. Sci.* **2009,** *255* (11), 5812-5817.

155.　Chakrabarti, S.; Ganguli, D.; Chaudhuri, S., Substrate dependence of preferred orientation in sol-gel-derived zinc oxide films. *Materials Letters* **2004,** *58* (30), 3952-3957.

156.　Chang, Y. S.; Ting, J. M., Growth of ZnO thin films and whiskers. *Thin Solid Films* **2001,** *398*, 29-34.

157.　Meulenkamp, E. A., Synthesis and growth of ZnO nanoparticles. *J. Phys. Chem. B* **1998,** *102* (29), 5566-5572.

158.　Fujihara, S.; Hosono, E.; Kimura, T., Fabrication of porous metal oxide semiconductor films by a self-template method using layered hydroxide metal acetates. *Journal of Sol-Gel Science and Technology* **2004,** *31* (1-3), 165-168.

159.　Wang, H. H.; Xie, C. S.; Zeng, D. W., Controlled growth of ZnO by adding H2O. *J. Cryst. Growth* **2005,** *277* (1-4), 372-377.

160.　Tokumoto, M. S.; Pulcinelli, S. H.; Santilli, C. V.; Briois, V., Catalysis and temperature dependence on the formation of ZnO nanoparticles and of zinc acetate derivatives prepared by the sol-gel route. *J. Phys. Chem. B* **2003,** *107* (2), 568-574.

161.　Wang, M.; Kim, E. J.; Shin, E. W.; Chung, J. S.; Hahn, S. H.; Park, C., Low-temperature solution growth of high-quality ZnO thin films and solvent-dependent film texture. *The Journal of Physical Chemistry C* **2008,** *112* (6), 1920-1924.

162.	Ohyama, M.; Kozuka, H.; Yoko, T.; Sakka, S., Preparation of ZnO films with preferential orientation by sol-gel method. *Journal of the Ceramic Society of Japan* **1996,** *104* (4), 296-300.

163.	Vajargah, P. H.; Abdizadeh, H.; Ebrahimifard, R.; Golobostanfard, M., Sol–gel derived ZnO thin films: effect of amino-additives. *Appl. Surf. Sci.* **2013,** *285*, 732-743.

164.	Kim, Y. S.; Tai, W. P.; Shu, S. J., Effect of preheating temperature on structural and optical properties of ZnO thin films by sol-gel process. *Thin Solid Films* **2005,** *491* (1-2), 153-160.

165.	O'Brien, S.; Koh, L. H. K.; Crean, G. M., ZnO thin films prepared by a single step sol-gel process. *Thin Solid Films* **2008,** *516* (7), 1391-1395.

166.	Li, Y.; Xu, L.; Li, X.; Shen, X.; Wang, A., Effect of aging time of ZnO sol on the structural and optical properties of ZnO thin films prepared by sol–gel method. *Appl. Surf. Sci.* **2010,** *256* (14), 4543-4547.

167.	Fatollahi, V.; Amini, M. M., Sol–gel preparation of highly oriented gallium-doped zinc oxide thin films. *Materials Letters* **2001,** *50* (4), 235-239.

168.	Habibi, M. H.; Sardashti, M. K., Structure and Morphology of Nanostructured Zinc Oxide Thin Films Prepared by Dip- vs. Spin-Coating Methods. *Journal of the Iranian Chemical Society* **2008,** *5* (4), 603-609.

169.	Mridha, S.; Basak, D., Effect of thickness on the structural, electrical and optical properties of ZnO films. *Mater. Res. Bull.* **2007,** *42* (5), 875-882.

170.	Ohyama, M.; Kouzuka, H.; Yoko, T., Sol-gel preparation of ZnO films with extremely preferred orientation along (002) plane from zinc acetate solution. *Thin Solid Films* **1997,** *306* (1), 78-85.

171.	Wang, M. R.; Wang, J.; Chen, W.; Cui, Y.; Wang, L. D., Effect of preheating and annealing temperatures on quality characteristics of ZnO thin film prepared by sol-gel method. *Materials Chemistry and Physics* **2006,** *97* (2-3), 219-225.

172.	Bagnall, D.; Chen, Y.; Zhu, Z.; Yao, T.; Koyama, S.; Shen, M. Y.; Goto, T., Optically pumped lasing of ZnO at room temperature. *Applied Physics Letters* **1997,** *70* (17), 2230-2232.

173.	Tang, Z.; Wong, G. K.; Yu, P.; Kawasaki, M.; Ohtomo, A.; Koinuma, H.; Segawa, Y., Room-temperature ultraviolet laser emission from self-assembled ZnO microcrystallite thin films. *Applied Physics Letters* **1998,** *72* (25), 3270-3272.

174.	Bagnall, D.; Chen, Y.; Shen, M.; Zhu, Z.; Goto, T.; Yao, T., Room temperature excitonic stimulated emission from zinc oxide epilayers grown by plasma-assisted MBE. *J. Cryst. Growth* **1998,** *184*, 605-609.

175.	Segawa, Y.; Ohtomo, A.; Kawasaki, M.; Koinuma, H.; Tang, Z.; Yu, P.; Wong, G., Growth of ZnO thin film by laser MBE: lasing of exciton at room temperature. *physica status solidi (b)* **1997,** *202* (2), 669-672.

176.	Su, B.-Y.; Su, Y.-K.; Tseng, Z.-L.; Shih, M.-F.; Cheng, C.-Y.; Wu, T.-H.; Wu, C.-S.; Yeh, J.-J.; Ho, P.-Y.; Juang, Y.-D., Antireflective and radiation resistant ZnO thin films for the efficiency enhancement of GaAs photovoltaics. *J. Electrochem. Soc.* **2011,** *158* (3), H267-H270.

177.	Norris, B. J.; Anderson, J.; Wager, J. F.; Keszler, D. A., Spin-coated zinc oxide transparent transistors. *J. Phys. D-Appl. Phys.* **2003,** *36* (20), L105-L107.

178.   Hadimioglu, B.; La Comb Jr, L.; Wright, D.; Khuri‑Yakub, B.; Quate, C., High efficiency, multiple layer ZnO acoustic transducers at millimeter‑wave frequencies. *Applied Physics Letters* **1987,** *50* (23), 1642-1644.

179.   Gorla, C.; Emanetoglu, N.; Liang, S.; Mayo, W.; Lu, Y.; Wraback, M.; Shen, H., Structural, optical, and surface acoustic wave properties of epitaxial ZnO films grown on (0112) sapphire by metalorganic chemical vapor deposition. *J. Appl. Phys.* **1999,** *85* (5), 2595-2602.

180.   Goldberger, J.; Sirbuly, D. J.; Law, M.; Yang, P., ZnO nanowire transistors. *The Journal of Physical Chemistry B* **2005,** *109* (1), 9-14.

181.   Heo, Y.; Tien, L.; Kwon, Y.; Norton, D.; Pearton, S.; Kang, B.; Ren, F., Depletion-mode ZnO nanowire field-effect transistor. *Applied Physics Letters* **2004,** *85* (12), 2274-2276.

182.   Heo, Y.; Tien, L.; Norton, D.; Pearton, S.; Kang, B.; Ren, F.; LaRoche, J., Pt∕ZnO nanowire Schottky diodes. *Applied Physics Letters* **2004,** *85* (15), 3107-3109.

183.   Lao, C. S.; Liu, J.; Gao, P.; Zhang, L.; Davidovic, D.; Tummala, R.; Wang, Z. L., ZnO nanobelt/nanowire Schottky diodes formed by dielectrophoresis alignment across Au electrodes. *Nano Lett.* **2006,** *6* (2), 263-266.

184.   Kim, D. C.; Jung, B. O.; Kwon, Y. H.; Cho, H. K., Highly Sensible ZnO Nanowire Ultraviolet Photodetectors Based on Mechanical Schottky Contact. *J. Electrochem. Soc.* **2012,** *159* (1), K10-K14.

185.   Hwang, D.-K.; Kang, S.-H.; Lim, J.-H.; Yang, E.-J.; Oh, J.-Y.; Yang, J.-H.; Park, S.-J., p-ZnO/n-GaN heterostructure ZnO light-emitting diodes. *Applied Physics Letters* **2005,** *86* (22), 222101-222101.

186.   Jiao, S.; Zhang, Z.; Lu, Y.; Shen, D.; Yao, B.; Zhang, J.; Li, B.; Zhao, D.; Fan, X.; Tang, Z., ZnO pn junction light-emitting diodes fabricated on sapphire substrates. *Applied Physics Letters* **2006,** *88* (3), 031911.

187.   Repins, I.; Contreras, M. A.; Egaas, B.; DeHart, C.; Scharf, J.; Perkins, C. L.; To, B.; Noufi, R., 19·9%‑efficient ZnO/CdS/CuInGaSe2 solar cell with 81·2% fill factor. *Progress in Photovoltaics: Research and applications* **2008,** *16* (3), 235-239.

188.   Katayama, J.; Ito, K.; Matsuoka, M.; Tamaki, J., Performance of Cu2O/ZnO solar cell prepared by two-step electrodeposition. *Journal of Applied Electrochemistry* **2004,** *34* (7), 687-692.

189.   Wan, Q.; Li, Q. H.; Chen, Y. J.; Wang, T. H.; He, X. L.; Li, J. P.; Lin, C. L., Fabrication and ethanol sensing characteristics of ZnO nanowire gas sensors. *Applied Physics Letters* **2004,** *84* (18), 3654-3656.

190.   Özgür, Ü.; Hofstetter, D.; Morkoç, H., ZnO devices and applications: a review of current status and future prospects. *Proc. IEEE* **2010,** *98* (7), 1255-1268.

191.   Liu, K.; Sakurai, M.; Aono, M., ZnO-based ultraviolet photodetectors. *Sensors* **2010,** *10* (9), 8604-8634.

192.   Moon, T.-H.; Jeong, M.-C.; Lee, W.; Myoung, J.-M., The fabrication and characterization of ZnO UV detector. *Appl. Surf. Sci.* **2005,** *240* (1), 280-285.

193.   Liang, S.; Sheng, H.; Liu, Y.; Huo, Z.; Lu, Y.; Shen, H., ZnO Schottky ultraviolet photodetectors. *J. Cryst. Growth* **2001,** *225* (2), 110-113.

194.   Cao, B.; Matsumoto, T.; Matsumoto, M.; Higashihata, M.; Nakamura, D.; Okada, T., ZnO nanowalls grown with high-pressure PLD and their applications as field emitters and UV detectors. *The Journal of Physical Chemistry C* **2009,** *113* (25), 10975-10980.

195.   Jiang, D.; Zhang, J.; Lu, Y.; Liu, K.; Zhao, D.; Zhang, Z.; Shen, D.; Fan, X., Ultraviolet Schottky detector based on epitaxial ZnO thin film. *Solid-State Electron.* **2008,** *52* (5), 679-682.

196.   Lin, T.; Chang, S.-J.; Su, Y.-K.; Huang, B.; Fujita, M.; Horikoshi, Y., ZnO MSM photodetectors with Ru contact electrodes. *J. Cryst. Growth* **2005,** *281* (2), 513-517.

197.   Basak, D.; Amin, G.; Mallik, B.; Paul, G.; Sen, S., Photoconductive UV detectors on sol–gel-synthesized ZnO films. *J. Cryst. Growth* **2003,** *256* (1), 73-77.

198.   Jin, Y.; Wang, J.; Sun, B.; Blakesley, J. C.; Greenham, N. C., Solution-processed ultraviolet photodetectors based on colloidal ZnO nanoparticles. *Nano Lett.* **2008,** *8* (6), 1649-1653.

199.   Ahn, S. E.; Lee, J. S.; Kim, H.; Kim, S.; Kang, B. H.; Kim, K. H.; Kim, G. T., Photoresponse of sol-gel-synthesized ZnO nanorods. *Applied Physics Letters* **2004,** *84* (24), 5022-5024.

200.   Vanheusden, K.; Warren, W.; Seager, C.; Tallant, D.; Voigt, J.; Gnade, B., Mechanisms behind green photoluminescence in ZnO phosphor powders. *J. Appl. Phys.* **1996,** *79* (10), 7983-7990.

201.   Feng, X.; Feng, L.; Jin, M.; Zhai, J.; Jiang, L.; Zhu, D., Reversible super-hydrophobicity to super-hydrophilicity transition of aligned ZnO nanorod films. *J. Am. Chem. Soc.* **2004,** *126* (1), 62-63.

202.   Shan, C.; Zhang, J.; Yao, B.; Shen, D.; Fan, X.; Choy, K., Ultraviolet photodetector fabricated from atomic-layer-deposited ZnO films. *J. Vac. Sci. Technol. B* **2009,** *27* (3), 1765-1768.

203.   (a) Look, D. C., Recent advances in ZnO materials and devices. *Materials Science and Engineering: B* **2001,** *80* (1-3), 383-387; (b) Brillson, L. J.; Lu, Y. C., ZnO Schottky barriers and Ohmic contacts. *J. Appl. Phys.* **2011,** *109* (12); (c) Anderson, J.; Chris, G. V. d. W., Fundamentals of zinc oxide as a semiconductor. *Reports on Progress in Physics* **2009,** *72* (12), 126501.

204.   (a) Ryu, Y.; Lee, T.-S.; Lubguban, J. A.; White, H. W.; Kim, B.-J.; Park, Y.-S.; Youn, C.-J., Next generation of oxide photonic devices: ZnO-based ultraviolet light emitting diodes. *Applied Physics Letters* **2006,** *88* (24), 241108-3; (b) Wolff, K.; Hilleringmann, U., Solution processed inverter based on zinc oxide nanoparticle thin-film transistors with poly(4-vinylphenol) gate dielectric. *Solid-State Electronics* **2011,** *62* (1), 110-114.

205.   (a) Sun, B.; Sirringhaus, H., Solution-Processed Zinc Oxide Field-Effect Transistors Based on Self-Assembly of Colloidal Nanorods. *Nano Letters* **2005,** *5* (12), 2408-2413; (b) Mourey, D. A.; Park, S. K.; Zhao, D. L. A.; Sun, J.; Li, Y. Y. V.; Subramanian, S.; Nelson, S. F.; Levy, D. H.; Anthony, J. E.; Jackson, T. N., Fast, simple ZnO/organic CMOS integrated circuits. *Org. Electron.* **2009,** *10* (8), 1632-1635.

206.   Ozgur, U.; Hofstetter, D.; Morkoc, H., ZnO Devices and Applications: A Review of Current Status and Future Prospects. *Proc. IEEE* **2010,** *98* (7), 1255-1268.

207.   (a) Park, J. S.; Jeong, J. K.; Mo, Y. G.; Kim, H. D.; Kim, C. J., Control of threshold voltage in ZnO-based oxide thin film transistors. *Applied Physics Letters* **2008,** *93* (3); (b) Moon, Y. K.; Moon, D. Y.; Lee, S.; Park, J. W., Enhancement of ZnO thin film transistor performance by high-dose proton irradiation. *Nucl. Instrum. Methods Phys. Res. Sect. B-Beam Interact. Mater. Atoms* **2010,** *268* (16), 2522-2526; (c) Park, J. S., The annealing effect on properties of ZnO thin film transistors with Ti/Pt source-drain

contact. *J. Electroceram.* **2010,** *25* (2-4), 145-149; (d) Remashan, K.; Choi, Y. S.; Park, S. J.; Jang, J. H., Improved Characteristics of Metal Organic Chemical Vapor Deposition-Grown ZnO Thin-Film Transistors by Controlling VI/II Ratio of ZnO Film Growth and Using a Modified Thin-Film Transistor Layer Structure. *Japanese Journal of Applied Physics* **2011,** *50* (4); (e) Trinh, T. T.; Nguyen, V. D.; Ryu, K.; Jang, K.; Lee, W.; Baek, S.; Raja, J.; Yi, J., Improvement in the performance of an InGaZnO thin-film transistor by controlling interface trap densities between the insulator and active layer. *Semicond. Sci. Technol.* **2011,** *26* (8).

208.   Shannon, J. M.; Balon, F., Source-gated thin-film transistors. *Solid-State Electron.* **2008,** *52* (3), 449-454.

209.   Jhaveri, R.; Nagavarapu, V.; Woo, J. C. S., Asymmetric Schottky Tunneling Source SOI MOSFET Design for Mixed-Mode Applications. *IEEE Trans. Electron Devices* **2009,** *56* (1), 93-99.

210.   Shannon, J. M.; Gerstner, E. G., Source-gated thin-film transistors. *IEEE Electron Device Lett.* **2003,** *24* (6), 405-407.

211.   Kanicki, J., *Amorphous and Microcrystalline Semiconductor Devices: Materials and device physics*. Artech House: 1992.

212.   Shannon, J. M.; Balon, F., High-performance thin-film transistors in disordered and poor-quality semiconductors. *Electron Devices, IEEE Transactions on* **2007,** *54* (2), 354-358.

213.   Shannon, J.; Gerstner, E., Source-gated transistors in hydrogenated amorphous silicon. *Solid-State Electron.* **2004,** *48* (7), 1155-1161.

214.   Sporea, R. A.; Guo, X.; Shannon, J. M.; Silva, S. R. P., Source-Gated Transistors for Versatile Large Area Electronic Circuit Design and Fabrication. In *2011 International Conference on Semiconductor Technology for Ultra Large Scale Integrated Circuits and Thin Film Transistors*, Kuo, Y.; Bersuker, G., Eds. 2011; Vol. 37, pp 57-63.

215.   Dahiya, A. S.; Opoku, C.; Sporea, R. A.; Sarvankumar, B.; Poulin-Vittrant, G.; Cayrel, F.; Camara, N.; Alquier, D., Single-crystalline ZnO sheet Source-Gated Transistors. *Scientific Reports* **2016,** *6*.

216.   Shannon, J. M.; Balon, F., Frequency response of source-gated transistors. *IEEE Trans. Electron Devices* **2009,** *56* (10), 2354-2356.

217.   Sporea, R. A.; Guo, X. J.; Shannon, J. M.; Silva, S. R. P.; Ieee, EFFECTS OF PROCESS VARIATIONS ON THE CURRENT IN SCHOTTKY BARRIER SOURCE-GATED TRANSISTORS. In *Cas: 2009 International Semiconductor Conference, Vols 1 and 2, Proceedings*, Ieee: New York, 2009; pp 413-416.

218.   Srinivasan, G.; Gopalakrishnan, N.; Yu, Y. S.; Kesavamoorthy, R.; Kumar, J., Influence of post-deposition annealing on the structural and optical properties of ZnO thin films prepared by sol-gel and spin-coating method. *Superlattices Microstruct.* **2008,** *43* (2), 112-119.

219.   Dutta, M.; Mridha, S.; Basak, D., Effect of sol concentration on the properties of ZnO thin films prepared by sol-gel technique. *Appl. Surf. Sci.* **2008,** *254* (9), 2743-2747.

220.   Jones, A. C.; Wright, P. J.; Cockayne, B., PRECURSORS FOR II-VI SEMICONDUCTORS - REQUIREMENTS AND DEVELOPMENTS. *J. Cryst. Growth* **1991,** *107* (1-4), 297-308.

221. Yoon, S. H.; Liu, D.; Shen, D. N.; Park, M.; Kim, D. J., Effect of chelating agents on the preferred orientation of ZnO films by sol-gel process. *J. Mater. Sci.* **2008,** *43* (18), 6177-6181.

222. Frenzel, H.; Lajn, A.; Brandt, M.; von Wenckstern, H.; Biehne, G.; Hochmuth, H.; Lorenz, M.; Grundmann, M., ZnO metal-semiconductor field-effect transistors with Ag-Schottky gates. *Applied Physics Letters* **2008,** *92* (19).

223. Park, J.; Ozbek, A. M.; Ma, L.; Veety, M. T.; Morgensen, M. P.; Barlage, D. W.; Wheeler, V. D.; Johnson, M. A. L., An analytical model of source injection for N-type enhancement mode GaN-based Schottky Source/Drain MOSFET's with experimental demonstration. *Solid-State Electron.* **2010,** *54* (12), 1680-1685.

224. Redinger, D. H., Lifetime Modeling of ZnO Thin-Film Transistors. *IEEE Trans. Electron Devices* **2010,** *57* (12), 3460-3465.

225. Wang, C.; Snyder, J. P.; Tucker, J. R., Sub-40 nm PtSi Schottky source/drain metal-oxide-semiconductor field-effect transistors. *Applied Physics Letters* **1999,** *74* (8), 1174-1176.

226. Hong, K.; Lee, J. L., Inverted top-emitting organic light-emitting diodes using transparent silver oxide anode formed by oxygen plasma. *Electrochem. Solid State Lett.* **2008,** *11* (2), H29-H31.

227. Adl, A. H.; Farsinezhad, S.; Ma, A.; Barlage, D. W.; Shankar, K. In *High Performance Zinc Oxide Thin Film Transistors Through Improved Material Processing and Device Design*, ASME 2014 International Mechanical Engineering Congress and Exposition, American Society of Mechanical Engineers: 2014; pp V02BT02A042-V02BT02A042.

228. Govender, K.; Boyle, D. S.; Kenway, P. B.; O'Brien, P., Understanding the factors that govern the deposition and morphology of thin films of ZnO from aqueous solution. *J. Mater. Chem.* **2004,** *14* (16), 2575-2591.

229. Adl, A. H.; Kar, P.; Farsinezhad, S.; Sharma, H.; Shankar, K., Effect of sol stabilizer on the structure and electronic properties of solution-processed ZnO thin films. *RSC Adv.* **2015,** *5* (106), 87007-87018.

230. Yahia, S. B.; Znaidi, L.; Kanaev, A.; Petitet, J. P., Raman study of oriented ZnO thin films deposited by sol-gel method. *Spectrochimica acta. Part A, Molecular and biomolecular spectroscopy* **2008,** *71* (4), 1234-8.

231. Yang, M. M.; Crerar, D. A.; Irish, D. E., A RAMAN-SPECTROSCOPIC STUDY OF LEAD AND ZINC ACETATE COMPLEXES IN HYDROTHERMAL SOLUTIONS. *Geochim. Cosmochim. Acta* **1989,** *53* (2), 319-326.

232. Alim, K. A.; Fonoberov, V. A.; Shamsa, M.; Balandin, A. A., Micro-Raman investigation of optical phonons in ZnO nanocrystals. *J. Appl. Phys.* **2005,** *97* (12).

233. Furushima, R.; Tanaka, S.; Kato, Z.; Uematsu, K., Orientation distribution-Lotgering factor relationship in a polycrystalline material-as an example of bismuth titanate prepared by a magnetic field. *Journal of the Ceramic Society of Japan* **2010,** *118* (1382), 921-926.

234. (a) Sagar, P.; Shishodia, P. K.; Mehra, R. M., Influence of pH value on the quality of sol-gel derived ZnO films. *Appl. Surf. Sci.* **2007,** *253* (12), 5419-5424; (b) Jun, T.; Jung, Y.; Song, K.; Moon, J., Influences of pH and Ligand Type on the Performance of Inorganic Aqueous Precursor-Derived ZnO Thin Film Transistors. *ACS Appl. Mater. Interfaces* **2011,** *3* (3), 774-781.

235.   Ghosh, T.; Basak, D., Highly efficient ultraviolet photodetection in nanocolumnar RF sputtered ZnO films: a comparison between sputtered, sol-gel and aqueous chemically grown nanostructures. *Nanotechnology* **2010,** *21* (37).

236.   Heo, Y. W.; Norton, D. P.; Pearton, S. J., Origin of green luminescence in ZnO thin film grown by molecular-beam epitaxy. *J. Appl. Phys.* **2005,** *98* (7).

237.   Hsu, H. C.; Cheng, C. S.; Chang, C. C.; Yang, S.; Chang, C. S.; Hsieh, W. F., Orientation-enhanced growth and optical properties of ZnO nanowires grown on porous silicon substrates. *Nanotechnology* **2005,** *16* (2), 297-301.

238.   (a) Yasutaka, T.; Masaaki, K.; Akiko, K.; Hideki, M.; Yutaka, O., Photoconductivity of Ultrathin Zinc Oxide Films. *Japanese Journal of Applied Physics* **1994,** *33* (12R), 6611; (b) Studenikin, S. A.; Golego, N.; Cocivera, M., Density of band-gap traps in polycrystalline films from photoconductivity transients using an improved Laplace transform method. *Journal of Applied Physics* **1998,** *84* (9), 5001-5004; (c) Soci, C.; Zhang, A.; Xiang, B.; Dayeh, S. A.; Aplin, D. P. R.; Park, J.; Bao, X. Y.; Lo, Y. H.; Wang, D., ZnO Nanowire UV Photodetectors with High Internal Gain. *Nano Letters* **2007,** *7* (4), 1003-1009.

239.   Liu, K. W.; Ma, J. G.; Zhang, J. Y.; Lu, Y. M.; Jiang, D. Y.; Li, B. H.; Zhao, D. X.; Zhang, Z. Z.; Yao, B.; Shen, D. Z., Ultraviolet photoconductive detector with high visible rejection and fast photoresponse based on ZnO thin film. *Solid-State Electronics* **2007,** *51* (5), 757-761.

240.   Hirschorn, B.; Orazem, M. E.; Tribollet, B.; Vivier, V.; Frateur, I.; Musiani, M., Determination of effective capacitance and film thickness from constant-phase-element parameters. *Electrochim. Acta* **2010,** *55* (21), 6218-6227.

241.   Blackwood, D. J., Influence of the space-charge region on electrochemical impedance measurements on passive oxide films on titanium. *Electrochim. Acta* **2000,** *46* (4), 563-569.

242.   Hossain, F. M.; Nishii, J.; Takagi, S.; Ohtomo, A.; Fukumura, T.; Fujioka, H.; Ohno, H.; Koinuma, H.; Kawasaki, M., Modeling and simulation of polycrystalline ZnO thin-film transistors. *J. Appl. Phys.* **2003,** *94* (12), 7768-7777.

243.   Cross, R. B. M.; De Souza, M. M.; Deane, S. C.; Young, N. D., A comparison of the performance and stability of ZnO-TFTs with silicon dioxide and nitride as gate insulators. *IEEE Trans. Electron Devices* **2008,** *55* (5), 1109-1115.

244.   Song, K.; Yang, W.; Jung, Y.; Jeong, S.; Moon, J., A solution-processed yttrium oxide gate insulator for high-performance all-solution-processed fully transparent thin film transistors. *J. Mater. Chem.* **2012,** *22* (39), 21265-21271.

245.   Sun, L.; Shao, R.; Chen, Z.; Tang, L.; Dai, Y.; Ding, J., Alkali-dependent synthesis of flower-like ZnO structures with enhanced photocatalytic activity via a facile hydrothermal method. *Appl. Surf. Sci.* **2012,** *258* (14), 5455-5461.

246.   Hsieh, C. H., Spherical zinc oxide nano particles from zinc acetate in the precipitation method. *Journal of the Chinese Chemical Society* **2007,** *54* (1), 31-34.

247.   Kaneva, N.; Dushkin, C.; Bojinova, A., ZnO thin films preparation on glass substrates by two different sol-gel methods. *Bulgarian Chemical Communication* **2012,** *44*, 261-267.

248.   Kamalasanan, M.; Chandra, S., Sol-gel synthesis of ZnO thin films. *Thin Solid Films* **1996,** *288* (1), 112-115.

249.   Shokuhfar, A.; Samei, J.; Esmaielzadeh Kandjani, A.; Vaezi, M. R. In *Synthesis of ZnO Nanoparticles via Sol-Gel Process Using Triethanolamine as a Novel Surfactant*, Defect and Diffusion Forum, Trans Tech Publ: 2008; pp 626-631.

250.   Salavati-Niasari, M.; Davar, F.; Mazaheri, M., Preparation of ZnO nanoparticles from [bis (acetylacetonato) zinc (II)]–oleylamine complex by thermal decomposition. *Materials Letters* **2008,** *62* (12), 1890-1892.

251.   Zhang, Z.; Liu, S.; Chow, S.; Han, M.-Y., Modulation of the morphology of ZnO nanostructures via aminolytic reaction: from nanorods to nanosquamas. *Langmuir* **2006,** *22* (14), 6335-6340.

252.   Fu, Y.-S.; Du, X.-W.; Kulinich, S. A.; Qiu, J.-S.; Qin, W.-J.; Li, R.; Sun, J.; Liu, J., Stable aqueous dispersion of ZnO quantum dots with strong blue emission via simple solution route. *J. Am. Chem. Soc.* **2007,** *129* (51), 16029-16033.

253.   Fu, Y.; Song, Y.; Kulinich, S.; Sun, J.; Liu, J.; Du, X., Single-crystal ZnO flocky sphere formed by three-dimensional oriented attachment of nanoparticles. *Journal of Physics and Chemistry of Solids* **2008,** *69* (4), 880-883.

254.   Turgeman, R.; Tirosh, S.; Gedanken, A., Growing ZnO crystals on magnetite nanoparticles. *Chemistry-A European Journal* **2004,** *10* (7), 1845-1850.

255.   Wang, F.; Wang, X., Mechanisms in the solution growth of free-standing two-dimensional inorganic nanomaterials. *Nanoscale* **2014,** *6* (12), 6398-6414.

256.   Nguyen, T.-D.; Do, T.-O., *Size-and shape-controlled synthesis of monodisperse metal oxide and mixed oxide nanocrystals*. INTECH Open Access Publisher: 2011.

257.   Andelman, T.; Gong, Y.; Polking, M.; Yin, M.; Kuskovsky, I.; Neumark, G.; O'Brien, S., Morphological control and photoluminescence of zinc oxide nanocrystals. *The Journal of Physical Chemistry B* **2005,** *109* (30), 14314-14318.

258.   Nyquist, R. A.; Kagel, R. O., *Handbook of infrared and raman spectra of inorganic compounds and organic salts: infrared spectra of inorganic compounds*. Academic press: 2012; Vol. 4.

259.   Zhang, L.; Yin, L.; Wang, C.; Lun, N.; Qi, Y., Sol− Gel Growth of hexagonal faceted ZnO prism quantum dots with polar surfaces for enhanced photocatalytic activity. *ACS Appl. Mater. Interfaces* **2010,** *2* (6), 1769-1773.

260.   Khan, Z. R.; Khan, M. S.; Zulfequar, M.; Khan, M. S., Optical and structural properties of ZnO thin films fabricated by sol-gel method. *Materials Sciences and Applications* **2011,** *2* (05), 340.

261.   Izaki, M.; Omi, T., Characterization of transparent zinc oxide films prepared by electrochemical reaction. *J. Electrochem. Soc.* **1997,** *144* (6), 1949-1952.

262.   Castanedo-Perez, R.; Jimenez-Sandoval, O.; Jimenez-Sandoval, S.; Marquez-Marin, J.; Mendoza-Galvan, A.; Torres-Delgado, G.; Maldonado-Alvarez, A., Influence of annealing temperature on the formation and characteristics of sol-gel prepared ZnO films. *J. Vac. Sci. Technol. A-Vac. Surf. Films* **1999,** *17* (4), 1811-1816.

263.   Bandyopadhyay, S.; Paul, G.; Roy, R.; Sen, S.; Sen, S., Study of structural and electrical properties of grain-boundary modified ZnO films prepared by sol–gel technique. *Materials Chemistry and Physics* **2002,** *74* (1), 83-91.

264.   Alias, S.; Ismail, A.; Mohamad, A., Effect of pH on ZnO nanoparticle properties synthesized by sol–gel centrifugation. *Journal of Alloys and Compounds* **2010,** *499* (2), 231-237.

265.   Becheri, A.; Dürr, M.; Nostro, P. L.; Baglioni, P., Synthesis and characterization of zinc oxide nanoparticles: application to textiles as UV-absorbers. *Journal of Nanoparticle Research* **2008,** *10* (4), 679-689.

Appendix

Tafel plots obtained from ZnO films
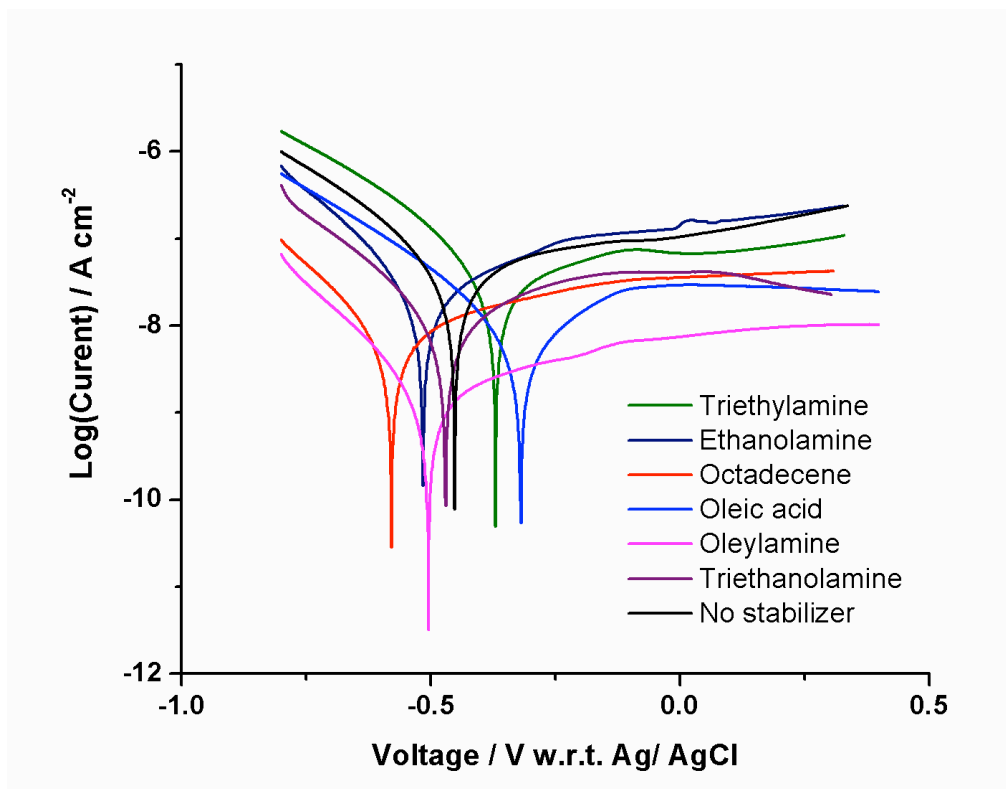
Fig. S1. Tafel plots for zinc oxide films grown with various stabilizers and also without stabilizer

Tafel plots for the ZnO films, formed by using various stabilizers, are shown in Fig. S1. Data was obtained by scanning the potential between −0.8 V (w.r.t. Ag/AgCl) to −0.025 V, in a 0.1 M KCl (aqueous) electrolyte, at room temperature. Samples were prepared by wrapping parafilm all around, except for a 0.5 cm × 0.5 cm area that was exposed to the electrolyte. This sealing of the edges by an insulator limited measurement and analysis errors due to points of high electric field concentration. Open circuit potential values were between −0.5 V and −0.3 V, implying that ZnO films exhibit blocking behavior in that potential range.

Charge carrier concentration measurement using EIS
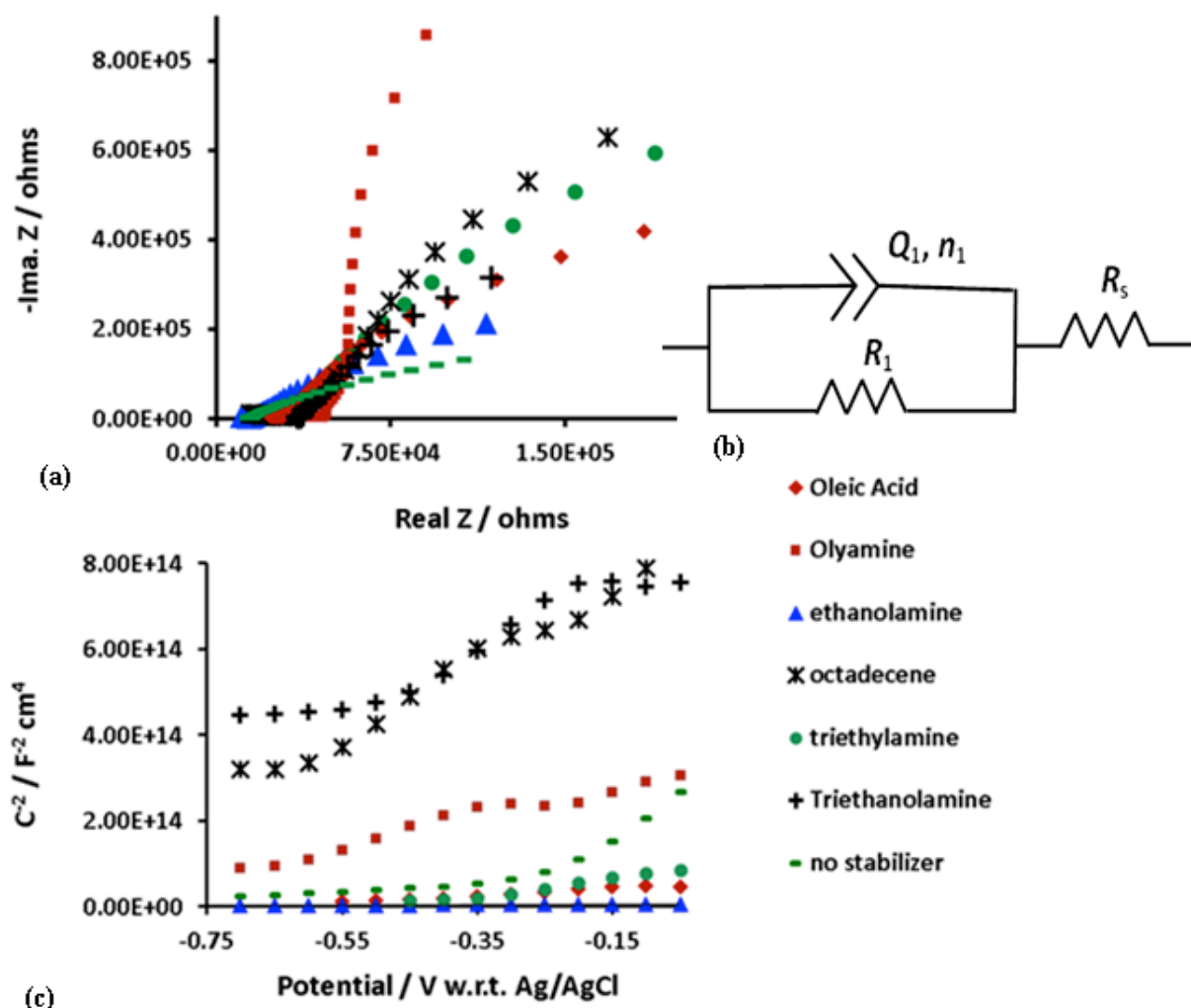
Fig. S2 Nyquist plots (a), equivalent circuit model (b) and Mott Schottky's plot (c) for zinc oxide films grown with various stabilizers and also without stabilizer.
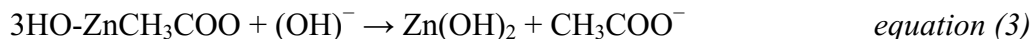
Section S1: Chemistry of the sol formation process

Triethanolamine, ethanolamine and triethylamine cause hydrolysis and generate OH^- ions, as per *equation (1)*:

In *equation (1)*, "R" denotes triethanolamine, ethanolamine, and triethylamine

$$R + H_2O \leftrightarrow [R]^+ + OH^- \qquad\qquad equation\ (1)$$

Zn^{2+} from zinc acetate precursors react with OH^- ions forming $Zn(OH)_2$ ions, as per *equations (2), (3) and (4)*[245,163,246,247]:

Formation of zinc hydroxide:

$$Zn(CH_3COO)_2 + (OH)^- \rightarrow HO\text{-}Zn\text{-}CH_3COO + CH_3COO^- \qquad equation\ (2)$$

$$3HO\text{-}ZnCH_3COO + (OH)^- \rightarrow Zn(OH)_2 + CH_3COO^- \qquad equation\ (3)$$

$$Zn^{2+} + 2OH^- \rightarrow Zn(OH)_2 \qquad equation\ (4)$$

$Zn(OH)_2$ precursors decompose to ZnO under hydrothermal conditions as per *equation (5)*

$$Zn(OH)_2 \rightarrow ZnO + H_2O \qquad equation\ (5)$$
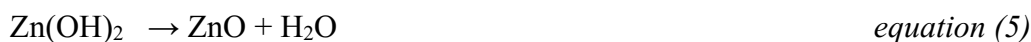
ZnO forms complexes with amine bearing (primary amines) organic stabilizers[248] (e.g. triethanolamine, ethanolamine and triethylamine). For example, as shown in Fig. S3 (a), triethanolamine forms a complex with ZnO
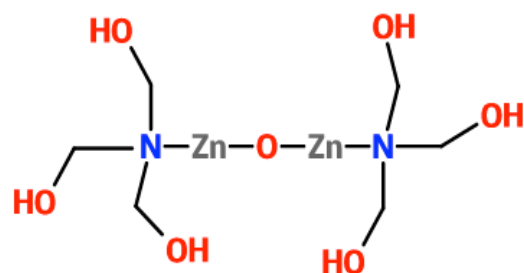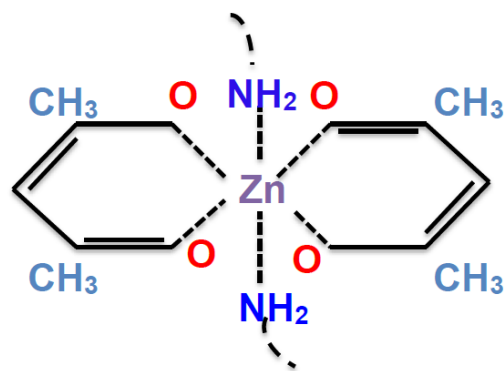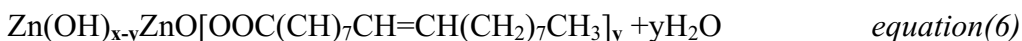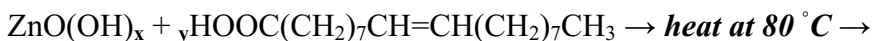

(a)   (b)

Fig. S3 (a) Representative structure of Zinc oxide – triethanolamine complex[249] , and (b) zinc acetate – oleylamine complex[250]

With oleylamine, zinc acetate forms a [Zn(acetate)$_2$]–oleylamine complex (pictorial schematic shown in Fig. 2 (b)) which thermally decomposes to yield ZnO.[250,251] With stabilizers like oleic acid and octadecene, ZnO(OH) species, generated by hydrolysis reaction, react to form complexes. An example reaction for oleic acid in shown in *equation (6),*[251] where, the zinc oxide – oleic acid complex yields ZnO at temperature above 400 °C [252]

$$ZnO(OH)_x + {}_yHOOC(CH_2)_7CH=CH(CH_2)_7CH_3 \rightarrow \textbf{\textit{heat at 80 °C}} \rightarrow$$

$$Zn(OH)_{x\text{-}y}ZnO[OOC(CH)_7CH=CH(CH_2)_7CH_3]_y + yH_2O \qquad equation(6)$$

## Section S2: Effect of sol-stabilizer on crystallographic orientation

Preferred crystalline orientations are attained because of capping of growth of certain crystal planes and promoting the growth of others by stabilizers. Amine bearing small alkyl chain stabilizers, such as ethanolamine, triethanolamine and triethylamine function as complex forming agents that stabilize positively charged Zn^{2+} ions, and promote preferred crystalline orientation of ZnO along the c-axis by aiding polymerization of ZnO chains. This phenomenon is favored by the fast enough rate of hydrolysis, in order to generate ZnO to feed the formation process of orientated network of ZnO chains.[163] These stabilizers also provide a dense matrix for oriented crystal growth.[84] Other authors[253] state that amine bearing stabilizers (such as triethanolamine) aid in oriented agglomeration (by collision, rotation and oriented attachment) of ZnO and their growth.

Also notable is that stabilizers such as oleic acid and oleylamine have long alkyl chains that form complexes which cap surfaces of the Zn^{2+} species restricting growth in certain directions. For instance, the coordinated complex formed by oleylamines are located at the top and at the bottom which have chains of alkyl groups that interact by Van der Waal's forces, promoting formation of oriented two-dimensional ZnO crystals.[254,255,256] In case of octadecene, preferred crystalline orientation is not observed because it is not a coordinating solvent, and therefore no one crystal plane was favored as a growth direction.[257]

Table S1. Ranking order of films based on value of material parameters and correlation to actual surface area

Ranking based on ratio of actual to geometric surface area	Photo to dark current ratio	Lifetime (s)	Bulk mobility (cm^2 V^{-1} s^{-1})	Doping (cm^{-3})
Ethanolamine (13.8)	Ethanolamine (90)	No stabilizer (42.3)	No stabilizer (23)	Ethanolamine (4.7E18)
Triethanolamine (8.4)	No stabilizer (62.9)	Ethanolamine (38.03)	Octadecene (11)	No stabilizer (9.4E16)
No stabilizer (6.5)	Triethanolamine (40)	Triethanolamine (34)	Triethanolamine(10)	Triethanolamine (7E16)
Triethylamine (4.67)	Triethylamine (4.8)	Triethylamine (32.34)	Triethylamine (2)	Triethylamine (7E16)
Octadecene (2)	Octadecene (4.3)	Octadecene (25)	Ethanolamine (7.8E-3)	Octadecene (3.5E16)

Section S3: FTIR analysis

FTIR spectra for the ZnO films is shown in Fig. 3. There we found that residual organic complexes are present on the resultant ZnO films. The peak intensities are similar for all the ZnO films and therefore we conclude that these organic residues contribute equally to the resistivity of the films. Peak at 482 cm^{-1} corresponds to ZnO.[163,258,259,260,261] Intense peak at 670 cm^{-1} corresponds to CH_2,[249] and those at 1010, 1100 and 1140 cm^{-1} may be ascribed to C–N bonds.[262],[171],[263],[146],[264] Peak at 1365 and 1490 correspond to C-O [163] and those at 1580, 1610 and 1700 correspond to C=O.[163,264] Peak at 2380 cm^{-1} is due to absorption of atmospheric CO_2.[264],[265]
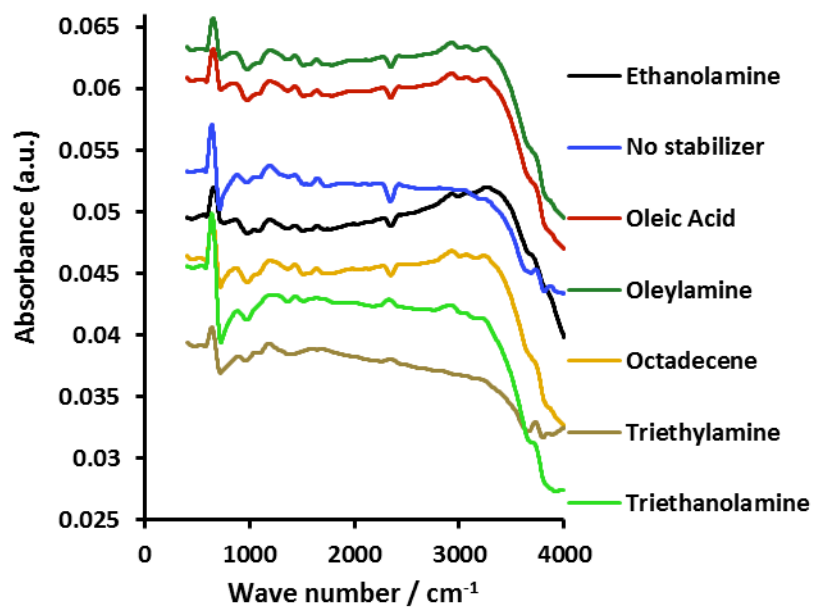
Fig. S4. Plots of FTIR data of ZnO films formed with various stabilizers.

Table S2. Assignment of chemical groups the FTIR peaks exhibited by the ZnO films

Peaks Position (cm^{-1})	Assignment	Reference(s)
482	ZnO	2, 16-19
670	C-H$_2$	2
1010	C-N	20-24
1100	C-N	20–24
1365	C-O	23
1490	C-O	23
1580	C=O	19, 23
1610	C=O	23
1700	C=O	2, 24
2300	O=C=O	23, 25
2950	C-H	2
3600	O-H	2, 23